O.V. Lounasmaa Laboratory

Dissipation at the Nanoscale: Cooper-pair Pumping and Electron Thermometry

Simone Gasparinetti

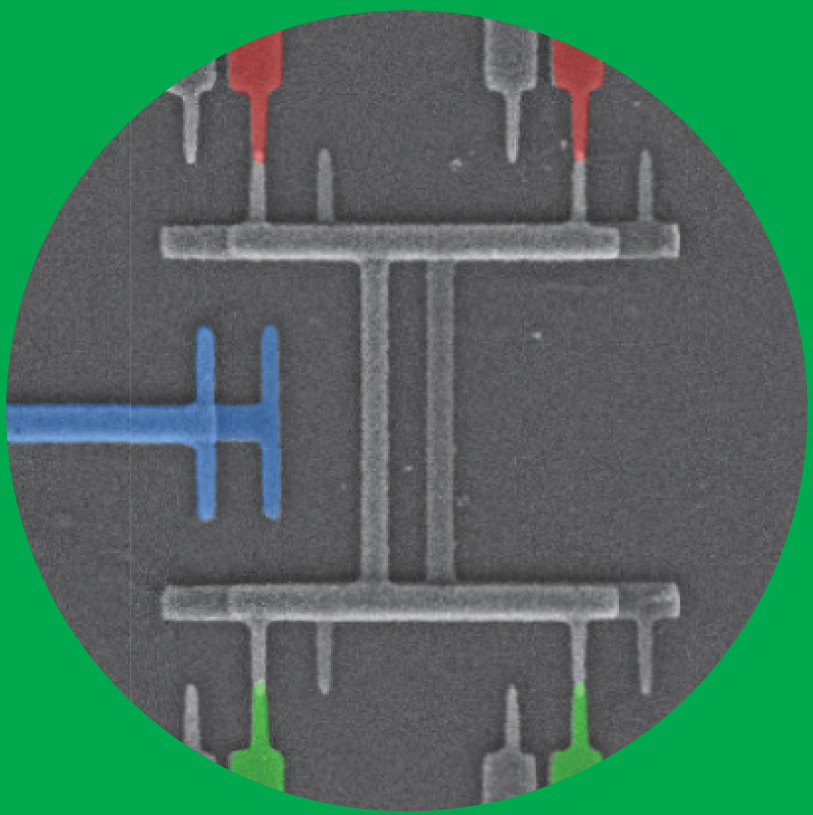

Aalto University

DOCTORAL DISSERTATIONS

Aalto University publication series
DOCTORAL DISSERTATIONS 165/2014

Dissipation at the Nanoscale: Cooper-pair Pumping and Electron Thermometry

Simone Gasparinetti

A doctoral dissertation completed for the degree of Doctor of Science (Technology) to be defended, with the permission of the Aalto University School of Science, at a public examination held at the lecture hall of the school on 18 November 2014 at 12.

Aalto University
School of Science
O.V. Lounasmaa Laboratory
PICO group

Supervising professor
Jukka Pekola

Thesis advisor
Jukka Pekola

Preliminary examiners
Sabrina Maniscalco, Heriot-Watt University, Scotland, UK
Gwendal Fève, École normale supérieure de Paris, France

Opponent
David Haviland, KTH Royal Institute of Technology, Sweden

Aalto University publication series
DOCTORAL DISSERTATIONS 165/2014

ISBN 978-952-60-5919-8 (printed)
ISBN 978-952-60-5920-4 (pdf)
ISSN-L 1799-4934
ISSN 1799-4934 (printed)
ISSN 1799-4942 (pdf)
http://urn.fi/URN:ISBN:978-952-60-5920-4

Unigrafia Oy
Helsinki 2014

Finland

Publication orders (printed book):
Simone Gasparinetti
gasimone@phys.ethz.ch

Aalto University

Abstract

Aalto University, P.O. Box 11000, FI-00076 Aalto www.aalto.fi

Author
Simone Gasparinetti

Name of the doctoral dissertation
Dissipation at the Nanoscale: Cooper-pair Pumping and Electron Thermometry

Publisher School of Science

Unit O.V. Lounasmaa Laboratory

Series Aalto University publication series DOCTORAL DISSERTATIONS 165/2014

Field of research Low-temperature electronics

Manuscript submitted 20 August 2014 **Date of the defence** 18 November 2014

Permission to publish granted (date) 7 October 2014 **Language** English

☐ **Monograph** ☒ **Article dissertation (summary + original articles)**

Abstract

Dissipation in electrical circuits is a theme of great relevance for present and future information technology. On the one hand, dissipation makes it increasingly demanding to scale down the tiny integrated circuits that run our computers. On the other hand, it poses a serious challenge to the realization of a "quantum" computer. In this thesis we study dissipation in three types of nanometer-sized electrical circuits cooled down to subkelvin temperatures.

We first consider Cooper-pair pumps, whose output current is related to quantum geometric phases as well as to the amount of dissipation experienced by the device. We present the first observation of single Cooper-pair pumping without quasiparticle poisoning and a quantitative characterization of adiabaticity breakdown in pumping. We also propose to use a Cooper-pair pump to realize Landau-Zener-Stückelberg interferometry with geometric phases and envisage a novel scheme for Cooper-pair pumping.

We then turn to thermometry in two-dimensional electron gases (2DEGs). Thermalizing 2DEGs is problematic at low temperatures, so that dissipation becomes a critical issue. We aim at measuring the 2DEG temperature while minimizing the self-heating of the thermometer. We first demonstrate a variation on the well-known quantum dot thermometry scheme. We then propose and demonstrate a contactless scheme that combines quantum dot thermometry with charge sensing using a quantum point contact.

The third type of circuit we consider is a fast electronic thermometer built out of a normal metal-insulator-superconductor (NIS) tunnel junction. This thermometer may be used to realize a fast microcalorimeter for single-photon detection in the microwave range. We demonstrate its use by measuring thermal relaxation times of a small copper island at the lowest temperature to date, in a regime where the relevant heat-relaxation mechanisms are strongly suppressed.

Finally, this thesis contains three theoretical studies on the dynamics of periodically driven quantum systems in the presence of dissipation. We focus on the effects of the environment on the steady-state dynamics and on the distribution of energy exchanges between the driven system and the environment. These studies may serve as a starting point for further experiments beyond those reported in this thesis.

Keywords superconducting circuits; Josephson junctions; electronic transport in mesoscopic systems; quantum dots; thermometry; quantum physics; open quantum systems

ISBN (printed) 978-952-60-5919-8 **ISBN (pdf)** 978-952-60-5920-4

ISSN-L 1799-4934 **ISSN (printed)** 1799-4934 **ISSN (pdf)** 1799-4942

Location of publisher Helsinki **Location of printing** Helsinki **Year** 2014

Pages 231 **urn** http://urn.fi/URN:ISBN:978-952-60-5920-4

Preface

The work described in this thesis was carried out in the PICO group of the Low Temperature Laboratory (now O.V. Lounasmaa Laboratory, OVLL), Aalto University, from February 2010 to May 2014.

First of all, I would like to express my deepest gratitude to my high school teacher Roberto Bigoni, who strived to teach me what it means to be a man of learning in the higher sense of the word. Whether he managed, I cannot tell – but for sure I loved his lessons and he did get me into studying physics at university, so here we are.

I would like to thank professor Jukka Pekola for accepting me as a Ph.D. student in his group, for being so present in the daily life of the lab and for constantly pushing his students. I tried to learn as much as I could from him, but even after several years working closely together, the task is far from completed. I would also like to thank professor Matti Kaivola, who initially acted as my Ph.D. advisor and indeed provided me with some invaluable advice how to survive the academic world. [1]

Many thanks to Matthias Meschke, whose outstanding technical knowledge is behind all experiments performed in our group. Thanks to Mikko Möttönen, who kick-started me into Cooper-pair pumping, and to Youngsoo Yoon, with whom I performed my first experiments. Thanks to Ville Maisi, especially for teaching me how to take good care of a plastic dilution refrigerator. Many thanks to Paolo Solinas, who has become a close colleague and a close friend. Thanks to Klaara Viisanen, whose Master thesis I partly instructed and who will hopefully bring our thermometry experiments to the next level... keep it up, Klaara! I am indebted to many past and present members of PICO group, with whom I shared the daily life of the lab, as well as some nice moments outside of the lab. It is long list, that certainly includes Thomas Aref, Massimo

[1] I will omit academic titles hereafter.

Borrelli, Timothé Faivre, Anna Ferring, Anna Feshchenko, Dima Golubev, Tommy Holmqvist, Sergey Kafanov, Ivan Khaymovich, Jonne Koski, Sarah MacLeod, Elsa Mannila, Juha Muhonen, “Leila” Najafi, Hung Nguyen, Antti Peltonen, Olli-Pentti Saira, Mathieu Taupin. Let me also mention some “honorary members” of our group: Antti Kemppinen, Nikolai Cherukov, Andrej Timofeev. Many thanks to the “guys downstairs”, with whom I occasionally shared some good coffee and some great talk: Joonas Govenius, Russell Lake, Kuan Yen Tan, Emmi Ruokokoski, Juha Salmilehto, Philip Jones. Thank you to the many people I had inspiring conversations with at OVLL, including Tero Heikkilä, Sorin Paraoanu, Alexander Savin, Mika Sillänpaa. Mika also accepted me as teaching assistant for his course on “Experimental methods in physics”, by which I learned a lot.

One thing I particularly enjoy in science is collaboration. During these years, I had the pleasure of meeting and exchanging ideas with many brilliant people, who in different ways all contributed to this work. In Pisa, at the NEST laboratories, Francesco Giazotto, my M.Sc. thesis advisor, the one who introduced me to professor Pekola’s work, and a source of inspiration during these years; then Fabio Deon, “Pepa” Martínez, the director Lucia Sorba, and the former director Fabio Beltram. At Scuola Normale Superiore, Stefano Pugnetti and “Saro” Fazio. In Grenoble, Patrick Torresani and Silvano de Franceschi. In Ulm, Vera Gramich and Joachim Ankerhold. In Karlsruhe, Ingo Kamleitner, Philip Wollfarth and “Sasha” Shnirman. In Genova, “Ale" Braggio and Maura Sassetti. In San Diego, CA, Sebastiano Peotta. In Oulu, Matti Silveri. In Santa Barbara, CA, Andrew Cleland, who accepted me as a visiting student in his group for three months, Joerg Bochmann, who supervised my work there, and many students in Andrew and John Martinis’ groups. In Lund, *la* Francesca Battista. In Aachen, Christoph Stampfer, Federica Haupt and Janine Splettsloesser. In Jerusalem, Amikam Levy and Ronnie Kosloff. In Göteborg, Marco Arzeo, Astghik Adamyan and Sergey Kubatkin.

I would like to thank cleanroom engineer Paula Heikkilä and the director of Aalto Nanofab, Veli-Matti Airaksinen, for their excellent management work at the Micronova Nanofabrication Centre. Thanks to the many students and researchers in Micronova that kept stuff in good shape, shared good advice on how to develop a certain process, and generally contributed to a pleasant as well as productive work environment. I would also like to thank the past and present administration staff at OVLL and Aalto for taking care of so many things.

An acknowledgement is due to those institutions which provided financial support for this work: the European Union (mainly through the FP7 project “GEOMDISS”), the Finnish National Graduate School in Nanoscience (NGS-NANO) and the Doctoral Network in Condensed Matter and Materials Physics (CMMP) of Aalto University.

On the personal side, I would like to thank my partner, my family and my closest friends for every bit of love, fun, and support during these interesting years.

Zürich, October 29, 2014,

Simone Gasparinetti

Contents

List of Publications

This thesis consists of an overview and of the following publications which are referred to in the text by their Roman numerals.

I S. Gasparinetti, F. Deon, G. Biasiol, L. Sorba, F. Beltram, and F. Giazotto. Probing the local temperature of a two-dimensional electron gas microdomain with a quantum dot: Measurement of electron-phonon interaction. *Physical Review B*, **83**, 201306, 2011.

II Y. Yoon, S. Gasparinetti, M. Möttönen, and J. P. Pekola. Capacitively Enhanced Thermal Escape in Underdamped Josephson Junctions. *Journal of Low Temperature Physics*, **163**, 164, 2011.

III S. Gasparinetti, P. Solinas, and J.P. Pekola. Geometric Landau-Zener Interferometry. *Physical Review Letters*, **107**, 207002, 2011.

IV S. Gasparinetti, P. Solinas, Y. Yoon, and J. P. Pekola. Single Cooper-pair pumping in the adiabatic limit and beyond. *Physical Review B*, **86**, 060502(R), 2012.

V S. Gasparinetti and I. Kamleitner. Coherent Cooper-pair pumping by magnetic flux control. *Physical Review B*, **86**, 224510, 2012.

VI S. Gasparinetti, M. J. Martínez-Pérez, S. de Franceschi, J. P. Pekola, and F. Giazotto. Nongalvanic thermometry for ultracold two-dimensional electron domains. *Applied Physics Letters*, **86**, 224510, 2012.

VII S. Gasparinetti, P. Solinas, S. Pugnetti, R. Fazio, and J. P. Pekola. Environment-Governed Dynamics in Driven Quantum Systems. *Physical Review Letters*, **110**, 150403, 2013.

VIII P. Torresani, M. J. Martínez-Pérez, S. Gasparinetti, J. Renard, G. Biasiol, L. Sorba, F. Giazotto, and S. De Franceschi. Nongalvanic

primary thermometry of a two-dimensional electron gas. *Physical Review B*, **88**, 245304, 2013.

IX V. Gramich, S. Gasparinetti, P. Solinas, J. Ankerhold. Lamb shift enhancement and detection in strongly driven superconducting circuits. *Physical Review Letters*, **113**, 027001, 2014.

X S. Gasparinetti, P. Solinas, A. Braggio, M. Sassetti. Heat-exchange statistics in driven open quantum systems. Accepted for publication in *New Journal of Physics*, arXiv:1404.3507, 2014.

XI S. Gasparinetti, K. L. Viisanen, O.-P. Saira, T. Faivre, M. Arzeo, M. Meschke, and J. P. Pekola. Fast electron thermometry towards ultrasensitive calorimetric detection. arXiv:1405.7568, 2014.

Author's Contribution

Publication I: "Probing the local temperature of a two-dimensional electron gas microdomain with a quantum dot: Measurement of electron-phonon interaction"

The Author fabricated the sample, performed the measurements, analyzed the data and wrote the manuscript.

Publication II: "Capacitively Enhanced Thermal Escape in Underdamped Josephson Junctions"

The author contributed developing the measurement technique and performed some preliminary measurements.

Publication III: "Geometric Landau-Zener Interferometry"

The Author developed the theory, carried out the numerical analysis and wrote the manuscript.

Publication IV: "Single Cooper-pair pumping in the adiabatic limit and beyond"

The Author fabricated the sample, performed the measurements, analyzed the data and wrote the manuscript.

Publication V: "Coherent Cooper-pair pumping by magnetic flux control"

The Author conceived the idea, carried out most part of the analysis and wrote the final version of the manuscript.

Publication VI: "Nongalvanic thermometry for ultracold two-dimensional electron domains"

The Author carried out the analysis and wrote the manuscript.

Publication VII: "Environment-Governed Dynamics in Driven Quantum Systems"

The Author developed the theory, carried out the numerical analysis and wrote the manuscript.

Publication VIII: "Nongalvanic primary thermometry of a two-dimensional electron gas"

The Author contributed to the design of the experiment and to the writing of the manuscript.

Publication IX: "Lamb shift enhancement and detection in strongly driven superconducting circuits"

The Author assisted in the development of the theory, provided some code for numerical simulations and contributed to the writing of the manuscript.

Publication X: "Heat-exchange statistics in driven open quantum systems"

The Author developed the theory and wrote most part of the manuscript.

Publication XI: "Fast electron thermometry towards ultra-sensitive calorimetric detection"

The Author had a significant contribution in fabricating the samples, performing the measurements, analyzing the data and writing the manuscript.

List of Abbreviations

2DEG two-dimensional electron gas.

ALD atomic layer deposition.

AWG arbitrary waveform generator.

CPP Cooper-pair pump.

DAC digital-to-analog converter.

EGD environment-governed dynamics.

FP flux pumping.

FSA full secular approximation.

NIS normal metal – insulator – superconductor.

PSA partial secular approximation.

QD quantum dot.

QPC quantum point contact.

SGD system-governed dynamics.

SQUID superconducting quantum interference device.

1. Introduction

In this thesis we study very small electrical circuits (on the scale of tens of nanometers) cooled down to very low temperatures (from around $1\,\mathrm{K}$ down to $20\,\mathrm{mK}$). The smallness of the circuits allows us to restrict our attention to a few degrees of freedom. As temperature is lowered, these degrees of freedom are less and less perturbed as thermal fluctuations are suppressed. Qualitatively new phenomena emerge under these conditions, many of which can only be understood in the framework of quantum mechanics.

This thesis includes experimental as well as theoretical contributions that can be classified into three main subjects. The subjects are quite diverse, but they fall under a common theme: dissipation. Dissipation in electrical circuits usually refers to the amount of energy that is "wasted" during their operation. Dissipation may come about because of nonidealities in the circuit, as well as due to intrinsic limitations (think of the Landauer principle). We also speak of dissipation when considering the interaction of a quantum mechanical system (in our case, a "quantum circuit") with its environment. The dynamics of an isolated quantum system follows the Schrödinger equation, of which energy eigenstates are stationary solutions. However, when we look at a finite system embedded in its environment, we find that the interaction with the environment induces "quantum jumps" between states with different energy. These jumps correspond to the emission or absorption of energy quanta that are "dissipated" in the environment.

In Chapter 2 we present our results on the first and "core" subject of this thesis, Cooper-pair pumping. Cooper-pair pumps are a particular type of charge pumps, based on superconducting circuits. Charge pumps are devices which actively transfer a precise amount of charge upon application of a time-dependent protocol. They are an active subject of research as

they may provide a new definition for the *Systéme international* (SI) unit of electric current. Among different types of pumps, Cooper-pair pumps stand out for being macroscopically coherent quantum devices, much in the same way as other superconducting quantum circuits (quantum bits, or qubits) used for quantum information and quantum computation purposes. An interesting feature of Cooper-pair pumps is their natural connection with geometric phases in quantum mechanics. Another one is that the measured pumped charge is determined by an interplay between the driving protocol and the interaction with the environment, which brings dissipation into the problem. In Publication II we show how to circumvent a potential issue that arises when using a small Josephson junction as a current threshold detector to monitor the pumped charge. In Publication IV we demostrate controlled pumping of a single Cooper-pair in a device free of quasiparticle poisoning and use the pumped charge in the nonadiabatic regime as a proxy for Landau-Zener transitions in the device. In Publication III we propose Landau-Zener-Stückelberg interferometry based on geometric phases and show how to observe this effect in a Cooper-pair pump. Finally, in Publication V we propose a novel scheme for Cooper-pair pumping, where Cooper pairs are delocalized throughout the pumping process.

In Chapter 3 we present our results on thermometry in two-dimensional electron gases (2DEGs). With their low electronic density and high mobility, 2DEGs provide a unique platform for the study of highly correlated electron phases. Temperature here is a key factor, as the many phenomena of interest are characterized by very small energy scales. On the other hand, thermalizing the 2DEG is problematic at low temperatures, as the electrons get more and more decoupled from the phonons of the host lattice. Dissipation in the 2DEG then becomes a critical issue, as it can lead to significant overheating. Our efforts have been aimed at assessing the 2DEG temperature while minimizing the amount of dissipation introduced by the thermometer itself. In Publication I we demonstrate a variation on the well-known thermometry scheme based on a quantum dot. In Publication VI we propose to combine quantum dot thermometry with charge sensing using a quantum point contact and thereby realize a nongalvanic temperature readout. This scheme is experimentally demonstrated in Publication VIII.

In Chapter 4 we present our preliminary results towards the realization of a fast microcalorimeter for single-photon detection in the microwave

range. These results are reported in Publication XI. Our ultimate goal here is to build an all-electrical set-up to study dissipation in driven open quantum systems, using a superconducting circuit as the quantum system and a nanometer-sized resistive island as the environment. Under realistic experimental conditions, energy exchanges between the two can be detected by measuring small temperature changes in the resistive island, corresponding to absorption and emission of single microwave photons.

In Chapter 5 we present three theoretical studies on the dynamics of periodically driven quantum systems in the presence of dissipation. These studies are presented together as they are based on a common formalism, which combines a quantum-master-equation approach with Floquet theory. The conclusions reached are quite general, but the connection to the experiments reported in Chapters 2 and 4 is very explicit. In Publication VII we investigate a regime in which the steady-state dynamics is highly influenced by the environment and take Cooper-pair pumping as a case in point. In Publication IX we show that the dressed-state energies of a strongly driven system can be significantly renormalized by the environment. We predict that this Lamb-shift-type renormalization should be observable in Cooper-pair boxes as well as in Cooper-pair pumps. Finally, in Publication X we study the distribution of heat exchanges between the driven system and the environment. Our predictions could be directly tested using a calorimetric readout of the type discussed in Chapter 5.

In the concluding Chapter 6 we give a brief summary of the experimental techniques used in this work.

2. Cooper–pair pumping

The outline of this chapter is as follows. In Section 2.1 we give a general overview of Cooper-pair pumping. In Section 2.2 we present a general theoretical framework, valid for every Cooper-pair pump. In Section 2.3 we introduce a specific type of pump, the Cooper-pair sluice, which plays a pivotal role in this thesis. In Sections 2.4, 2.5 and 2.6 we present the results obtained in Publication IV, Publication III, and Publication V, respectively.

2.1 Historical review and outlook

The first realization of a Cooper-pair pump (CPP) dates back to the heyday of single electronics [1] and can be regarded as one of the first pieces of evidence for the existence of Cooper pairs as localized charge carriers. Since then, two main types of CPP have been considered in literature. The first one [1, 2, 3] consists of an array of three Josephson junctions defining two superconducting islands. The second one, known as "Cooper-pair sluice" [4, 5, 6, 7], uses SQUIDs as tunable Josephson junctions connecting a single superconducting island to the leads. It plays a major role in this thesis and will be considered in detail in Section 2.3. A third type of CPP, operating as a quantum-coherent turnstile, was demonstrated in Ref. [8].

In theory, CPPs offer a viable alternative to single-electron pumps towards the realization of a metrology standard for current [9]. Advantages include the dissipationless nature of supercurrent, the vanishing density of states at energies below the superconducting gap, and the quantum coherence of the pumping process (as opposed to stochastic electron tunneling). The main obstacles on the way to a quantized current have been identified as (1) Cooper-pair cotunneling, (2) excitations due to Landau-

Zener transitions, and (3) tunneling of quasiparticles. The “sluice" design introduced in [4] marked a progress with respect to both issues (1), as it suppresses cotunneling without resorting to large arrays, and (2), as it pushes the onset of Landau-Zener transitions up in frequency. As for (3), a step forward was made in Publication IV, where improvements in filtering and shielding made it possible to observe clean $2e$ periodicity in the pumped charge, implying a device free from quasiparticle poisoning. Despite this progress, however, the state-of-the-art accuracy of Cooper-pair pumps (about 1%) is still modest, limited by nonidealities in design and fabrication, such as, dissimilar Josephson junctions in the superconducting quantum interference device (SQUID) loops, as well as by low-frequency noise.

In the very last years, the metrological motivation to study CPPs has been declining, also due to the advance of more promising devices – most notably, pumps based on hybrid tunnel junctions [10] and semiconductor quantum dots [11, 12, 13, 14]; see Ref. [15] for a review – and the focus has shifted towards the investigation of more fundamental properties of CPPs. If the phase across a Josephson junction is perhaps the most celebrated example of a macroscopic degree of freedom that exhibits quantum behavior [16], a CPP can be regarded as a prototypical example of a driven quantum system whose dynamics is coupled to a macroscopic observable – the pumped current. Theoretical and experimental investigations have revolved around two distinct yet intertwined themes: geometric phases and dissipation.

Geometric phases naturally arise as the cyclic parametric steering needed to achieve pumping is equipped with a geometric structure in the space of parameters. In the adiabatic limit, manipulations in parameter space are directly mapped to the evolution of the Bloch vector in pseudospin space. The existence of a quantitative relation directly linking the pumped charge to the Berry phase, first proved in [17], discussed in detail in [6] and experimentally verified in [7], is remarkable. It also provides an alternative route to the Berry phase, different from more conventional interferometric settings. The work of Ref. [7] is indeed one of the very first observations of geometric phases in solid-state devices, published shortly after [18].

Beyond the adiabatic limit, the pumped charge generally decreases due to excitations that manifest themselves as pumping errors. On the other hand, the dynamics of the pump becomes richer. In the Cooper-pair sluice, the adiabatic limit breaks down “locally”, due to Landau-Zener transitions

taking place at avoided energy-level crossings. In a quantum-coherent setting, the sequence of Landau-Zener transitions interspersed by time lapses of adiabatic evolution produces interference patterns known as Landau-Zener-Stückelberg interferometry [19]. In Publication III, we propose to use this type of interferometry to study geometric phases, and discuss its application to the Cooper-pair sluice. While the theory underlying our proposal is very general, its application to a CPP reveals unique features: the geometric phase can be directly controlled by the superconducting phase bias across the pump and the interference patterns can be extracted by measuring the pumped charge (as opposed to, say, quantum-state tomography). An experimental characterization of Landau-Zener transitions in the Cooper-pair sluice is provided in Publication IV. Since our proposal, geometric Landau-Zener-Stückelberg interferometry was observed in two different systems, a superconducting qubit [20] and a single trapped ion [21], but it has not yet been observed in a CPP. In Publication IV, the absence of interferometric patterns was ascribed to strong decoherence. This leads us to the second of the two themes we mentioned, that is, dissipation.

Dissipation is unavoidable in CPPs. This statement is based on the fact that CPPs are operated continuously. As a result, interactions with the environment cannot be neglected, however weak the coupling may be. In CPPs, random fluctuations of the local electrostatic potential (charge noise) provide the main source of dissipation. In addition, the pumped current is typically probed with a very low bandwidth (a few Hz) as compared to the frequency of the pumping cycle (tens to hundreds of MHz in Publication IV), so that the output signal is averaged over a great (about 10^6) number of cycles. Altogether, continuous operation and massive averaging – the latter in the absence of a reset protocol between subsequent realizations – establish a robust link between the pumped charge and the dissipative dynamics of the pump. As shown in both theory and experiments, a measurement of the pumped charge can be used to extract a great deal of information regarding nonadiabatic transitions as well as decoherence. In this respect, the CPP readout is markedly different from that of otherwise similar devices investigated for quantum information and quantum computation purposes, in particular, superconducting quantum bits [22]. A closer analogy can perhaps be drawn between CPPs and quantum heat engines [23].

Theoretical studies of dissipation in CPP started by considering the adi-

abatic limit and the first nonadiabatic corrections [24, 25, 26, 27]. A general result of these works is that ground-state dynamics is not affected by the presence of a cold environment. Moreover, a cold environment can help stabilizing the system against nonadiabatic transitions, hence extending the validity of the adiabatic approximation to higher frequencies. Further theoretical work in the fully nonadiabatic limit has been based on Floquet theory, see Ref. [28] and Chapter 5. At high pumping frequencies, transitions are not localized at avoided crossings, and the relevant energy scale is no longer the instantaneous energy gap, but rather the dressed gap of the driven system (quasienergy gap). In this limit, the most notable result, reported in Publication VII, is that the influence of the environment can be particularly strong close to degeneracies in the dressed gap, giving rise to a qualitatively different dynamics.

Experimental results on dissipation in the nonadiabatic limit were reported in Publication IV and Ref. [8]. The data of Publication IV, measured with a Cooper-pair sluice in a voltage-biased configuration, suggest coherence times no longer than 5 ns. Ref. [8] quotes a $8\,\mu\mathrm{s}$ relaxation time for a similar device, as inferred from coherent oscillations. These figures are similar to those reported in early measurements of quantum coherence in a Cooper-pair box [29, 30]. Longer coherence times, of the order of hundreds of ns, were obtained for a Cooper-pair box in the so-called "quantronium" configuration, when operated close to charge degeneracy ("sweet spot") [31, 32]. It should be mentioned that the best coherence times for superconducting circuits (in the range of a few $\mu\mathrm{s}$ to $1\,\mathrm{ms}$) are nowadays obtained by designs that carefully avoid the single-Cooper-pair regime, thereby keeping the detrimental effects of charge noise at bay [33, 34, 35]. Whether such a strategy could be conveniently applied to a charge pump, is an interesting question that may be addressed in future research. In this view, the proposal of Publication V may provide some useful insight. While still relying on a single-Cooper-pair transistor, it envisages a pumping scheme where Cooper-pairs are delocalized throughout the pumping process and coherently transferred as charge-state superpositions. Such a scheme, which can be realized by modulating magnetic fluxes instead of gates, has some interesting analogies to open quantum pumping in disordered conductors [36, 37, 38, 39, 40].

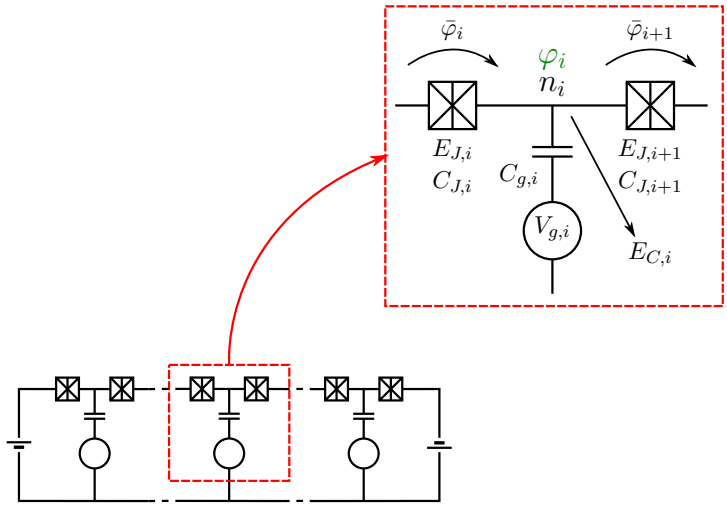

Figure 2.1. Cooper-pair pumps. A generic Cooper-pair pump consists of an array of superconducting islands connected by Josephson junctions. The two ends of the device are connected to superconducting leads held either at fixed chemical potentials (voltage bias), or at fixed phases of the order parameter (phase bias). Inset: Close-up on a single island and notation used in the main text.

2.2 Theoretical framework

A basic theory of Cooper-pair pumping in the adiabatic limit was developed in Refs. [41, 42, 17]. The equivalent circuit of a generic CPP is shown in Fig. 2.1. It consists of an array of N superconducting islands of charging energy $E_{C,i}$ per Cooper-pair, connected in series and to superconducting leads by $N+1$ Josephson junctions of Josephson energy $E_{J,k}$. The gate voltages $V_{g,i}$ control the polarization charges $\vec{q} = \{q_i\}$ on each island. The Josephson energies can be made adjustable by replacing them with flux-controlled dc SQUIDs (see Section 2.3). CPPs are typically operated in the so-called charging regime, so that $E_{C,i} \gg E_{J,k}$ for every i and k. They can be operated either in the presence of a voltage bias V_b or a phase bias φ. We will develop the theory for the case of a phase bias, for which all the coherent properties of CPPs are preserved.

The Hilbert space is generated by either the charge occupation numbers $\vec{n} = \{n_i\}$ of each island, or the phase differences $\{\bar{\varphi}_k\}$ across each junction, the latter constrained by the sum rule $\sum_{k=1}^{N+1} \bar{\varphi}_k = \varphi$. It is also possible to define a phase for each island, as $\varphi_i = \bar{\varphi}_{i+1} - \bar{\varphi}_i$. The corresponding charge and phase operators on each island are conjugate variables and satisfy the usual commutation rule $[\hat{n}_i, \hat{\varphi}_i] = 1$. It is also possible to define the

number of charges that have traversed the k-th junction as $\bar{n}_k = n_k - n_{k-1}$, with n_0 and n_{N+1} now representing the number of Cooper-pairs in the left and right lead, respectively. Charge and phase across each junction are also conjugate variables, so that $[\hat{\bar{n}}_k, \hat{\bar{\varphi}}_k] = 1$. In the following, we will "drop the hat" that we used here to emphasize the distinction between operators and c-numbers.

The total Hamiltonian can be written as

$$H = H_C(\vec{n} - \vec{q}) + \sum_{k=1}^{N+1} \frac{E_{J,k}}{2} \cos \bar{\varphi}_k \ , \tag{2.1}$$

where $H_C(\vec{n}-\vec{q})$ is the energy of the charge configuration $\vec{n}$ in the presence of polarization charges $\vec{q}$, which can be calculated from the capacitance matrix of the circuit.

The current operator for the k-th junction reads $I_k = \frac{2e}{\hbar}[H, \bar{n}_k]$, or, equivalently, $I_k = \frac{2e}{\hbar}\frac{\partial H}{\partial \bar{\varphi}_k}$. It is explicitly given by:

$$I_k = -\frac{e}{\hbar} E_{J,k} \sin \bar{\varphi}_k \ . \tag{2.2}$$

The average current operator across the pump is given by

$$I = \frac{2e}{\hbar}\frac{\partial H}{\partial \varphi} \ . \tag{2.3}$$

If we consider cyclic evolution over a period τ, then charge conservation implies $\int_0^\tau I_k = \int_0^\tau I$, for every k.

Adiabatic limit and Berry phase

The adiabatic theorem of quantum mechanics [43] states that for an infinitely slow (adiabatic) evolution, each eigenstate of the initial Hamiltonian evolves into the eigenstate of the final Hamiltonian, derived from it by continuity. Let $H_0(t)$ be the system Hamiltonian. Let E_n be its (non-degenerate) eigenvalues and $|E_n(t)\rangle$ the corresponding eigenvectors. Let $D(t)$ be the matrix that diagonalizes $H(t)$ at each time with respect to a fixed basis $|n\rangle$. We can write $D(t) = |E_n(t)\rangle\langle n|$. In the rotating frame defined by $|\Psi(t)\rangle \to D(t)|\Psi(t)\rangle$, the effective Hamiltonian reads

$$\tilde{H}(t) = D^\dagger(t) H_0(t) D(t) + w(t) = \tilde{H}_0(t) + w(t) \ , \tag{2.4}$$

where $w(t) = -i\hbar D^\dagger \dot{D}$. From now on, we take $\hbar = 1$. We introduce the adiabatic parameter

$$\alpha = \frac{|w(t)|}{\epsilon_{\min}(t)} \ , \tag{2.5}$$

where $||$ denotes the trace norm and $\epsilon_{\min}$ is the minimum energy gap between two states. The adiabatic limit is attained provided $\alpha \ll 1$. Then

the eigenstates of $\tilde{H}$ are approximate solutions of the Schrödinger equation up to order α. In order to determine the approximate eigenvalues and eigenstates, we use standard first-order perturbation theory. The approximate eigenvalues are given by

$$E'_n = E_n + \langle E_n|\dot{E}_n\rangle \ , \tag{2.6}$$

where we have used the shorthand notation $|\dot{E}_n\rangle = \frac{d}{dt}|E_n\rangle$. The approximate eigenvectors are given by

$$|E'_n\rangle = |E_n\rangle + {\sum_k}' \frac{\langle E_k|\dot{E}_n\rangle}{E_k - E_n}|E_k\rangle \ . \tag{2.7}$$

The total phase accumulated by the n-th eigenstate after time t is given by

$$\Theta_n = \int_0^t E_n(t)dt + \int_0^t \langle E_n|\dot{E}_n\rangle \, dt = \Theta_{d,n} + \Theta_{g,n} \ , \tag{2.8}$$

where we have distinguished a dynamic phase $\Theta_{d,n}$ and a geometric phase $\Theta_{g,n}$. The adiabatic phase is simply the integral of the instantaneous energy of the given state. To understand the meaning of the geometric phases, let us choose a set of parameters $\{\lambda\}$ that determine the time evolution of H_0, so that $H_0(t) = H_0[\vec{\lambda}(t)]$. Then we can write (2.8) as

$$\Theta_{g,n} = \int_{\vec{\lambda}} \langle E_n|\nabla_{\vec{\lambda}} E_n\rangle \, d\vec{\lambda} \ . \tag{2.9}$$

Eq. (2.9) shows that Θ_g is a geometric quantity: it only depends on the path drawn by the vector $\vec{\lambda}$ in parameter space, and not on the speed at which the path is traversed.

Charge currents in the adiabatic limit

Let us now calculate the average current in the adiabatic ground state of the pump. This is given by

$$I_0 = \langle E'_0|I|E'_0\rangle = I_d + I_p \ , \tag{2.10}$$

where

$$I_d = \langle E_0|\tilde{I}|E_0\rangle \ , \tag{2.11}$$

$$I_p = 2\,\Re\mathrm{e}\left[{\sum_k}' \frac{\langle E_0|\tilde{I}|E_k\rangle\,\langle E_k|\dot{E}_0\rangle}{E_k - E_0}\right] \ , \tag{2.12}$$

and we have neglected terms of the order $O(\alpha^2)$. It has become customary in the literature to refer to I_d as dynamic current and to I_p as geometric current or pumped current. The value of I_d only depends on the

instantaneous ground state, telling that a current I_d would flow through the pump even in the absence of any drive. By contrast, a nonvanishing I_p is a direct consequence of the time-dependent drive. By recalling the definition (2.3) and exploiting the identities $\langle E_0|\frac{\partial H}{\partial\varphi}|E_0\rangle = \frac{\partial E_0}{\partial\varphi}$ and $\langle E_0|\frac{\partial H}{\partial\varphi}|E_k\rangle = \langle E_0|\frac{\partial}{\partial\varphi}|E_k\rangle\,(E_k - E_0)$ we can also write:

$$I_d = \frac{\partial E_0}{\partial\varphi}\ , \tag{2.13}$$

$$I_p = -4\,\Im\mathrm{m}\,\langle E_0|\frac{\partial}{\partial\varphi}|\dot{E}_0\rangle\ . \tag{2.14}$$

The total transferred charge after a full cycle of period τ is given by

$$Q_{\rm tot} = \int_0^\tau I_0 dt = Q_d + Q_p\ , \tag{2.15}$$

where a distinction has been made between a dynamic charge Q_d and a pumped charge Q_p.

Relation to the Berry phase

We are now in the position to prove a general relation between the pumped charge and the Berry phase. This relation was derived in [17, 6] and experimentally verified in [7]. To do so, we have to compute the derivative of the Berry phase (2.9) with respect to the overall phase bias φ. This is given by

$$\frac{\partial\Theta_g}{\partial\varphi} = \int_\Lambda d\lambda\left[2\,\Im\mathrm{m}\,\langle E_0|\frac{\partial}{\partial\varphi}|\nabla_\lambda E_0\rangle + \nabla_\lambda\,\langle\frac{\partial E_0}{\partial\varphi}|E_0\rangle\right]\ . \tag{2.16}$$

For a closed path, the second term vanishes and one is left with

$$\frac{\partial\Theta_g}{\partial\varphi} = 2\,\Im\mathrm{m}\int_\Lambda d\lambda\,\langle E_0|\frac{\partial}{\partial\varphi}|\nabla_\lambda E_0\rangle\ . \tag{2.17}$$

By direct comparison one then finds

$$Q_p = -2e\frac{\partial\Theta_g}{\partial\varphi}\ ,\ \text{and} \tag{2.18}$$

$$Q_d = -2e\frac{\partial\Theta_d}{\partial\varphi} \tag{2.19}$$

Equations (2.18) and (2.19) relate the dynamic charge and phase, and the pumped charge and the Berry phase. They were derived assuming the adiabatic limit and a closed path in parameter space. However, suitable generalizations are possible which do not rely on these assumptions. The open-path case can be treated by using the gauge-invariant generalization of the Berry phase proposed in Refs. [44, 45]. Finally, regardless of the speed of the drive, it is meaningful to consider those states which are periodic (up to a phase) in time, that are, the Floquet states. Then the transferred charge is well defined and the Berry phase is naturally replaced by the Aharonov-Anandan phase; see Ref. [28].

Phase bias and current detection in a closed-loop configuration

The most natural setting for exploring coherent effects in Cooper-pair pumping involves a phase bias. The question then arises how such a bias can be realized in practice. The most obvious way is to connect the two leads so as to form a loop of negligible inductance. The phase bias across the pump is then determined by the magnetic flux piercing the loop. The effect of a finite loop inductance is discussed in detail in [46]; using realistic parameters, it is found to be negligible down to the level of 10^{-5} accuracy, which is far beyond the state of the art. In the closed-loop configuration, the current circulating in the loop could be detected by monitoring the current flowing in another, inductively coupled circuit. Another possibility is to shunt the pump with a Josephson junction of large critical current. This still ensure a proper phase bias, as long as phase fluctuations across the shunt junction are small. Furthermore, the current flowing through the pump can be detected by sending current pulses to the device and monitoring its switching to the normal state. In this way, the shunt junction serves the purpose of a current-threshold detector. This technique was demonstrated for the so-called "quantronium circuit" [31], then applied to a CPP [7] and more recently to the detection of phase slips in Josephson-junction arrays [47].

In using Josephson junctions as current threshold detectors, one should notice that the resolution typically scales with the critical current. By using small junctions with critical current of a few tens of nA, current levels as low as $1\,\mathrm{pA}$ can be appreciated [48]. However, such small Josephson junctions are subject to underdamped phase diffusion [49, 50, 51, 52], a regime that is potentially harmful as it introduces dissipation in the quantum circuit. In Publication II, we show experimentally that this regime can be avoided by increasing the junction capacitance. This is done by adding a large ($3\,\mathrm{pF}$) shunt capacitor to the junction. The capacitor is fabricated by atomic layer deposition (ALD). We compare the switching distributions of shunted junctions to those of unshunted junctions of otherwise comparable parameters. As the temperature is increased, the reference junctions enter the phase diffusion regime, as signaled by a decrease in the width of the switching distribution [51, 52]. By contrast, the switching statistics of the shunted junctions agrees with the standard thermal-activation model up to the highest measured temperature. We have also performed measurements of Cooper-pair pumping using a

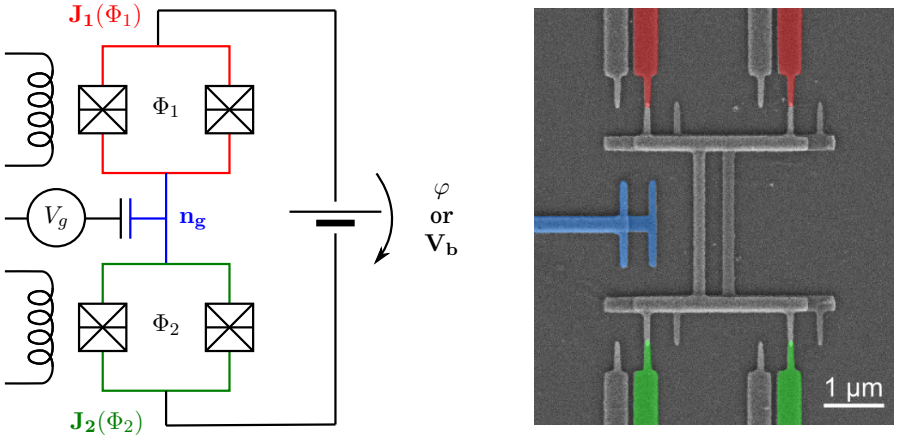

Figure 2.2. The Cooper-pair sluice. Schematic circuit (a) and false-color micrograph of a representative device after Publication IV (b).

Josephson junction as the detector; they are not included in this thesis, but will be reported elsewhere [48].

While the phase bias may be regarded as the definitive setting for studying coherent effects in CPPs, such effects have been observed also in the presence of a voltage bias, both close to the supercurrent branch [Publication IV] and at finite voltages [8].

2.3 The Cooper-pair sluice

In this section we introduce a specific type of Cooper-pair pump, named Cooper-pair sluice, that plays a central role in this thesis.

A schematic drawing of the device is shown in Fig. 2.2(a). It is a fully tunable Cooper-pair transistor, consisting of a small superconducting island connected to leads by two SQUIDs. The SQUIDs, whose loop inductance (geometric + kinetic) is negligible as compared to the Josephson inductance, serve as tunable Josephson junctions of coupling energies J_1, J_2. The coupling energies are set by the magnetic fluxes Φ_l, Φ_r threading the SQUID loops, which can be individually addressed by using suitably designed on-chip coils [53]. A gate electrode capacitively coupled to the island controls its polarization charge in units of Cooper pairs $n_g = C_g V_g/2e$, where C_g is the cross-capacitance between gate and island and V_g the gate voltage. The device is typically operated in the charging regime, meaning that $E_C \gg J_1, J_2$, where $E_C = e^2/(2C_\Sigma)$ is the

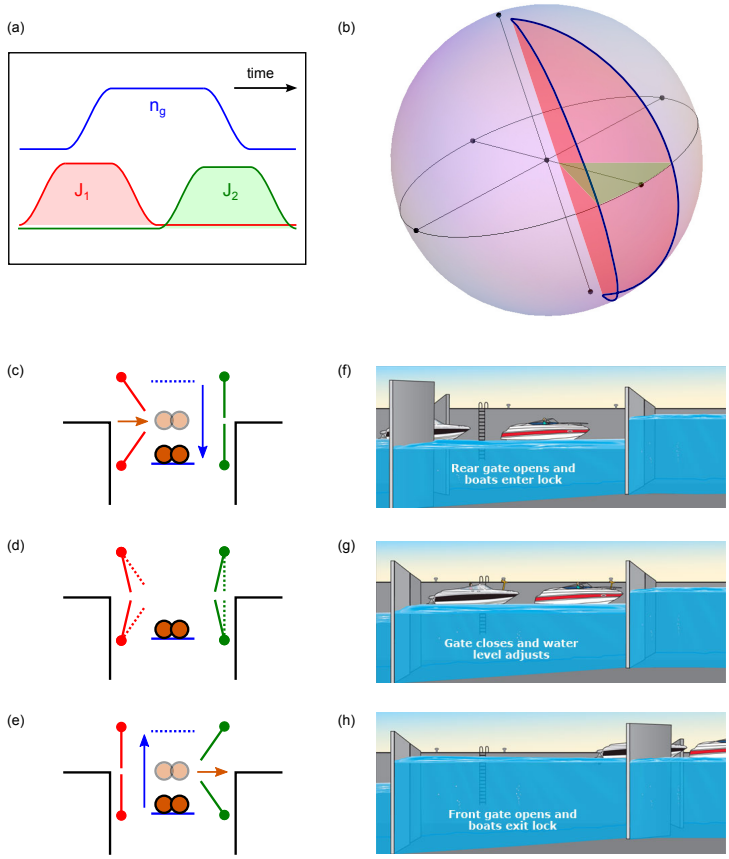

Figure 2.3. How the sluice works. (a) Typical pulse sequence used to achieve pumping. (b) Path drawn by the Bloch vector on the Bloch sphere, as the pulse sequence in (a) is applied. (c-e) Deconstructing the pumping cycle: tunneling in (c), coupling switch (d), tunneling out (e). (f-h) The way a boat lock is operated reminds of the Cooper-pair sluice; after [54].

charging energy of the island and C_Σ its total capacitance. In practice, $C_\Sigma \approx 4C_J + C_g + C_{\rm self} \approx 4C_J$, where C_J is the capacitance of a single junction and $C_{\rm self}$ the self-capacitance of the island. A false-color micrograph of a representative device is shown in Fig. 2.2(b), where we can see the central island, four nominally identical Josephson junctions of area $\approx 70\,\mu\text{m} \times 70\,\mu\text{m}$, the SQUID arms, and the gate.

Pumping is realized by steering the three control parameters J_1, J_2 and n_g in a periodic fashion, as shown in Fig. 2.3(a). The gate is used as a piston to change the number of Cooper-pairs on the island, while the SQUIDs are operated as valves so as to impart a direction to the flow of charge. Snapshots of the pumping cycle are schematically depicted in Fig. 2.3(c-e), showing a Cooper pair tunneling into the island from the left lead (c),

the left SQUID "closing" and the right SQUID "opening" (d), and finally the Cooper pair tunneling out of the island and into the right lead (e). This device, first proposed in Ref. [4], was nicknamed "Cooper-pair sluice" due to the analogy between SQUIDs and sluice gates in water channels. The arrangement of two gates "in series", as in the Cooper-pair sluice, is usually referred to in water transport as a lock. The process of transferring a boat across a lock is illustrated in Fig. 2.3(f-h), indeed showing some analogy with the operation of the Cooper-pair sluice. [1] Anyways, the analogies between Cooper pairs and boats (or marbles, or billiard balls, or even electrons in a Fermi gas) stop here. Cooper-pair tunneling between two superconductors is a quantum coherent process carrying a definite phase. This has important (and observable) implications also in charge-based devices such as the sluice, where it is natural to speak of "single" Cooper pairs as the charge number is a good quantum number to describe the dynamics.

Indeed, the operation of the device can be modeled by restricting the Hilbert space to the states $|0\rangle$ and $|1\rangle$ with no and one excess Cooper pair on the island, respectively. In the $\{|0\rangle, |1\rangle\}$ basis, the sluice Hamiltonian reads

$$H = \begin{pmatrix} E_C(\frac{1}{2} + \delta n_g)^2 & J_+ \cos\frac{\varphi}{2} + iJ_- \sin\frac{\varphi}{2} \\ J_+ \cos\frac{\varphi}{2} - iJ_- \sin\frac{\varphi}{2} & E_C(\frac{1}{2} - \delta n_g)^2 \end{pmatrix} \tag{2.20}$$

where $J_\pm = \frac{1}{2}(J_1 \pm J_2)$, and $\delta n_g = n_g - \frac{1}{2}$ the offset between the gate charge and the degeneracy point. Besides simplifying the treatment, the two-level approximation makes it possible to map the state of the pump into that of a $\frac{1}{2}$ spin immersed in a time-dependent magnetic field ("pseudo-spin formalism"). This mapping can be made explicit by writing (2.20) as $H = \vec{\sigma} \cdot \vec{B}$, where $\{\sigma_i\}$ are the Pauli matrices and the effective magnetic field $\vec{B}$ has components

$$B_x(t) = J_+(t) \cos\frac{\varphi}{2}\,, \tag{2.21}$$

$$B_y(t) = J_-(t) \sin\frac{\varphi}{2}\,, \tag{2.22}$$

$$B_z(t) = E_C\left[1/2 - n_g(t)\right]\,, \tag{2.23}$$

where we put $J_\pm(t) = J_L(t) \pm J_R(t)$. In this formalism, a pumping cycle is described by a closed path drawn by $\vec{B}$ in three-dimensional space. In

[1] For this reason, it seems that the name "Cooper-pair lock" would have been more appropriate. However, in the Netherlands the word *sluis* (or *schutsluis*) is also used for "lock" and that is the place where the first such device was reported to be built, in the fourteenth century.

the adiabatic limit considered in Section 2.2, the spin continuously follows the field, drawing a closed path on the Bloch sphere. An example of such a path is shown in Fig. 2.3(b) for the pumping cycle of Fig. 2.3(a). Some intuitive understanding can be gained from this picture, as the solid angle spanned by the path equals the Berry phase, which, in turn, is related to the pumped charge by (2.18). Furthermore, the projection of the path on the $\hat{xy}$ plane defines an angle that equals the phase bias φ, a unique feature of the Cooper-pair sluice.

2.4 Single Cooper-pair pumping in the adiabatic limit and beyond

The theoretical understanding gained in the previous sections is based on an effective-Hamiltonian description, where the dynamics of the pump is generated by a single, macroscopically-coherent degree of freedom, the number of Cooper-pairs residing on a superconducting island. In the two-level approximation, this dynamics is further reduced to that of a single Cooper-pair hopping on and off the island. This simplified picture is at the heart of many interesting studies on Cooper-pair pumping. In Publication IV, we demonstrate that such a picture can indeed hold in an experimentally accessible regime.

Evidence of Cooper-pair pumping was reported already in [1, 5]. Furthermore, the measurement of the Berry phase reported in [7] can be regarded as indirect proof of the overall quantum coherence of the pumping process. However, a satisfactory characterization of Cooper-pair pumping in the single-Cooper-pair regime was still lacking. In particular, the height of the current steps observed in Ref. [5] when plotting the pumped current against the amplitude of the gate modulation is ef, and not $2ef$, as one would expect if the charge were carried by Cooper pairs. The steps are also spaced by intervals e, and not $2e$, in the gate charge, and no dependence on the gate offset was reported. As for Ref. [7], where a CPP was measured in a phase-biased configuration for the first time, the measurements were performed at large gate amplitudes, corresponding to tens of Cooper pairs traversing the island in a single cycle. Finally, the breakdown of the adiabatic limit had also been investigated, but not quantitatively understood: a decrease in the pumped charge upon increasing the pumping frequency was observed in Ref. [1, 5, 7], but no comparison to any theoretical model was drawn.

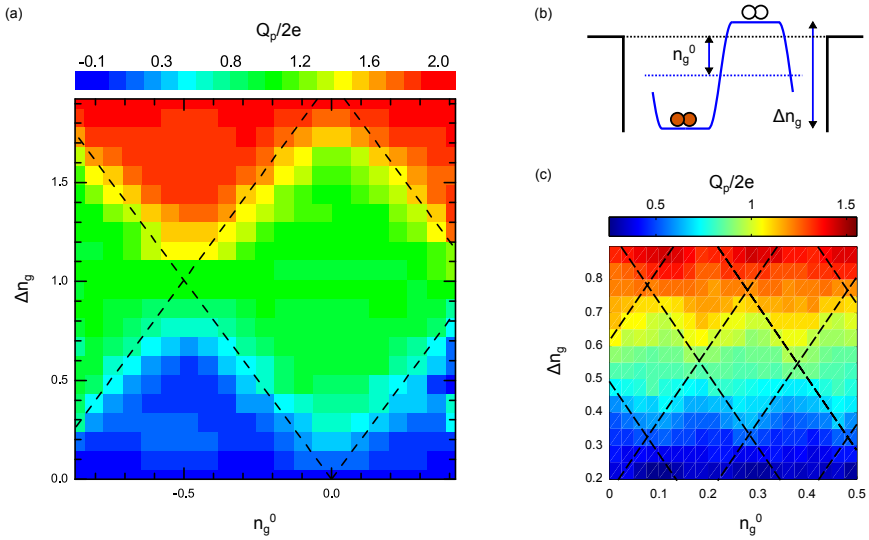

Figure 2.4. Single Cooper-pair pumping. (a) Pumped charge Q_p versus peak-to-peak amplitude δn_g and offset n_g^0 of the gate drive, normalized in units of Cooper pairs. The pumping frequency is $f = 80\,\mathrm{MHz}$. Dashed lines highlight the "pumping diamonds" discussed in the text. (b) Energy-level diagram illustrating the effect of δn_g and n_g^0. (c) Same as (a), for a quasiparticle-poisoned device.

Getting the quasiparticle poison out

One of the greatest threats to single-Cooper-pair devices is posed by quasiparticles. At temperatures much below the superconducting gap, the thermal population of quasiparticles is negligible. However, a nonequilibrium population of quasiparticles is routinely observed in many experiments [55]. While generally harmful for most superconducting quantum devices, including those based on flux [56], nonequilibrium quasiparticles are particularly unforgiving to charge-based devices [57]. Quasiparticle "poisoning" manifests itself in uncontrolled jumps of e in the gate charge, due to incoherent tunneling of quasiparticles on and off the island [58, 59]. The data of Ref. [5] can indeed be explained by considering a quasiparticle tunneling rate intermediate between the pumping frequency (a few MHz) and the acquisition rate (a few Hz). The origin of nonequilibrium quasiparticles is not fully understood, but significant evidence has been gathered, also in our group, that a careful filtering of microwave radiation is crucial in order to keep this population low. [60, 61].

Figure 2.4(a), taken after Publication IV, demonstrates single Cooper-pair pumping in a device free from quasiparticle poisoning. The mea-

sured device is a Cooper-pair sluice as in Fig. 2.2, mounted on the sample stage of a dilution refrigerator cooled down to 20 mK. Two nested rf-tight shields enclose the sample stage in order to screen blackbody radiation from higher-temperature stages. The device is voltage-biased in the supercurrent branch at $V_b = 0$ and the current is read out at room temperature with a transconductance amplifier. Pumping is achieved by applying engineered microwave pulses to the gate and flux lines. In Fig. 2.4(a), the pumped charge is plotted versus the offset n_g^0 and the peak-to-peak amplitude Δn_g of the gate drive, normalized in units of Cooper pairs on the island. Here the pumping frequency is $f = 80\,\mathrm{MHz}$ and the pulse parameters are chosen so as to ensure adiabatic operation. The regions of constant Q_p are diamond-shaped in the offset-amplitude plane. This behavior can remind of the stability diagram a single-electron transistor, with δn_g in lieu of the voltage bias; however, we recall that in the present case no such pattern can be observed without actively driving the device. The position and extent of the diamonds can be predicted from the energy-level diagram of Fig. 2.4(b), where the modulation of the SQUIDs is not shown and it is intended that Cooper-pair tunneling is possible only at resonance, when the respective Fermi levels cross. Inside a given diamond, Q_p is constant and an integer multiple of $2e$ within 2% accuracy. Furthermore, Q_p is $2e$-periodic in the gate charge, that is, the diagonals of the diamonds measure 1 and 2 along the n_g^0 and the Δn_g axis, respectively. For comparison, a similar measurement is shown in Fig. 2.4(c). It was taken during the same cooldown, before a ground loop was diagnosed and eliminated. This indicates blackbody radiation is not the only source of quasiparticle poisoning: bad circuit design works well, too!

Nonadiabatic I – dynamic generation of quasiparticles

While the data of Fig. 2.4(a) are not affected by nonequilibrium quasiparticles, the latter may come into play as a result of nonadiabatic pumping. One way of making the pumping nonadiabatic is to increase the amplitude of the gate modulation. This increases both the effective speed of the drive (continuously), and the number of tunneling events involved (discretely). In Fig. 2.5(a), we plot Q_p versus n_g^0 while increasing δn_g from 0.1 to 7. The data show a clear crossover between pure Cooper-pair and mixed Cooper-pair-quasiparticle dynamics. Up to about $\delta n_g = 3$, Q_p is $2e$-periodic in n_g^0, as in Fig. 2.4(a). The pumping plateaus are also $2e$-periodic in δn_g. The crossover takes place between about $\delta n_g = 3$ and $\delta n_g = 5$, where the

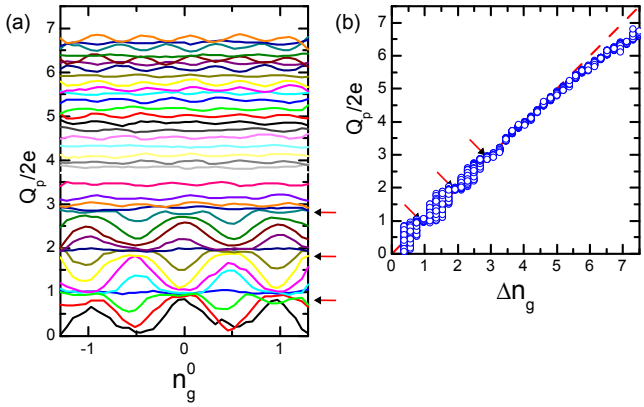

Figure 2.5. Crossover between pure Cooper-pair and mixed Cooper-pair-quasiparticle dynamics. (a) Pumped charge Q_p versus gate offset n_g^0 for increasing gate amplitudes δn_g (bottom to top). (b) Same data as in (a), collapsed over n_g^0 and plotted against δn_g (dots). The dashed line is the adiabatic-limit expectation. The first three pumping plateaus are indicated by arrows.

pattern is blurred. Finally, for $\delta n_g \gtrsim 5$ a clear periodicity is restored, but the period has doubled. These data show that quasiparticle poisoning, while initially absent, can be induced by nonequilibrium quasiparticles generated by a nonadiabatic drive. The link between loss of adiabaticity and quasiparticle poisoning is strengthened by the fact that the crossover is accompanied by a reduction in Q_p with respect to the adiabatic-limit prediction, as shown in Fig. 2.5(b).

We understand the generation of nonequilibrium quasiparticles as a multi-step process, consisting of Landau-Zener tunneling to an excited state, breaking of a Cooper pair, and quasiparticle tunneling. For instance, let us consider the energy-level diagram in Fig. 2.6, where the energy of the ground state and the first three excited states are plotted versus time as the gate is swept across three degeneracy points. Far from the degeneracy points, the Cooper-pair number is well defined for each energy eigenstate. If we start from the ground state on the far left and the drive is adiabatic, then we end up in the ground state on the far right, having loaded three Cooper pairs on the island. By contrast, if we make a Landau-Zener transition at the first crossing, then we end up in the third excited state, having loaded no Cooper pair. At this point, incoherent tunneling of a single quasiparticle is energetically favored, as it would lower the energy by an amount $\Delta E^+ = 11\,\mathrm{E_C}$. The energy of the state with one quasiparticle added to the island is plotted as a dashed line. Now, even if the quasiparticle population in the leads

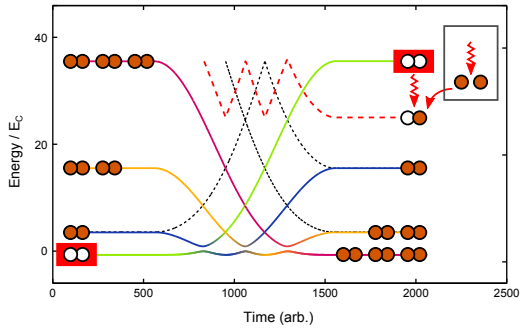

Figure 2.6. A pathway to dynamic quasiparticle generation. The system starts in the ground state (left) and is driven into the second excited state (right) by a Landau-Zener transition. Inelastic relaxation can take place via incoherent tunneling of two quasiparticles, provided the energy gain for the first tunneling ($7E_C$ in this case) exceeds the energy cost 2Δ to break a Cooper-pair.

is depleted, quasiparticle tunneling into the island is still possible provided $\Delta E^+ > 2\Delta$, as in this case an extra quasiparticle (actually, two) can be made available by breaking a Cooper pair. After the tunneling of such a quasiparticle, the island is left in a metastable state with an odd quasiparticle number, which may then further decay by tunneling of a second quasiparticle. Overall, this mechanism is similar to the well-known Josephson-quasiparticle cycle [62], with the gate drive playing the role of an effective voltage bias in dynamically creating nonequilibrium. In the general case, the energy gain for adding/removing a single quasiparticle is $\Delta E^{\pm}[n, n_g] = 4E_C[(n - n_g)^2 - (n - n_g \mp 1/2)^2]$, where n is the number of excess Cooper pairs on the island. For the device measured in Publication IV, $E_C = 0.33\Delta$, so that dynamic quasiparticle generation is only possible from the second excited state and upwards, provided the drive is fast enough to induce Landau-Zener transitions. This is in semiquantitative agreement with the results of Fig. 2.5.

Nonadiabatic II – Probing Landau-Zener transitions

The absence of quasiparticle poisoning in our device, together with the fact that energy relaxation via generation of quasiparticles is an active channel only at highly excited states, makes it possible to study nonadiabatic transitions in a quasiparticle-free scenario. In order to do so, we work at small amplitudes of the gate pulse, so that the dynamics of the

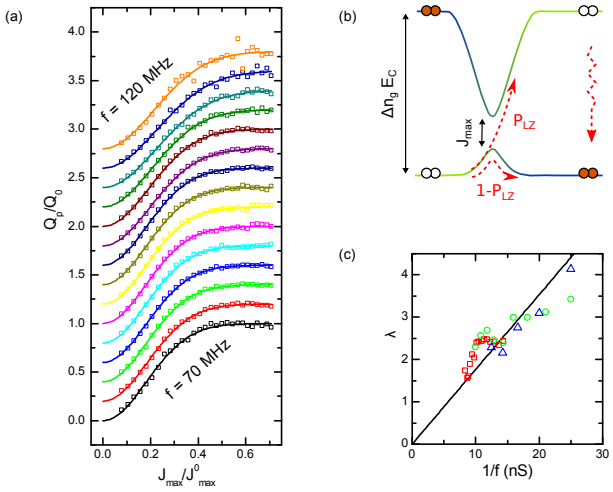

Figure 2.7. Nonadiabatic pumping and Landau-Zener transitions. (a) Normalized pumped charge Q_p/Q_0 versus Josephson coupling $J_{\max}$, for a set of frequencies in the range of 70 and 120 MHz (squares). The traces are vertically stacked for clarity. The full lines are best-fits of (2.24) in the main text. (b) Sketch of the model considered in the text, where Landau-Zener transitions are always followed by inelastic relaxation. (c) Frequency dependence of the fit parameter λ, as extracted from three different measurement sets (squares, circles, and triangles). The full line is a linear fit to the data.

pump is effectively reduced to that of a two-level system. We henceforth denote with E_C the charging energy of a Cooper-pair, so that $E_C = 2e^2/C_\Sigma$ instead of $e^2/(2C_\Sigma)$. Transitions from the ground into the excited state can occur due to Landau-Zener tunneling. For a single avoided energy crossing, the transition probability $P_{LZ} = e^{-2\pi\delta}$ is governed by the adiabatic parameter $\delta = J_{\max}^2/\hbar v$, where $J_{\max}$ is the Josephson coupling of the active SQUID at the crossing and $v = E_C dn_g/dt$ the rate of change of the energy difference between the two charge states. The adiabatic parameter, and hence the transition probability, can be acted upon in several independent ways. For instance, we can change $J_{\max}$ by tuning the amplitude of the flux pulses, or dn_g/dt by changing either the rise time of the gate pulse, or the pumping frequency. In Fig. 2.7(a), we plot Q_p versus $J_{\max}$, normalized to its maximum value $J_{\max,0}$, when $n_g^0 = 0$ and $\delta n_g = 0.45$. The traces are taken at different pumping frequencies in the range of 70 and $120\,\mathrm{MHz}$; they have been normalized and vertically offset for clarity. In order to interpret the results quantitatively, we resort to the model illustrated in Fig. 2.7(b). The model relies on two rather crude assumptions, namely, that

(i) each nonadiabatic transition is followed by energy relaxation before the system reaches the next avoided crossing, and

(ii) on average, the relaxation process entails no net transfer of charge across the island.

Under (i) and (ii), it is easy to show that the expected pumped charge at dynamic steady state is given by the expression

$$Q_p/2e = 1 - P_{LZ} \ , \tag{2.24}$$

providing a transparent link between Landau-Zener transitions and pumped charge. Armed with this understanding, we fit to each trace the expression $Q_p(x) = Q_0\left[1 - \exp\left(-2\pi\lambda x^2\right)\right]$, where $x = J_{\max}/J_{\max,0}$ and λ is a fit parameter, to be compared with the model prediction $\lambda \propto J_{\max,0}^2/E_C\Delta n_g hf$. The data and our single-parameter fit are in excellent agreement over the full frequency range. The dependence of the fitting parameter λ on the inverse pumping frequency also follows the linear prediction of the model, as shown in Fig. 2.7.

Altogether, these results provide evidence that the departure from the adiabatic limit takes place via Landau-Zener transitions and that our understanding of decoherence effects, albeit simplified, is essentially cor-

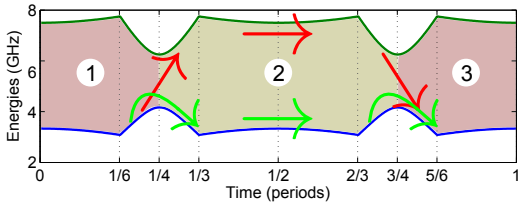

Figure 2.8. Landau-Zener-Stückelberg interferometry. Time evolution of the instantaneous (adiabatic) ground and excited-state energies. The pumping cycle is as in Fig. 2.3(a). Landau-Zener transitions can occur at times $t_1 = T/4$ and $t_2 = 3T/4$. The green and red arrows outline two possibly interfering transition paths.

rect. The validity of assumption (i) in the frequency range of the experiment sets an upper bound of about 5 ns on the relaxation time of the island, which is consistent with measurements of Rabi oscillations in charge qubits [29]. Furthermore, our results indicate that the pumped charge is indeed a sensitive probe of the dynamics of the pump. In the following section, we will show how this property could be exploited to realize an interferometer for geometric phases.

2.5 Geometric Landau-Zener-Stückelberg interferometry

The experimental observations of the previous section are accounted for by a model where decoherence effects are strong. In this model, subsequent Landau-Zener transitions are totally uncorrelated (in both classical and quantum sense). A different scenario would arise if the coherence time of the pump were greater than the time interval between to subsequent crossing, that equals half the pumping period. This could be achieved by operating the pump at a higher frequency (or by improving the coherence times). In a quantum-coherent scenario, Landau-Zener transition paths can interfere according to the different phase accumulated by the ground and excited-state wavefunctions between subsequent crossings. This effect is usually referred to as Landau-Zener-Stückelberg interferometry; it was first observed in atomic and optical systems and recently measured also in superconducting qubits – for a review, see [19]. In all these realizations, the system was driven in such a way that the interference effects have a purely dynamical nature. In general, though,

a quantum state subject to steered evolution acquires both a dynamic and a geometric phase. We already know from Sections 2.2 and 2.3 that this occurs, for example, in the Cooper-pair sluice.

In Publication III, we study Landau-Zener-Stückelberg interference in the sluice as a possible realization of Landau-Zener-Stückelberg interferometry based on geometric phases. Our proposal is general and can be realized in a variety of quantum architectures; still, its application to the sluice reveals some unique features. In particular, the accumulated geometric phase is directly linked to the superconducting phase bias and the interference patterns can be read out at steady-state by measuring the pumped charge. On the other hand, the short coherence times of the sluice are a major drawback. As a matter of fact, soon after our proposal geometric Landau-Zener-Stückelberg interferometry was observed in two different systems, a single trapped ion [21] and a superconducting phase qubit [20], while it still awaits to be observed in a Cooper-pair pump.

Dynamics in the adiabatic-impulse model

Figure 2.8 displays the time-dependent energies of the adiabatic ground and excited state $|g\rangle, |e\rangle$ during a pumping cycle. The avoided level crossings at $t = \tau/4, 3\tau/4$ (τ is the pumping period) correspond to the gate charge passing the degeneracy point. In the limits $E_C \gg J_{max}$ and $hf \lesssim E_C\bar{n}_g$, nonadiabatic transitions are strongly localized at level crossings. In the so-called adiabatic-impulse model [63, 19], Landau-Zener tunneling at an anticrossing is treated as instantaneous. In the adiabatic basis $\{|g\rangle, |e\rangle\}$, it is described by a transfer matrix of the form:

$$N_{LZ} = \begin{pmatrix} \sqrt{1-P_{LZ}}e^{i\tilde{\varphi}_S} & -\sqrt{P_{LZ}} \\ \sqrt{P_{LZ}} & \sqrt{1-P_{LZ}}e^{-i\tilde{\varphi}_S} \end{pmatrix} , \tag{2.25}$$

where $\tilde{\varphi}_S$ is the phase acquired by the adiabatic states in traversing the crossing (Stokes phase) [64]. It is a smooth function of δ taking values between $-\pi/2$ (slow passage) and $-\pi/4$ (fast passage). By contrast, for each adiabatic sector $j = 1, 2, 3$ in Fig. 2.8, the evolution is described by a diagonal matrix of the form

$$U_j = \begin{pmatrix} e^{i\varphi_j} & 0 \\ 0 & e^{-i\varphi_j} \end{pmatrix} , \tag{2.26}$$

where φ_j is half the difference between the phases acquired by the adiabatic states in the given sector. In general, $\varphi_j = \xi_j + \gamma_j$, where we have

distinguished a dynamic (ξ_j) and a geometric (γ_j) contribution. The dynamic phase ξ_j is obtained by integrating the instantaneous energy gap across the sector; as such, it is proportional to the shaded areas in Fig. 2.8. By contrast, the geometric phase γ_j can be calculated as [44, 45]:

$$\gamma_j = \frac{i}{2}\int_{t_{j-1}}^{t_j} dt \left[\left\langle g \left| \frac{d}{dt} \right| g \right\rangle - \left\langle e \left| \frac{d}{dt} \right| e \right\rangle\right] . \tag{2.27}$$

This phase has a purely geometric origin, as it does not depend on the speed at which each adiabatic sector is traversed. Putting things together, the evolution operator U over the full cycle is given by

$$U = U_3 N_{LZ} U_2 N_{LZ} U_1 . \tag{2.28}$$

Eq. (2.28) can be used to gain analytical insight into the dynamics of the pump beyond the adiabatic limit. For example, we can calculate the excitation probability after one cycle, starting from the ground state. This is given by:

$$P = 4P_{LZ}(1-P_{LZ})\cos^2\left(\tilde{\varphi}_S + \xi_2 + \gamma_2\right) . \tag{2.29}$$

For the pumping cycle of the sluice and up to the first order in $[J_{max}/(E_C\bar{n}_g)]^2$, one finds

$$\xi_2 \propto \frac{E_C\bar{n}_g}{hf} , \tag{2.30}$$

$$\gamma_2 = \varphi/2 . \tag{2.31}$$

As expected, the dynamic phase ξ_2 is inversely proportional to the pumping frequency f. By contrast, the geometric contribution is independent of f and directly proportional to the superconducting phase bias ϕ.

Equation 2.29 describes an interference pattern, the excited-state population oscillating between 0 and $4P_{LZ}(1-P_{LZ})$ depending on the argument of the $\cos$ term. In particular, if we neglect the weak dependence of $\tilde{\varphi}_S$ on δ and hence f, the positions of the maxima and minima move in the $\varphi - f$ plane as branches of hyperbolae. By choosing f so that $\tilde{\varphi}_S+\xi_2$ is an integer multiple of π, the dynamic contribution in (2.29) is washed out, resulting in purely geometric Landau-Zener-Stückelberg interferometry. Elimination of the geometric phase can be achieved in a qubit using a spin echo scheme [18, 21, 20].

A complementary and instructive way to understand the interferometric patterns is provided by Floquet analysis [65]. In fact, we can explicitly calculate the quasienergy spectrum by diagonalizing the evolution operator U in (2.28). We find that destructive resonances occur at exact

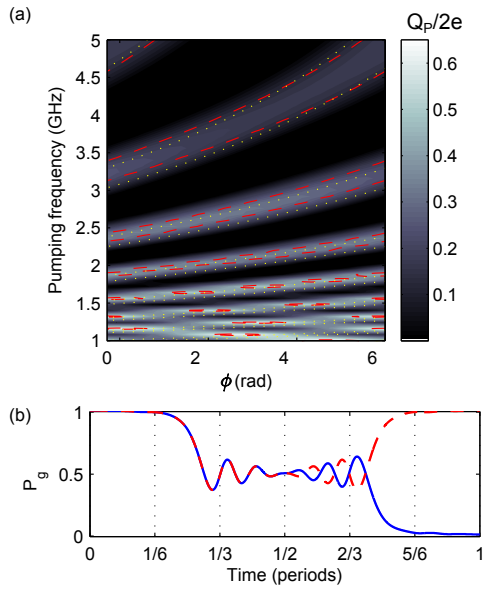

Figure 2.9. Nonadiabatic Cooper-pair pumping. (a) Pumped charge Q_p for a single cycle starting from the ground state, versus phase bias φ and frequency f. Same-ground-state-population lines are plotted for the value 0.9. The numerically exact result (full lines) is in good agreement with the adiabatic-impulse approximation in the fast-passage limit (dotted lines). (b) Ground-state population versus time for a case of destructive (dashed line) and constructive (solid line) interference.

quasienergy crossings, where tunneling between adiabatic states is dynamically frozen. This phenomenon is known as coherent destruction of tunneling [66]. At the opposite end, constructive interference enhances nonadiabatic transitions, resulting in Floquet states being the maximal mix of the adiabatic ones. This is revealed in the quasienergies as the opening of a gap, similarly to a time-independent system with a coupling interaction switched on. A Floquet approach to Cooper-pair pumping was first presented in [28]. It was also the starting point of the theoretical work of Publication VII.

The readout with the pumped charge

As already remarked, information on the quantum dynamics of a CPP can be gained by measuring the pumped charge. Indeed, this is also the case for geometric-phase interferometry. In Fig. 2.9(a), we plot the pumped charge Q_p versus the superconducting phase bias ϕ and the pumping frequency f. The lines drawn on top of the image plot correspond to 90% probability of the system being in the ground state at the end of

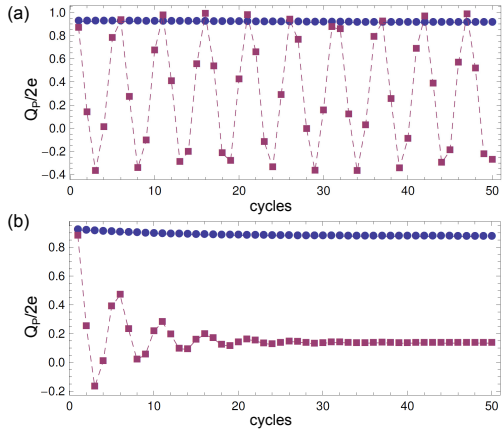

Figure 2.10. Nonadiabatic Cooper-pair pumping with decoherence. Pumped charge per cycle versus time for a case of constructive (squares) and destructive interference (circles), without decoherence (a) and with decoherence induced by a zero-temperature environment (b). The dashed lines are guides for the eye.

the cycle. We have plotted both the predictions of (2.29) (dotted lines) and the numerically exact result obtained by solving the time-dependent Schrödinger equation (dashed lines). As expected, we observe a strong correlation between the ground-state population and the pumped charge. Furthermore, the accuracy of the approximations made in deriving (2.29) is confirmed by the good agreement between analytical and numerical calculations.

In Fig. 2.9(b), we show the time evolution of the ground-state population for one case of constructive and one of destructive interference. In both cases, we witness a population transfer to the excited state after the first avoided crossing. Yet, while constructive interference (solid line) enhances the excitation after the second crossing, destructive interference (dashed line) brings the system back to the ground state. Destructive interference may be exploited in applications, as it acts as a stabilizer for pumping even in a strongly nonadiabatic regime.

The role of the environment

The results of Section 2.4 indicate that observed pumped charge, being a steady-state quantity, critically depends on the dissipation experienced by the pump. Here, we will argue on the visibility of the patterns in the presence of dissipation. First of all, we expect the patterns not to be visible if the coherence time is much shorter than the pumping period,

as in Publication IV. Given the short coherence time of the sluice, this suggests increasing the pumping frequency. In Fig. 2.10 (a) we present the expected pumped charge in the absence of noise over 50 pumping cycles, for both constructive (squares) and destructive (circles) interference. We have considered a charging energy $E_C/k_B = 5$ K and a pumping frequency $f = 0.5\,\mathrm{GHz}$. The results are readily interpreted after Fig. 2.9 (b): When interference is destructive, the system starts each cycle in the ground state, so that the pumped charge is constant. Conversely, constructive interference allows the system to be in different superpositions of the ground and the excited state, and this is reflected in an oscillating pumped charge from cycle to cycle. In Fig. 2.10(b), we include the effects of a weakly coupled, zero-temperature environment, as predicted by the master equation of Refs. [24, 25]. The behavior of the pumped charge in the constructive case changes dramatically, as oscillations are quickly damped. At the same time, the pumped charge in the destructive case is only slightly affected by the environment. This is a direct result of the fact that the system stays mainly in the ground state, whose robustness against decoherence was discussed in Refs. [24, 25]. Most importantly, Fig. 2.10(b) predicts a good visibility for the interference patterns in the presence of weak dissipation.

The behavior of the pumped charge in the presence of a fully nonadiabatic drive and/or with stronger dissipation is also worth some attention. Due to the periodicity of the drive, the dynamics of the pump is best described in terms of Floquet states, that are, dynamic steady states of the Schrödinger equation [65]. In the adiabatic limit, Floquet states reduce to the adiabatic states considered in Section 2.2. The study of Cooper-pair pumping using Floquet theory was pioneered in Ref. [28]. A master-equation formalism combining Floquet theory with dissipation is the starting point of Chapter 5. Applications to the Cooper-pair sluice are discussed in Sections 5.2 and 5.3. In both cases, the Cooper-pair sluice emerges as a suitable tool to study the interplay between drive and environment in driven open quantum systems.

2.6 Flux pumping

All types of CPPs we have considered so far rely on the use of gates as "pistons" to move Cooper pairs on and off the islands. In Publication V, we propose a different scheme for Cooper-pair pumping, which we refer to as

flux pumping (FP). While still based on Coulomb blockade, the FP protocol entails the adiabatic, coherent transfer of a superposition of charge states across a superconducting island. In other words, Cooper pairs are delocalized throughout the pumping process. As a coherent manipulation, FP resembles other adiabatic transfer schemes used in quantum information, in particular, the coherent transfer by adiabatic passage (CTAP) protocol [67, 68, 69, 70, 71]. As a pumping scheme, FP shares some features with parametric pumping in open electron systems [36, 37, 40], sometimes referred to as "quantum pumping". FP thus provides a way to explore quantum pumping in superconducting circuits.

Flux pumping: the principle

FP uses the same "hardware" as the Cooper-pair sluice; however, it exploits a different pulse sequence. In order to achieve FP, the flux pulses must have a finite overlap. A typical pulse sequence for the flux pulses is shown in Fig. 2.11(a). As for the electrostatic gate, it is kept at a fixed potential throughout the pumping cycle. In order to maximize the effect, the gate charge should be close to the degeneracy point, that is, $|\delta n_g| \ll 1$. Furthermore, the device should be phase biased. This is particularly important for FP, as the pumped charge vanishes when averaged over the phase.

In order to illustrate the principle of FP, we first consider the case $\varphi = 0$, which is easier to interpret. At the beginning of the cycle, the island is decoupled from both leads, hence it is in a definite charge state ($|0\rangle$ if $\delta n_g < 0$, $|1\rangle$ if $\delta n_g > 0$), see Fig. 2.11(b). When the left coupling is switched on (sector I), the ground state evolves into a superposition of charge states, provided $J_1 \gtrsim E_C \delta n_g$ [Fig. 2.11(c)]. As a result, charge flows from the left lead into the island. When the left and right coupling are symmetrically swapped (sector II), the Hamiltonian (2.20) does not change, implying [see Eq. (2.14) in Section 2.2] that no charge is transferred between the island and the leads. However, at the end of sector II, the island is coupled to the right lead. Hence, when the coupling is turned down in sector III, the loaded charge is transferred to the right lead. In this scheme, the fact that the dynamics is coherent plays a crucial role. Also notice that the transferred charge is a fraction of a Cooper pair, which is allowed precisely because the leads are phase biased (in contrast to a voltage bias, which would force the leads into a Cooper-pair-number eigenstate).

Under optimal pumping conditions (adiabatic limit, symmetric pulse se-

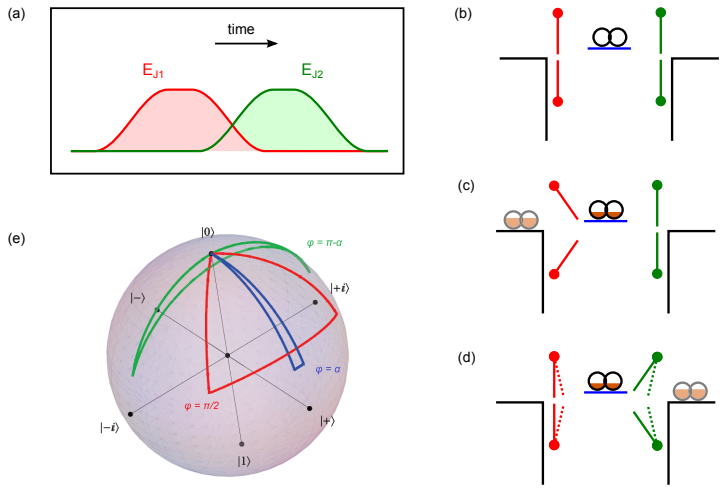

Figure 2.11. Flux pumping. (a) Time modulation of J_l, J_r leading to flux pumping. The gate position is kept fixed throughout the modulation. (b-d) Illustration of the pumping mechanism (at $\varphi = 0$): a fraction of a Cooper pair is attracted to the otherwise empty state on the island (b) by turning the left coupling on (c); as the two coupling are simultaneously switched (d), no charge flows through the island – yet the Cooper-pair fraction now "belongs" to the right lead. (e) Path drawn by the state vector on the Bloch sphere, as the pulse sequence in (a) is applied, for different values of φ (α is a number $\ll 1$).

quence, perfectly tunable SQUIDs), the pumped charge in units of Cooper pairs is given by

$$Q_p[\varphi = 0] = -\frac{1}{2}\mathrm{sgn}(\delta n_g)\left(1 - \frac{1}{\sqrt{1+r^2}}\right) , \tag{2.32}$$

where we have introduced the ratio

$$r = \frac{J_{\max}}{2E_C\delta n_g} . \tag{2.33}$$

The dependence of Q_p on δn_g exhibits a sawtooth behavior; at $\delta n_g = 0$, Q_p discontinuously changes sign as it reaches its maximum absolute value $\frac{1}{2}$. From our heuristic description of the pumping cycle, it is easy to see why the maximum has to be half a Cooper pair. In the most favorable case, the state of the island goes from a definite charge state at the beginning to an equal superposition of charge states at the end of sector I (remember that the gate position is not changed). This corresponds to the limit $|r| \to \infty$ and gives $|Q_P| = \frac{1}{2}$. When $\delta n_g \to 0$, however, also the minimum energy gap $\Delta E_{\min} \equiv \min_{t\in[0,T]} \Delta E(t) = \delta n_g E_C$ tends to zero. This implies that the adiabatic limit, in which (2.32) was derived, is only attained for infinitely slow evolution. We will come back to this point in the following.

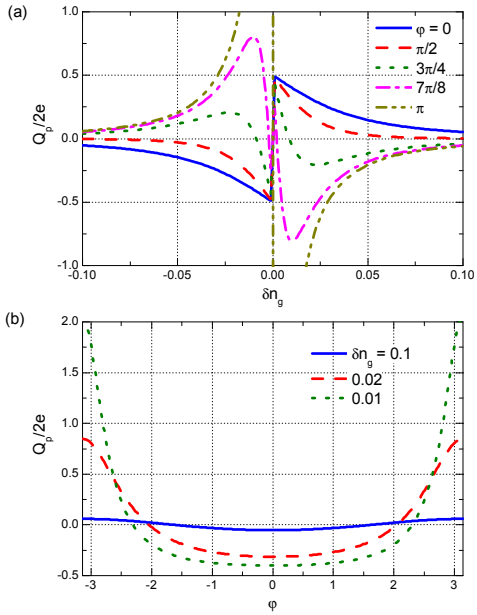

Figure 2.12. Flux pumping: pumped charge in the adiabatic limit. (a) Q_p versus offset charge δn_g for different values of the phase bias φ. (b) Q_p versus φ for different values of δn_g.

A peculiar phase dependence

When $\varphi \neq 0$, the transferred charge in sectors I and III is the same as in the case $\varphi = 0$. This is only to be expected: as long as the island is only coupled to a single lead, the phase difference between the leads cannot play any role. The situation is different for sector II, where the swap of the Josephson couplings now takes place between two leads held at different phases. As a result, an adjustment of the superconducting order parameter on the island is required. This causes an additional current to flow across the island, in a direction opposite to that of the pumping. This current also has a geometric origin, as its integral does not depend on the speed at which the couplings are swapped.

In Fig. 2.12(a), we plot Q_p versus δn_g for different values of φ. When φ is in the range of 0 to $\pi/2$, Q_p simply decreases with respect to the case $\varphi = 0$. As φ is further increased, however, a new trend emerges: Q_p changes its sign with respect to the unbiased case, except in the vicinity of the degeneracy point. The magnitude of the counterflowing Q_p can well exceed a Cooper pair. Finally, at $\varphi = \pi$ the sign of the pumped charge is opposite to that of the unbiased case for all values of δn_g. Furthermore, Q_p diverges as $1/\delta n_g$ for $\delta n_g \to 0$.

The full dependence of Q_p on φ is shown in Fig. 2.12(b) for three selected values of δn_g. In general, one can show that $\langle Q_p \rangle_\varphi = 0$, implying that FP can only be observed in the presence of a well-defined phase bias. These features are peculiar to FP. For comparison, let us recall that in the "ordinary" Cooper-pair sluice, $\langle Q_p \rangle_\varphi = 1$, the phase dependence of Q_p only appears as first-order correction in the small parameter $J_{\min}/J_{\max}$, and no significant dependence on the charge offset δn_g is found as long as the gate modulation crosses the degeneracy point.

For the case $\varphi = \pi$, an analytical result for Q_p is also available:

$$Q_p[\varphi = \pi] = \frac{1}{2}\mathrm{sgn}(\delta n_g)\left(\sqrt{1+r^2} - 1\right) . \tag{2.34}$$

On comparing (2.32) and (2.34), we see that the pumping direction for $\varphi = \pi$ is always opposite to that for $\varphi = 0$. From (2.34), it is also apparent that Q_p diverges when $r \to \infty$ (or $\delta n_g \to 0$). Once again, we recall that (2.34) was derived in the adiabatic limit. Its range of validity is determined by the condition $\alpha \ll 1$, where α is the adiabatic parameter defined in (2.5). As $r \to \infty$, it turns out that the pumping period τ should be increased according to $\tau \propto r^2$ for the adiabatic condition to be satisfied. In other words, the increase in Q_p comes at the cost of an increasingly long τ.

Adiabatic breakdown and optimal pumping frequency

In this section, we investigate the behavior of the pumped charge beyond the adiabatic limit. We focus on the pumped charge Q_p^{st} at dynamic steady state, as this is the relevant quantity for the experiments. In order to brings the system into the steady state, we weakly couple the pump to a zero-temperature environment [24, 25]. In Fig. 2.13, we plot Q_p^{st} versus δn_g for the cases $\varphi = 0$ (a) and $\varphi = \pi$ (b). We choose the realistic device parameters $E_C = 1\,\mathrm{K}, J_{\max} = 0.1E_C, J_{\min} = 0.03J_{\max}$ and explore different pumping frequencies (solid lines). The adiabatic-limit, $J_{\min} = 0$ predictions (2.32) and (2.34) are also plotted for comparison (dashed lines). In general, nonadiabatic transitions result in a decrease of Q_p. For the case $\varphi = 0$ [Fig. 2.13(a)], this results in a smearing of the adiabatic sawtooth. The effect is even more dramatic when $\varphi = \pi$ [Fig. 2.13(b)], with higher frequencies hitting the nonadiabatic onset first. These results indicate that nonadiabatic effects must be taken into serious consideration in any practical implementation of FP. A relevant figure of merit for optimization is the average geometric current $\langle I_p \rangle = fQ_p$, as this is the signal to be detected in a realistic readout scheme. An example of such optimization

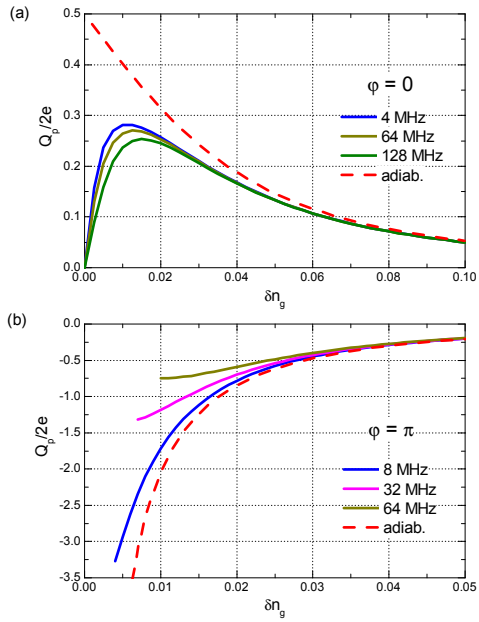

Figure 2.13. Flux pumping: breakdown of adiabaticity. Q_p versus δn_g for $\varphi = 0$ (a) and $\varphi = \pi$ (b), for different pumping frequencies f (solid lines). The results are obtained by numerical integration of the master equation of Ref. [24] and a residual Josephson coupling $J_{\min} = 0.03 J_{\max}$ is considered. The corresponding predictions for the adiabatic limit, (2.32) and (2.34), are plotted for comparison (dashed lines).

is presented in the Appendix of Publication V.

3. Quantum dot thermometry for two-dimensional-electron-gas domains

This chapter is organized as follows. In Section 3.1 we motivate the need for an accurate, non-invasive thermometer for two-dimensional electron gases (2DEGs) cooled down to very low temperatures. In Section 3.2 we give a brief overview of quantum dot (QD) thermometry. In Section 3.3 we report on the measurements of Publication I, where a QD is used to probe the temperature of micrometer-sized electronic domain. In Section 3.4 we introduce the nongalvanic (contactless) QD thermometer proposed in Publication VI and report on its realization in Publication VIII.

3.1 Introduction and motivation

The availability of high-mobility 2DEGs [72], combined with the ability to cool them down to very low temperatures [73], has led to the discovery of outstanding physical phenomena, such as the integer and fractional quantum Hall effect [74, 75]. Achieving even lower temperatures (say, below 1 mK) would open the way to a range of experiments of fundamental relevance for which ultralow temperatures are a sine qua non. Prominent examples include nuclear-spin and highly-correlated quantum phases in low-dimensional electron systems [76, 77], multiple-channel Kondo physics [78, 79, 80], topologically protected quantum computation with the $\nu = 5/2$ fractional quantum Hall state [81, 82], only to name a few.

Cooling the 2DEG down to such low temperatures is an extremely challenging task, as the thermal coupling between the 2DEG and the phonons of the host lattice is strongly suppressed at low temperatures. As a result, parasitic heat loads that would be negligible at higher temperatures – due, for instance, to electrical noise as well as unfiltered blackbody radiation from the hotter environment – can cause significant overheating.

Given this limitation, it is not surprising that in many experiments on 2DEGs the reported electronic temperatures are significantly higher than the base temperature of the cryostat (tens of mK and a few mK, respectively).

With a frozen electron-phonon interaction, cooling of the 2DEG primarily takes place via the electrical contacts. Therefore, thermalization of the contact wires is of paramount importance. For instance, the $4\,\mathrm{mK}$ electron temperature achieved in Ref. [73], still one of the lowest to date, is the result of a brute-force thermalization strategy: sintered silver heat exchangers were directly soldered to the indium contacts to the 2DEG and immersed into a cell filled with 3-He and cooled down to 0.5 mK by a nuclear demagnetization stage. A conceptually similar yet distinct scheme, recently developed and tested in Refs. [83, 84, 85], is based on integrating a Cu nuclear refrigerator into each individual wire.

A different approach to the challenge of cooling 2DEGs to sub-mK temperatures is provided by electronic refrigeration [86]. While driving an electrical current through the system, electronic coolers replace high-energy ("hot") electrons with lower-energy ("cold") ones. As a result, they make the electron energy distribution sharper, which amounts to cooling. One way to selectively remove hot electrons is to exploit a system or material with a gap in the density of states at the Fermi energy. Superconductors are a prototypical example. Electron coolers based on normal metal-insulator-superconductor (NIS) tunnel junction have been investigated for more than 20 years; for a review, see Ref. [87]. In 2DEGs, a similar role can be played by QDs, as theoretically envisaged by Edwards *et al.* [88, 89]. A quantum-dot-based electronic refrigerator operating at $250\,\mathrm{mK}$ was demonstrated in Ref. [90].

As the temperature of the 2DEG can significantly differ from that of the lattice phonons, the question arises how to accurately measure it. Such a measurement requires using either a primary thermometer, that is, a thermometer whose output signal can be directly converted into absolute temperature, or a secondary thermometer that can be calibrated at higher temperatures, where electrons are expected to be well thermalized, and whose behavior can be safely extrapolated down to lower temperatures. Furthermore, the extremely low thermal budget the 2DEG can afford puts a bound on the power the thermometer itself can dissipate before it acts as a source of overheating. This issue is particularly critical for 2DEG domains of small size (tens of $\mu\mathrm{m}^2$), such as the one considered in Ref. [90].

In this Chapter, we present the development of noninvasive, primary thermometry schemes for micrometer-sized 2DEG domains, based on QDs and quantum point contacts (QPCs). It is well known [91, 92, 93] that the temperature-dependent conductance of a QD near a Coulomb-blockade peak can be used for thermometry. Measurements of the temperature of bulk 2DEGs using transport spectroscopy of QDs have been routinely reported down to very low temperatures [94, 80, 95]. In Publication I, we employ a variation on this scheme. In our device, the QD is coupled to two 2DEG domains – one fairly small, the other very large – held at different temperatures. The standard way to probe these two temperatures would be to apply a finite bias across the dot, thereby aligning the resonant level of the dot to one lead at a time. By contrast, we demonstrate that if the temperature gradient across the dot is large, then the two temperatures can be both extracted from a single zero-bias measurement, due to the change in the line shape of the Coulomb-blockade peak. In Publication VI, we analyze a contactless version of the QD thermometer, where the mean charge state of the dot is read out by a QPC. This technique, originally proposed in [96], is particularly suited for low temperatures and small domains, as it dissipates – ideally – no power in the domain. It was demonstrated independently in Ref. [97], down to $120\,\mathrm{mK}$ 2DEG temperature, and in Publication VIII, down to $45\,\mathrm{mK}$. Recently, the same technique was used in the set-up of Ref. [84] to measure 2DEG temperatures as low as 11 mK [85].

3.2 Quantum-dot thermometry

The theory of Coulomb-blockade oscillations in the conductance of a QD was developed by Beenakker [91]. In this section, we derive a few results that are useful for thermometry.

The situation we consider is depicted in Fig. 3.1. The QD is coupled to two leads, indexed by $i = 1, 2$. The leads are ideal charge reservoirs held at constant chemical potentials μ_1, μ_2. The density of states is constant around the Fermi energy and the states are occupied according to the thermal distributions f_1, f_2 corresponding to temperatures T_1, T_2. As for the QD, both the charging energy E_C and the orbital level spacing $\Delta\epsilon$ are much larger than the thermal energy $k_B \max(T_1, T_2)$ in the leads. As a result, the state occupation of the QD is fixed for all but one single state, whose energy ϵ is varied with respect to μ_1, μ_2 by acting on the gate volt-

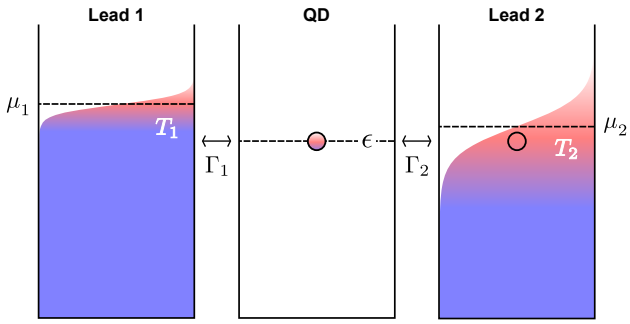

Figure 3.1. Transport across a temperature-biased QD. Energy-level diagram for transport across a temperature-biased QD in the "quantum" Coulomb blockade regime (all quantities are defined in the text).

age. The tunnel coupling between the QD and the leads, described by the rates Γ_1, Γ_2, is assumed to be weak. In particular, this implies that (i) electron tunneling is sequential and higher-order transitions (cotunneling) can be neglected, and (ii) the energy broadening $h\Gamma$ of the QD level due to its finite lifetime is negligible as compared to the thermal linewidth $k_B \min(T_1, T_2)$. Finally, the calculation is slightly different depending on whether the level is nondegenerate or spin-degenerate. In the following, we will consider the nondegenerate case for simplicity; similar results for the spin-degenerate case are briefly discussed in Publication I.

Under this set of assumptions, the occupation probability p_1 evolves according to the master equation

$$\frac{dp_1}{dt} = -(\Gamma^1_{1\to 0} + \Gamma^2_{1\to 0})p_1 + (\Gamma^1_{0\to 1} + \Gamma^2_{0\to 1})(1 - p_1) \,, \tag{3.1}$$

where we have introduced the transition rates $\Gamma^i_{0\to 1}$ and $\Gamma^i_{1\to 0}$ for an electron tunneling on and off, respectively, between the i-th lead and the island. In particular:

$$\begin{aligned} \Gamma^i_{0\to 1} &= \Gamma_i f_i(\epsilon) \\ \Gamma^i_{1\to 0} &= \Gamma_i [1 - f_i(\epsilon)] \end{aligned} \tag{3.2}$$

where

$$f_i(\epsilon) = \left[\exp\left(\frac{\epsilon - \mu_i}{k_B T_i} \right) + 1 \right]^{-1} \,. \tag{3.3}$$

For a given occupation, the charge flow between the i-th lead and the dot is given by

$$I_i = -e \left[(1 - p_1)\Gamma^i_{0\to 1} - p_1 \Gamma^i_{1\to 0} \right] \,. \tag{3.4}$$

At steady state, we set $dp_1/dt = 0$ and find

$$p_1 = \frac{\Gamma_1 f_1(\epsilon) + \Gamma_2 f_2(\epsilon)}{\Gamma_1 + \Gamma_2} \tag{3.5}$$

The steady-state current I is given by ($I = I_1 = I_2$)

$$I = -e\frac{\Gamma_1\Gamma_2}{\Gamma_1 + \Gamma_2}\left[f_1(\epsilon) - f_2(\epsilon)\right] \tag{3.6}$$

In the experiments, we often measure the differential conductance $G = \partial I/\partial V_b$, with $V_b = (\mu_2 - \mu_1)/e$. Assuming a symmetric voltage drop across the two barriers, we obtain

$$\begin{aligned} G &= e^2\frac{\Gamma_1\Gamma_2}{\Gamma_1 + \Gamma_2}\left[f_1'(\epsilon) + f_2'(\epsilon)\right] \\ &= e^2\frac{\Gamma_1\Gamma_2}{(\Gamma_1 + \Gamma_2)}\sum_{i=1}^{2}\frac{1}{4k_BT_i}\cosh^{-2}\left(\frac{\epsilon - \mu_i}{k_BT_i}\right) . \end{aligned} \tag{3.7}$$

Equation (3.7) is a central result for transport-based QD thermometry. Its implications can be summarized as follows: as the gate voltage is swept, the QD conductance probes the derivative of the distribution functions in the leads.

In Fig. 3.2, we demonstrate the use of (3.7) in three different cases. First of all, if $T_1 = T_2 \equiv T$, the conductance at zero bias reads

$$G = e^2\frac{\Gamma_1\Gamma_2}{(\Gamma_1 + \Gamma_2)}\frac{1}{2k_BT}\cosh^{-2}\left(\frac{\epsilon}{k_BT}\right) . \tag{3.8}$$

Sample conductance traces are shown in Fig. 3.2(a) for different values of the common temperature, in suitably normalized units. The FWHM of the conductance peak is given by

$$(\Delta\epsilon)_{\mathrm{FWHM}} = k_BT\log\frac{3 + 2\sqrt{2}}{3 - 2\sqrt{2}} . \tag{3.9}$$

Equation (3.9) shows that the QD thermometer is a primary thermometer, as it directly relates the measured signal to absolute temperature (via a combination of numerical and physical constants). We must recall, however, that a measurement of $\Delta\epsilon_{\mathrm{FWHM}}$ requires an accurate estimation of the "lever arm" of the gate $\alpha = \epsilon/(eV_g)$ in order to convert gate voltages into QD energy. This estimation is typically obtained from finite-bias spectroscopy and is probably the most significant source of error in this thermometry scheme. Whether the reliance on the lever arm disqualifies the QD thermometer from being regarded as "primary", it is sometimes a subject of debate. Our view is that it does not – even if the measurement of the lever arm is in essence a calibration, it is not one that requires the presence of a second thermometer, hence the adjective "primary" seems

to us appropriate for a device that can tell absolute temperature without relying on other thermometers.

Equation (3.7) applies just as well when the two temperatures are different, $T_1 \neq T_2$. In this case, two strategies are possible for thermometry. The easiest one is to apply a voltage bias $eV_b = \mu_2 - \mu_1 \gg k_B \max T_1, T_2$ so that the distribution functions of the two leads are probed independently; see Fig. 3.2(b). The main drawback of this scheme is that it injects high-energy carriers ($\approx eV_b$ above the Fermi energy) into the lead whose temperature is not being measured. If the two temperatures are significantly different, $\max(T_1, T_2)/\min(T_1, T_2) \gtrsim 1$, then a zero-bias measurement is a viable alternative, as the functional dependence (3.7) allows us to tell both T_1 and T_2 from a single conductance peak. This can be qualitatively seen in Fig. 3.2(c): the tails of the peak are more sensitive to the hottest temperature; the "body" of the peak, to the coldest. An experimental demonstration of this thermometry scheme is provided in Publication I.

3.3 Zero-bias transport thermometry for temperature gradients

In Publication I, we study the local temperature of a micrometer-sized 2DEG domain as it is heated by a known heating power. In order to measure this temperature, which can be significantly different from that of the neighboring 2DEG regions, we use a QD in the quantum Coulomb-blockade regime [see Section 3.2]. QD thermometry in the presence of a temperature bias is usually accomplished by imposing a finite voltage bias across the dot, so that the electronic distributions in the leads are probed one at a time as the resonant levels of the QD cross the respective Fermi energies [85]. In Publication I, we take a slightly different approach and show that a zero-bias measurement is sufficient to probe both temperatures, provided the two of them are significantly different from each other. Such a scheme may be useful for a few reasons. First of all, the QD may be part of a more complex circuit whose behavior is altered by the presence of a finite bias. Secondly, finite-bias thermometry implies a significant amount of overheating in the lead whose temperature is not being probed. This heat load can be undesirable, either because the said lead must itself be kept as cold as possible, or because part of the heat can backflow to the other lead, for instance, via a phonon-based energy-transfer mechanism [98, 99].

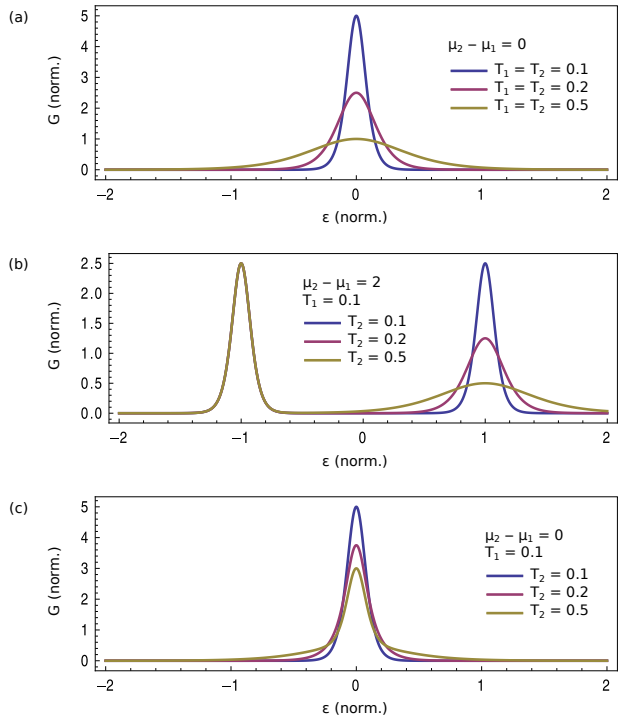

Figure 3.2. Transport-based QD thermometry, as described by (3.7). The QD conductance, plotted against the QD energy, shows the characteristic Coulomb-blockade peaks. (a) If $T_1 = T_2$, a zero-bias measurement tells the common temperature. (b) If $T_1 \neq T_2$ and $eV_b \gg k_B \max(T_1, T_2)$, the two temperatures are probed independently. (c) If $T_1 \neq T_2$ and $eV_b = 0$, the information about the two temperatures is "buried" in the same conductance peak; nonetheless, it can be recovered by considering the functional dependence of (3.7), as demonstrated in Publication I.

Our thermometry scheme gives us access to the steady temperature of the 2DEG in the presence of a given heat load. This temperature is the result of a balance between the injected power and the heat leakages through all possible thermal relaxation channels. In our case, two channels must be considered, namely, electronic heat conductance through the QPCs defining the domain and inelastic scattering between the electrons in the domain and the phonons of the lattice. Thanks to the high degree of tunability of our device, we can control the electronic heat conductance over a broad range and realize regimes where either one or the other channel prevails. Strong experimental evidence for this claim is provided by the different temperature dependence of the two channels. In the regime where the electronic heat conductance dominates, the heat outflow follows the Wiedemann-Franz law ($\dot{Q} \propto T^2$) and our data are quantitatively accounted for by a model with no free parameters. In the opposite regime, our data are consistent with a thermal relaxation model based on the screened electron-acoustic phonon piezoelectric interaction, which is expected to dominate below 1K and gives a temperature dependence $\dot{Q} \propto T^5$. Our estimate for the corresponding coupling constant – measured, to the best of our knowledge, for the first time in such a small domain – is not far from other values reported in literature [100].

These results contribute to our understanding of heat flows in 2DEG microdomains and to our ability to measure them. They can be relevant, for instance, to the design of the QD refrigerator discussed at the beginning of this chapter [88, 89, 90]. Finally, our thermometry technique could be applied to other systems characterized by different electronic and phononic properties, for instance, InGaAs alloys with high In content [101] or semiconductor nanowires [102, 103].

A tunable platform for heat-transport experiments in 2DEGs

Figure 3.3 shows a scanning electron micrograph of the device used in Publication I. The substrate is a GaAs/AlGaAs heterostructure. The 2DEG, defined 100nm below the surface, is characterized by a density $n_s = 2.26 \times 10^{11}\,\mathrm{cm}^{-2}$ and a mobility $\mu = 3.31 \times 10^6\,\mathrm{cm}^2/\mathrm{Vs}$. By applying a negative voltage to the surface gates, we locally deplete the 2DEG. As a result, we can define a central domain of area $A_D = 16\,\mu\mathrm{m}^2$. The domain (red) is connected to four neighboring 2DEG regions (blue) by one QD and three QPCs (two additional gates, defining a second QD, were not used). The four regions are contacted by low-resistance Ohmic contacts (squares). The gate design,

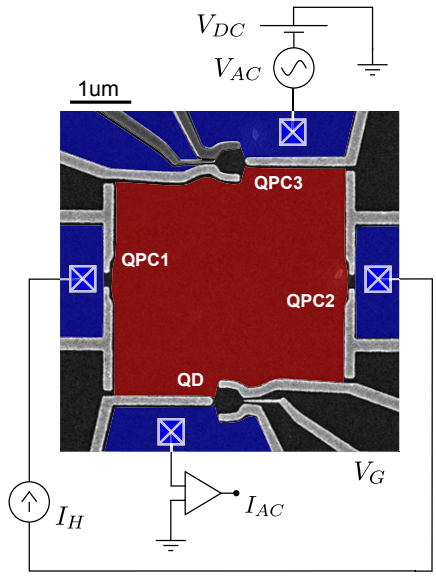

Figure 3.3. A platform for heat-transport experiments in 2DEGs. False-color scanning electron micrograph of the device and scheme of the measurement setup. Schottky gates (light gray) define a $16\,\mu m^2$ sized central electronic domain connected to outer regions of the 2DEG through a QD (bottom) and three QPCs (left, right, top). Crossed squares indicate Ohmic contacts to the 2DEG.

comprising 12 independent gates, was aimed at providing maximum tunability to each quantum feature, including the QPCs and the QD barriers. Two small, "plunger" gates are used to tune the chemical potential of each dot. The QD geometry was chosen in order to maximize its charging energy E_C and its single-particle energy spacing δE. In the diamonds with lowest occupation number we measured $E_C = 1.5\,\mathrm{meV}$ and $\delta E \approx 0.4\,\mathrm{meV}$. The estimated energy-level spacing associated with the lateral confinement of the domain is $400\,\mathrm{neV} \approx 5\,\mathrm{mK}/k_B$, so that the 2DEG domain can still be regarded as a Fermi gas. Due to the small size, the charging energy of the domain is significant (we estimate it to be of the order of tens of $\mu\mathrm{eV}$ [90]). While its impact was negligible on the low-bias, relatively-high-temperature measurements of Publication I, such a high charging energy can affect QD thermometry and refrigeration at lower temperatures. One way to decrease it would be to fabricate a large top gate extending over the domain, as done in Ref. [104]. Such a gate could also be used to tune the electron density in the domain.

An architecture similar that of Fig. 3.3 is suitable for a broad range of experiments on heat management at the nanoscale, besides and beyond those reported in Publication I. A list of subjects should include electronic refrigeration [90], thermoelectric effects in QDs and QPCs [105, 106, 107], asymmetric dissipation in a strongly biased QPC [98] and nonthermal electron distributions. Finally, an entire class of different effects could be addressed, also from the point of view of heat manipulation, in the presence of quantizing magnetic fields.

Two-temperature thermometry at zero bias

The measurements of Publication I were carried out in a ^{3}He cryostat down to $250\,\mathrm{mK}$, in the configuration schematically shown in Fig. 3.3. We heated the domain by driving a dc current I_H through the QPC1-domain-QPC2 circuit; at the same time, we measured the zero-bias differential across the QPC3-domain-QD circuit.

Figure 3.4(a) shows the measured zero-bias conductance G versus gate voltage V_g around a Coulomb-blockade peak, for different values of the heating current I_H. We set the working point of the QPCs so that $R_{QPC1,2,3} \simeq 7.4\,\mathrm{k}\Omega$. The full lines are a fit of the model of Section 3.2 to the experimental points. As we tuned the QD barriers to be symmetric, we can assume $\Gamma_1 = \Gamma_2$. We measured the conversion factor between V_G and the dot energy ("level arm") by finite-bias spectroscopy (Coulomb-blockade "dia-

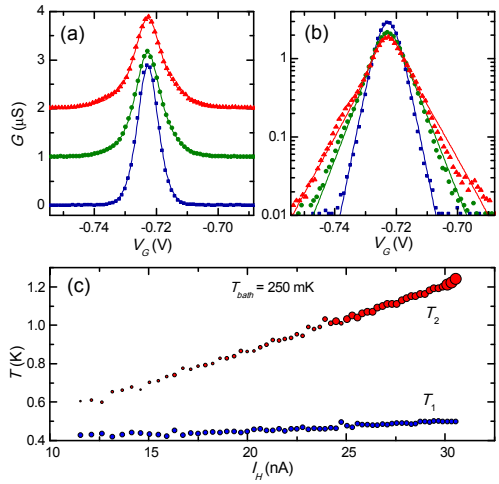

Figure 3.4. Two-temperature QD thermometry. (a,b) Conductance G versus gate voltage V_G for increasing values of the heating current I_H: $11.6\,\mathrm{nA}$ (squares), $20\,\mathrm{nA}$ (circles), $28.6\,\mathrm{nA}$ (triangles). The theoretical model is fitted to the data (full lines) and the two temperatures T_1, T_2 are extracted as fit parameters. The same data are plotted on both linear (a) and logarithmic scale (b). (c) Extracted T_1 and T_2 as a function of I_H.

monds") [93] within 5% accuracy. This allows us to fit the model to the line shape of the peak with the two temperatures T_1 and T_2 ($T_2 > T_1$) as the only free parameters. The same data is also plotted in logarithmic scale, see Fig. 3.4(b), to highlight the sensitivity of the peak tails to the higher temperature. This sensitivity provides a basis for our thermometry scheme. In Fig. 3.4(c), we plot the extracted T_1 and T_2 as a function of I_H. While both temperatures increase with I_H, the increase in the hotter T_2 is much more pronounced. We hence assign $T_2(I_H)$ to the central domain and $T_1(I_H)$ to the adjacent 2DEG region. There is a ~ 150 mK difference between the cryostat base temperature (250 mK) and the coldest T_1, which we ascribe to heating of the 2DEG by noise. The additional increase of T_1 with I_H may be due to local heating of the phonon lattice.

Heat flows in the 2DEG microdomain

Our thermometry scheme can be used to investigate heat-relaxation mechanisms in the 2DEG domain. Indeed, the steady-state T_2 is the result of a thermal balance. Our thermal model, sketched in Fig. 3.5(a), is described by the equation

$$\sum_{i=1}^{3} \dot{Q}_{\mathrm{QPC,i}} + \dot{Q}_{\mathrm{e-ph}} + P_0 = 0\,. \tag{3.10}$$

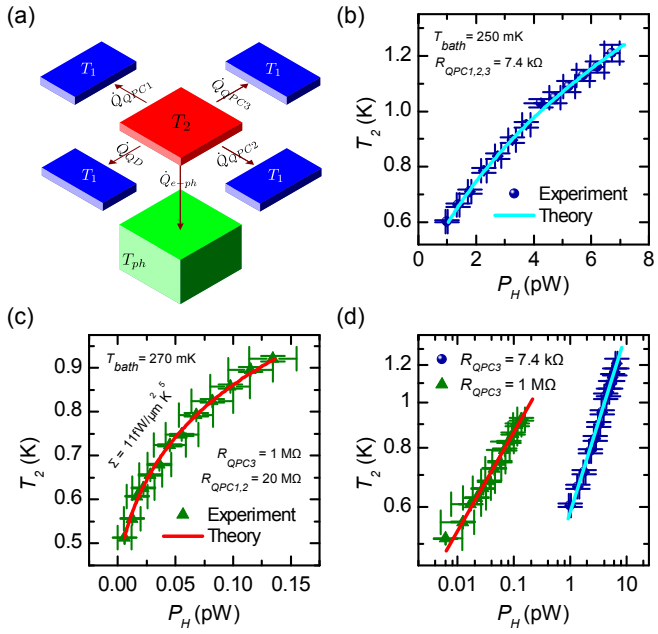

Figure 3.5. Heat flows in a 2DEG microdomain. (a) Main contributions to the thermal balance equation (3.10). (b-c) Hot temperature T_2 versus injected power P_H for different configurations of the device: $R_{\mathrm{QPC},1,2,3} = 7.4\,\mathrm{k\Omega}$ (b) and $R_{\mathrm{QPC},1,2,3} > 1\,\mathrm{M\Omega}$ (c). The full lines are fits of the expressions given in the text, implying that a different heat-relaxation mechanism prevails in each case. (d) Joint bi-logarithmic plot of (b) and (c), highlighting the different power laws obeyed by the two datasets.

Here, $\dot{Q}_{\mathrm{QPC,i}}$ denotes the heat current flowing through the i-th QPC and into the domain, $\dot{Q}_{\mathrm{e-ph}}$ results from inelastic scattering between the electrons in the domain and the lattice phonons (the latter in equilibrium at base temperature T_b), P_0 accounts for a spurious heat power overheating the domain, and we have neglected the heat flow through the QD due to its very high impedance. $\dot{Q}_{\mathrm{QPC,i}}$ can be written as [108, 109]

$$\dot{Q}_{\mathrm{QPC,i}} = -\frac{1}{2} V_{\mathrm{QPC,i}} I_{\mathrm{QPC,i}} + \frac{L_0}{2R_{\mathrm{QPC,i}}} \left[T_2^2 - T_1^2\right] \tag{3.11}$$

where $V_{\mathrm{QPC,i}}$, $I_{\mathrm{QPC,i}}$ are the voltage drop across and the current through the i-th QPC, respectively, and $L_0 = \pi^2 k_B^2/3e^2$ is the Lorenz number. We can rewrite the first term in (3.10) as

$$\sum_{i=1}^{3} \dot{Q}_{\mathrm{QPC,i}} = \frac{1}{2} I_H V_H + \frac{3L_0}{2R_{\mathrm{QPC}}} \left[T_2^2 - T_1^2\right] \tag{3.12}$$

where V_H is the voltage drop across the heating circuit and we have used the fact that all QPCs are tuned to the same impedance R_{QPC}. Let us now turn to $\dot{Q}_{\mathrm{e-ph}}$. At low temperatures and for III-V semiconductor alloys, piezoelectric coupling is expected to dominate over deformation-potential interaction at subkelvin temperatures, resulting in the energy-loss rate [110]

$$\dot{Q}_{\mathrm{e-ph}} = \Sigma A_D \left(T_2^5 - T_b^5\right) \ , \tag{3.13}$$

where we have assumed that the lattice phonons are thermalized at the bath temperature T_b and Σ is a coupling constant which depends on the electron density and on the material parameters of the host lattice.

In Fig. 3.5(b), we replot T_2 from Fig. 3.4(c) against the injected power $P_H = \frac{1}{2} I_H V_H$. The data are well described by the power law $P_H = -P_0 + B(T_2^2 - T_1^2)$. From the fit (full line) we extract $P_0 = (0.15 \pm 0.02)\,\mathrm{pW}$ and $B = (5.0 \pm 0.1)\,\mathrm{pWK^{-2}}$, in excellent agreement with the $4.9\,\mathrm{pWK^{-2}}$ prediction for the heat leakage through three QPCs of equal resistance $7.4\,\mathrm{k\Omega}$. In this regime, heat flow through the QPCs dominates over electron-phonon heat exchange. By increasing the resistance of the QPCs, one can make the former contribution negligible. The results of such a measurement are shown in Fig. 3.5(c), where the impedance of each QPC was tuned to the $\mathrm{M\Omega}$ range. The full line is a fit of the power law $P_H = -P_0 + D(T_2^5 - T_{ph}^5)$, demonstrating the transition to a regime where heat relaxation relies on coupling to the phonon bath. This is manifest in the joint log-log plot of Fig. 3.5(d), where the two datasets are characterized by different exponents as well as by a different order of magnitude for P_H. The best-fit

values for Fig. 3.5(c) are $P_0 = (5 \pm 1)\,\mathrm{fW}$ and $D = (170 \pm 20)\,\mathrm{fWK}^{-5}$. Notice that P_0 is strongly suppressed compared to the previous case, thanks to the high impedance of the QPCs. Assuming for our domain the area $A_D = 16\,\mu\mathrm{m}^2$, we obtain for the electron-phonon coupling constant the value $\Sigma = (11 \pm 1)\,\mathrm{fW}\mu\mathrm{m}^{-2}\mathrm{K}^{-5}$. This is about three times smaller than the theoretical prediction $\Sigma \approx 30\,\mathrm{fW}\mu\mathrm{m}^{-2}\mathrm{K}^{-5}$ (see Publication I for details) and about two times smaller than what was previously measured [100]. We do not know the reasons for this discrepancy. It is worth noticing that our results were obtained for a micrometer-sized, as opposed to bulk, domain, where the effects of confinement can be important. Among possible sources of uncertainty, we mention the lever arm of the QD, the effective area relevant for the electron-phonon interaction, and the average electron density inside the domain.

3.4 Contactless thermometry based on charge sensing

The thermometry technique described in the previous section may well be sufficiently unobtrusive for many applications, including temperature measurements of large domains and/or at temperatures above 100 mK. However, based on a transport measurement, this technique unavoidably entails dissipation. Dissipation in the domain is associated to the tunneling of hot quasiparticles, contributing a heat flow $\dot{Q}_R = \Gamma E f(E)$, where Γ is the tunneling rate for the resonant level of the dot, E its energy (with respect to the Fermi energy of the domain), and f the electron distribution function in the domain (say, a Fermi function at temperature T_e). In order to sample f, we must vary E at least in the range of $-3k_BT_e$ and $3k_BT_e$. Averaging over such a sweep, we obtain $\langle \dot{Q}_R \rangle \approx 0.55\Gamma k_B T_e$. The admissible values for the tunneling rate Γ – which, we recall, can be adjusted over a broad range by acting on the QD barriers – are bounded from below by the lowest measurable current (typically, $e\Gamma \gtrsim 1\,\mathrm{pA}$) and from above by the requirement that the intrinsic (Lorentzian) broadening of the Coulomb-blockade peak be negligible as compared to the thermal broadening ($h\Gamma \ll k_BT/e$). For temperatures of hundreds down to tens of mK, a reasonable value is $\Gamma \approx 100\,\mathrm{MHz}$.

In order to determine whether the resulting $\langle \dot{Q}_R \rangle$ is acceptable, we must compare it to the cooling power provided by all relevant heat-relaxation channels. For definiteness, let us consider a GaAs/AlGaAs 2DEG domain as in Fig. 3.3. In Fig. 3.6, we plot the steady-state T_e for 1 and $100\,\mu\mathrm{m}^2$-

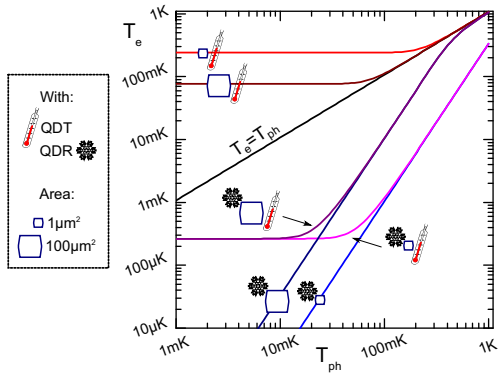

Figure 3.6. The "dissipative" QD thermometer. Steady-state electron temperature T_e versus phonon bath temperature T_{ph}, for domains of different areas, in the presence of a QD thermometer, a QD refrigerator, or both. Parasitic heat loads on the system are not taken into account (see text).

sized domains, versus the phonon-bath temperature $T_{\rm ph}$. T_e is obtained by solving a thermal-balance equation similar to (3.10). The straight line marked $T_e = T_{ph}$ is plotted for reference, and stands for the case where no additional heat load is put on the domain. As soon as the thermometer is introduced, the situation changes dramatically: T_e follows T_{ph} only down to about 100 mK and then saturates, due to the weakening of the electron-phonon interaction. We also consider the case where an ideal quantum-dot refrigerator is used to cool the domain. In this case, much lower temperatures can be obtained ($\approx 1\,\mathrm{mK}$), regardless of the domain area. In this case, the competition is between the dissipation induced by the thermometer and the cooling power of the refrigerator, the phonon bath playing little or no role. Quite obviously, this analysis should be taken with a grain of salt, as it neglects parasitic heat sources (one of the most severe limitations in achieving such low temperatures), nonidealities in the refrigerator and nonequilibrium effects in the 2DEG. However, it indicates a fundamental limitation of transport-based QD thermometry.

Proposal

In Figure 3.7 we compare two schemes for QD thermometry. In panel (a) we show the usual, transport-based scheme. In panel (b) we show a "nongalvanic" or "contactless" variation on this scheme, which we analyzed in Publication VI. In both schemes, the strongly nonlinear density of states of a QD is exploited to probe the energy distribution of the domain. All the difference lies in the way this information is read out: instead of

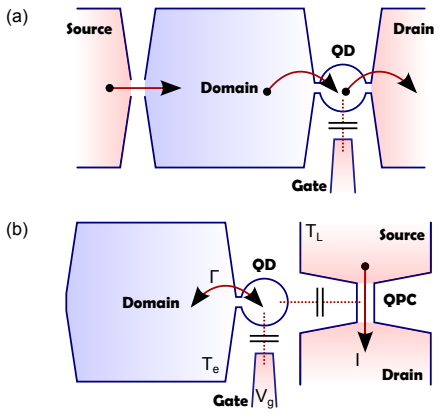

Figure 3.7. Galvanic (a) versus nongalvanic (b) QD thermometer. In (a), temperature is determined by the linewidth of Coulomb-blockade peaks, obtained from a transport measurement. In (b), from the average occupation of the dot, read out in a nongalvanic fashion by a QPC placed nearby.

performing a transport measurement across the dot, we measure its average occupation in a nongalvanic fashion with the help of a QPC placed nearby. This scheme combines two established techniques: QD thermometry, which we have discussed in detail in this Chapter, and charge sensing with a QPC [111, 112, 113]. If the gate sweep is performed adiabatically, then the heat flow into the domain vanishes, making this device appealing for temperature measurements of ultracold electron domains.

The operation of the nongalvanic thermometer can be quantitatively modeled as in Fig. 3.8. On the one hand, the mean occupation of the QD $\langle n_{QD} \rangle$ changes by one as the energy ϵ_d of the relevant energy level in the dot crosses the Fermi energy μ_0 of the domain, the linewidth of this transition being directly related to the temperature T_e of the domain. On the other hand, a change in the dot occupation affects the potential landscape of the neighboring QPC, and hence its conductance. Finally, one has to take into account that a change in the gate voltage V_g affects the chemical potential of the dot as well as the potential of the QPC, as observed in the experiments. For a single active channel and in the linear-response regime, we can write the QPC conductance as

$$G_{\mathrm{QPC}} = \frac{2e^2}{h} \mathcal{T}(\epsilon_q) \,, \tag{3.14}$$

where $\mathcal{T}(\epsilon)$ is the transmission function of the channel and ϵ_q the difference in energy between the bottom of the confining potential in the QPC and the Fermi level in the QPC leads. In the linear response, we can

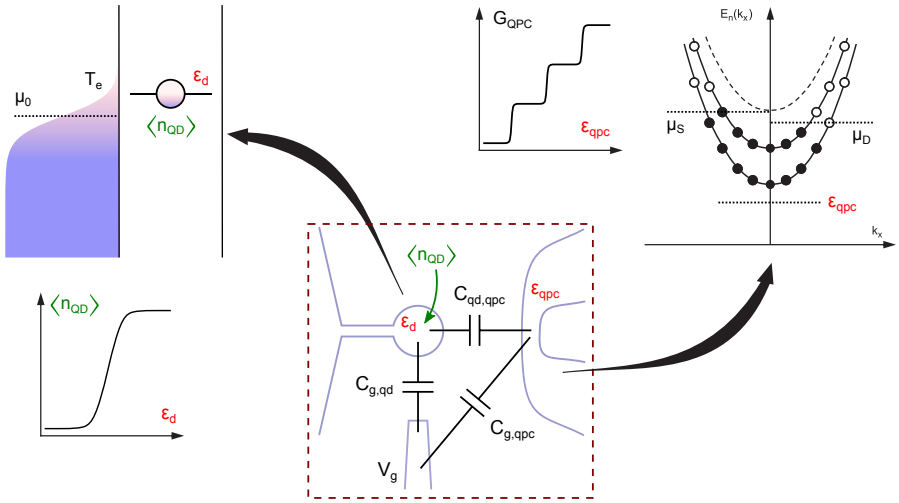

Figure 3.8. A model for the nongalvanic QD thermometer. The central panel shows the capacitively coupled gate, QD and QPC. Left: the occupation of the QD reflects the electron distribution in the tunnel-coupled domain. Right: the QPC conductance depend on the occupation of its subbands, each providing a conductance quantum $2e^2/h$. The QD state affects the confining potential of the QPC, hence the subband occupation, hence the QPC conductance.

write:

$$\epsilon_q = \epsilon_q^0 - 2\beta E_C f(\epsilon_d^0 - e\alpha V_G) - e\gamma V_G \,, \tag{3.15}$$

where ϵ_q^0 and ϵ_d^0 set the working point of the QPC and the position of the QD level, respectively, E_C is the charging energy of the QD, and α, β and γ are "lever arms" between different parts of the circuit.

In terms of the cross and total capacitance introduced in Fig. 3.8, the lever arms can be written as

$$\begin{aligned} \alpha &= \frac{1}{C_{\Sigma,\mathrm{qd}}}\left(C_{\mathrm{g,qd}} + \frac{C_{\mathrm{g,qpc}}C_{\mathrm{qd,qpc}}}{C_{\Sigma,\mathrm{qpc}}}\right) \,, \\ \beta &= \frac{C_{\mathrm{qd,qpc}}}{C_{\Sigma,\mathrm{qpc}}} \,, \\ \gamma &= \frac{1}{C_{\Sigma,\mathrm{qpc}}}\left(C_{\mathrm{g,qpc}} + \frac{C_{\mathrm{g,qd}}C_{\mathrm{qd,qpc}}}{C_{\Sigma,\mathrm{qd}}}\right) \,. \end{aligned} \tag{3.16}$$

The predictions of this model are shown in Fig. 3.9(a), where we plot the QPC current versus V_g for different values of T_e. As V_g is made more negative, I steadily decreases due to the spurious coupling γ between the gate and the QPC. Yet, as the resonant level crosses the Fermi energy of the domain from above, $\langle n_{dot}\rangle$ sharply decreases by one, leading to a step-like increase in I. This gives rise to a sawtooth pattern at zero temperature, which gets progressively smeared as T_e is increased.

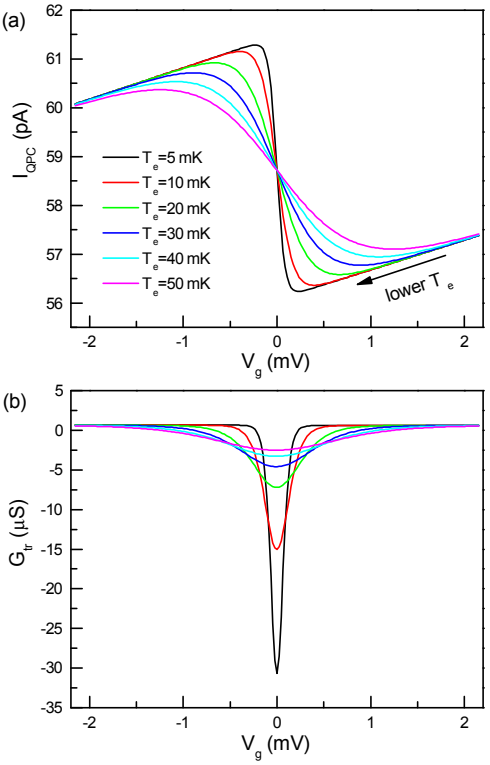

Figure 3.9. Temperature responsivity of the nongalvanic QD thermometer. (a) QPC current I_{QPC} versus gate voltage V_g for different values of the domain temperature T_e; a steeper sawtooth corresponds to a lower T_e. (b) Transconductance G_{tr} versus V_G for the same set of temperatures as in (a); a sharper peak corresponds to a lower T_e.

Besides the QPC current $I_{\rm QPC}$, a relevant quantity for thermometry is the gate-to-QPC transconductance $G_{\rm tr} = dI_{\rm QPC}/dV_g$, which can be directly measured, e.g., with a lock-in amplifier [see Publication VIII]. We can write

$$G_{\rm tr} = \frac{2e^2}{h} eV_b \left.\frac{d\mathcal{T}}{d\epsilon}\right|_{\epsilon_q} \left(\gamma + \alpha\beta E_C \frac{df}{dE}(\epsilon_d^0 - e\alpha V_G)\right) . \tag{3.17}$$

As a function of V_g, a series of dips appear on top of a positive baseline [see Fig. 3(b)]. The dips are proportional to the derivative of the Fermi function, and their FWHM ΔV_g to the domain temperature T_e. In particular:

$$T_e = \frac{e\alpha}{2\log(3+2\sqrt{2})k_B} \Delta V_g . \tag{3.18}$$

The constant relating ΔV_g to T_e is a simple combination of fundamental constants and the lever arm α, which can be determined experimentally from a measurement of the QD charging energy and the cross-capacitance between the gate and the QD. This clearly shows that the nongalvanic QDT, just as well as its "galvanic" version, is a primary thermometer.

More details on the performance of the thermometer, as well as on its limitations, can be found in Publication VI. Here, we just limit ourselves to observing that in the model we have described, the QPC is influenced by the QD state – our readout is based on this – but not the other way around. Strictly speaking, this is inconsistent on both a fundamental and a practical ground. Fundamental, because in quantum mechanics "there is no free lunch" (or measurement). Practical, because any kind of noise in the QPC measurement can easily couple to the QD due to the close proximity of the two quantum devices. We are thus led to consider the measurement "backaction" of the QPC on the QD. This backaction is of (at least) two kinds, as the QD is sensitive to both current fluctuations through the QPC (that is, shot noise) [114, 115, 116, 117] and charge fluctuations in the QPC [118, 119]. Current fluctuations couple to the QD due to finite lead resistance and asymmetric capacitive couplings between the leads and the QD. As a result, they can be minimized by careful circuit design. By contrast, the backaction due to charge fluctuations is fundamentally unavoidable, as it is due to the Heisenberg backaction of the detector (QPC) on the quantum system whose state we are measuring (QD). For a discussion, see Ref. [119]. In Publication VI, we give quantitative estimates for each mechanism. Our conclusion is that none of them limits the operation of the thermometer down to very low temperatures, provided the relevant parameters (biasing point, lead resistance, capacitive

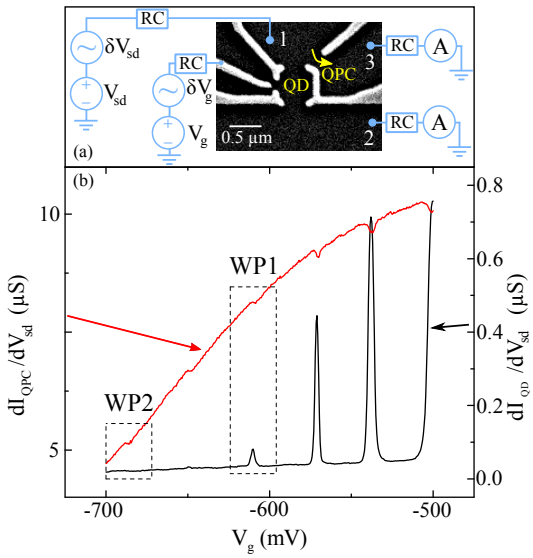

Figure 3.10. Implementation of a nongalvanic thermometer. (a) Micrograph of the device and scheme of the measurement set-up. The lead marked as (1) is voltage-biased while leads (2) and (3) are either left floating or connected to transconductance amplifiers. A varying voltage is applied to the plunger gate, while all other gates are kept fixed at their working-point values. Small ac voltages $\delta V_{\rm sd}$ and δV_g can be applied on top of the dc voltages $V_{\rm sd}$ and V_g to perform lock-in measurements. (b) QPC (red) and QD conductance (black) versus gate voltage V_g.

coupling) are optimized. Phonon-mediated backaction, not considered in Publication VI, may also play a role; see, e.g., Refs. [120, 98, 99, 121].

Experimental demonstration down to $45\,\mathrm{mK}$

In Publication VIII, we experimentally demonstrate nongalvanic thermometry in a bulk 2DEG by directly comparing it against transport-based thermometry, in the temperature range of $800\,\mathrm{mK}$ down to $45\,\mathrm{mK}$. Similar measurements were carried out down to $120\,\mathrm{mK}$ in Ref. [97] and more recently down to $12\,\mathrm{mK}$ in Ref. [85].

In Fig. 3.10, we show a micrograph of the active region of the sample along with a scheme of the measurement set-up. Schottky gates are used to define QD and a QPC. A bias voltage $V_{\rm sd}$ is applied to lead no. 1, which is shared by both the QD and the QPC. The drain currents $I_{\rm QD}$ and $I_{\rm QPC}$, to leads no. 2 and 3, respectively, are measured by grounded transconductance amplifiers. Differential conductance measurements are performed by low-frequency lock-in detection by applying a small ac excitation $\delta V_{\rm sd}$ on top of $V_{\rm sd}$. Measurements of the gate-to-QPC transconductance $G_{\rm tr}$ are similarly performed by applying an ac excitation δV_g to the plunger gate

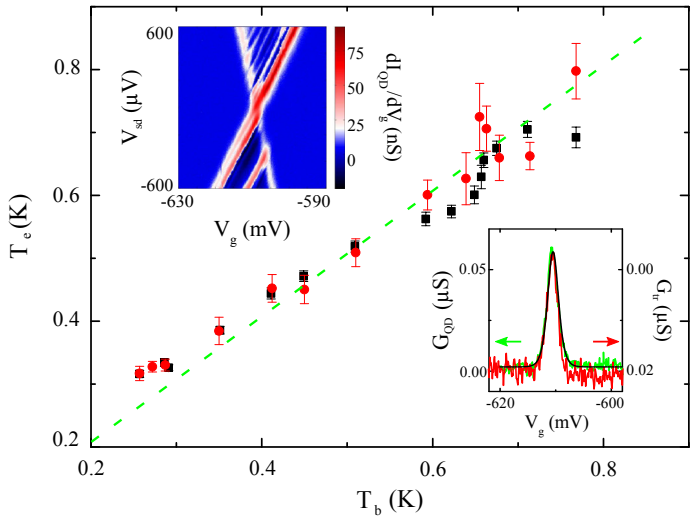

Figure 3.11. Nongalvanic thermometry with "open barriers". The gate is operated at the working point "WP1" (see Fig. 3.10). Electronic temperature T_e versus bath temperature T_b, as extracted from both a transport measurement (black squares) and a charge-detection measurement (red dots). Top Left: finite-bias spectroscopy of the QD around WP1. Bottom Right: comparison between transport ($G_{\rm QD}$ versus V_g, green) and charge-detection measurements ($G_{\rm tr}$ versus V_g, red) at base temperature T_b = 260 mK. The black line is fit of the model expression (3.19).

of the QD. The QPC conductance exhibits the quantized plateaus typical of one-dimensional ballistic transport. Its value is tuned to be half a conductance quantum in order to maximize sensitivity [see Publication VI]. From finite-bias spectroscopy of the QD, we extract a charging energy $E_C \sim 1\,\mathrm{meV}$ and a level spacing $\Delta\epsilon$ of a few hundred $\mu\mathrm{eV}$.

In Fig. 3.10(b), we present simultaneous measurements of the QD and QPC conductance ($G_{\rm QD}$ and $G_{\rm QPC}$, respectively) as a function of the gate voltage V_g, showing a clear correspondence between Coulomb-blockade peaks in $G_{\rm QD}$ and sharp changes in $G_{\rm QPC}$ on top of a smooth background. Some of the features in these plots are due to the common source contact between the QPC and the QD, including the fact that the QPC response depends on the height of the Coulomb blockade peak, or that a finite slope is observed in the off-resonant QD conductance. In the following, $G_{\rm QD}$ and $G_{\rm QPC}$ are independently measured one after the other, with the unused lead left floating. Notice that even in the range where the $G_{\rm QD}$ signal is not sensitive [left of Fig. 3.10], the QPC still functions as a detector, signaling changes in the occupation number of the QD.

We demonstrate the equivalence between the two types of thermome-

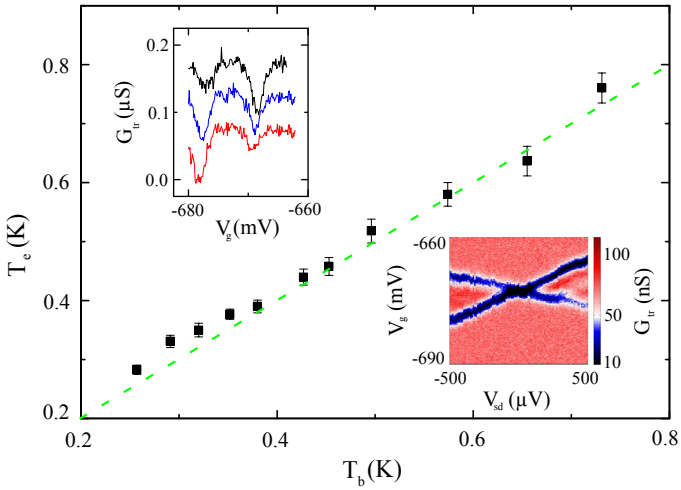

Figure 3.12. Nongalvanic thermometry with "closed barriers". The gate is operated at the working point "WP2" (see Fig. 3.10). Electronic temperature T_e versus bath temperature T_b. Top Left: gate-to-QPC transconductance $G_{\rm tr}$ versus gate voltage V_g for three different configurations of the QD barriers. Bottom Right: color plot of $G_{\rm tr}$ versus V_g and dc bias $V_{\rm sd}$, used to estimate the lever arm at WP2.

try in Fig. 3.11. As we sweep the bath temperature T_b in the range of 250 to $800\,\mathrm{mK}$, the results of transport-based thermometry (black) and charge-detection-based thermometry (red) are in good agreement. Furthermore, the so-determined electronic temperature T_e closely follows the bath temperature T_b, plotted for reference (dashed line). The data were taken around the working point labeled as WP1 in Fig. 3.10(b), where both $G_{\rm QPC}$ and $G_{\rm QD}$ are sensitive to the dot occupation. T_e was estimated from the Coulomb-blockade peak (transport measurement) and from the corresponding QPC-to-gate transconductance dip (charge detection measurement). Around the peak position V_g^0, these two features share the functional dependence

$$y(x) = \bar{y}\cosh^{-2}\left(\frac{V_g - V_g^0}{w}\right) \tag{3.19}$$

where $w = 2k_BT_e/\alpha$. This correspondence is demonstrated in Fig. 3.11, Right Inset, where the two signals $G_{\rm QD}$ and $G_{\rm tr}$, measured at the same temperature and suitably normalized, perfectly overlap (the V_g axis has not been rescaled). In order to measure T_e, we first determine w by fitting each trace to (3.19). The conversion from w into T_e is determined by the lever arm α, which we independently measure by finite-bias spectroscopy around WP1.

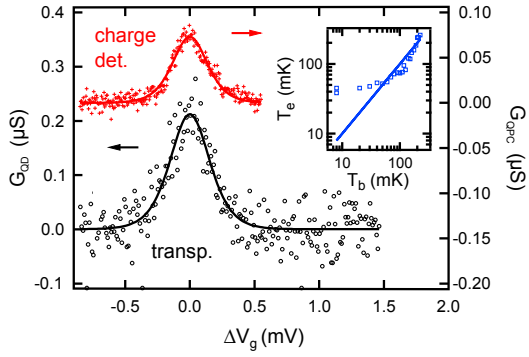

Figure 3.13. Nongalvanic thermometry down to $45\,\mathrm{mK}$. Comparison of charge-detection (red crosses, right axis) and transport thermometry (black open circles, left axis) at 8 mK base temperature. From the model fits (full lines), we extract $T_e = 42 \pm 3.5$ mK (charge detection) and $T_e = 46 \pm 4.5$ (transport). Inset: T_e versus bath temperature T_b, measured with transport thermometry.

After establishing the validity of the nongalvanic technique, in Fig. 3.12, we demonstrate its applicability in the regime of very weak QD tunneling rates, where a transport measurement would be challenging due to the small currents involved (at the fA level). This is done by moving to the V_g range labeled as WP2 in Fig. 3.10. The measured electronic temperatures (squares) are, again, in good agreement with the cryostat temperature down to $250\,\mathrm{mK}$. A technical detail – yet a critical one – concerns how to estimate the lever arm and tune the QD barriers, without relying on a transport measurement. As a matter of fact, the lever arm depends on the confining potential of the QD, which, in turn, depends on the value of V_g. For this reason, the lever arm must be estimated in a configuration as close as possible to the one in which the actual measurement is performed. The data of Fig. 3.10, Insets indicate one way to go. At finite bias voltage, the QPC transconductance exhibits two dips as the chemical potential of the dot is aligned with either lead (Left Inset). The relative strength of the two dips reflects the ratio between the tunneling rates to the two leads, allowing the fine-tuning of the QD barriers. The lever arm can be estimated, even in a very-asymmetric-barrier configuration, by measuring G_{tr} versus V_b and V_g, in a similar way as in the conventional finite-bias spectroscopy (Right Inset).

In order to test our nongalvanic thermometer at lower temperatures, we cooled down the same device in a dilution refrigerator. Figure 3.13 shows measurements taken at $T_b = 8\,\mathrm{mK}$. The nongalvanic measurement (red)

was performed at low tunneling rates and with asymmetric barriers, the transport mesurements (black) in a more conductive regime. The temperature estimates are $T_e = 42 \pm 3.5$ mK and $T_e = 46 \pm 4.5$ mK, respectively, in good agreement but significantly higher than T_b. A full T_e versus T_b plot is shown in Fig. 3.13 for the transport measurement, indicating that the saturation of T_e starts at $T_b \approx 50\,\mathrm{mK}$.

4. Fast thermometry for calorimetric energy detection

This chapter describes our preliminary steps towards a fast microcalorimeter for single-photon detection in the microwave range. In Section 4.1 we motivate our goal from the perspective of quantum thermodynamics and quantum statistical mechanics. In Section 4.2 we provide some background on the transport properties of the normal metal-insulator-superconductor tunnel junction, which we use as a thermometer, and on impedance matching using a lumped-element RLC resonator. In Section 4.3 we discuss a generic thermal model for our calorimeter, which is a nanometer-sized metallic island contacted to superconducting leads. Finally, in Section 4.4 we report on the preliminary experimental results of Publication XI.

4.1 Motivation

The thermodynamics of quantum systems is not as well understood as its classical counterpart. Even in the classical realm, fluctuations of thermodynamic quantities become important for small systems, calling for a suitable extension of the notions of work, heat and entropy production to individual trajectories and nonequilibrium ensembles. Stochastic thermodynamics [122] provides a convenient framework to study these fluctuations. Its predictions, most notably the Jarzynski equality [123] and the Tasaki-Crooks fluctuation relations [124], have been experimentally verified in a variety of physical settings, including single-electron devices [125, 126, 127].

In the last years, much effort has been put into carrying the concepts of stochastic thermodynamics over to the quantum domain; for a review, see Refs. [128, 129]. Despite progress, however, the definition of a key quantity, work, is still under debate [130]. At the heart of this difficulty

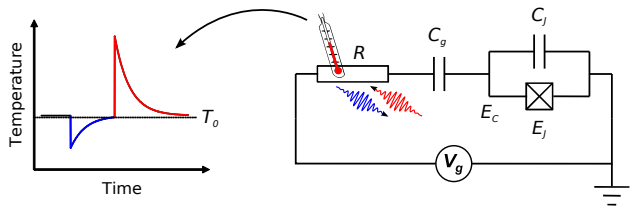

Figure 4.1. Calorimetric measurement of quantum work. A gate-driven Cooper-pair box is capacitively coupled to a resistor acting as the environment. The electronic temperature of the resistor is constantly monitored with a fast thermometer. "Quantum jumps" in the Cooper-pair box are detected as temperature spikes in the resistor.

is the pivotal role of measurement in quantum mechanics. While work is not an "observable" in quantum-mechanical sense [131], its definition in terms of a double projective measurement, which prevails in literature [129], "forces" the system to start in a defined energy eigenstate. An interferometric measurement of the work distribution using an ancilla was proposed in [132, 133]. Finally, it has also been proposed to measure the environment, rather than the system, to keep track of the energy exchanges between the two [15]. This proposal has spurred further theoretical investigations [134, 135]; see also Publication X.

Let us consider the circuit of Fig. 4.1, which describes a minimal, all-electrical set-up for a calorimetric measurement of work [15]. The circuit consists of a gate-driven Cooper-pair box, which is also capacitively coupled to a resistor. The Cooper-pair box acts as the quantum system and the resistor as a broadband environment. Voltage fluctuations across the resistors are coupled to the potential of the island, so that photons can be exchanged between the Cooper-pair box and the resistor. In order to detect photon-exchange events, the temperature T_e of the electron gas in the resistor is constantly monitored. Absorption of a single photon of energy E_C causes T_e to rise by an amount $\Delta T_e = E_C/\mathcal{C}$, where $\mathcal{C}$ is the heat capacity of the electron gas. This temperature "spike" decays with a characteristic time constant $\tau = \mathcal{C}/G_{\rm th}$, where $G_{\rm th}$ is the thermal conductance between the resistor and its thermalization bath. A temperature trace such as the one shown in Fig. 4.1 thus makes it possible to determine the distribution of photon exchanges, as well as their energies (provided G is known from an independent measurement) [15]. Continuous photon exchanges between two resistors coupled by superconducting lines have

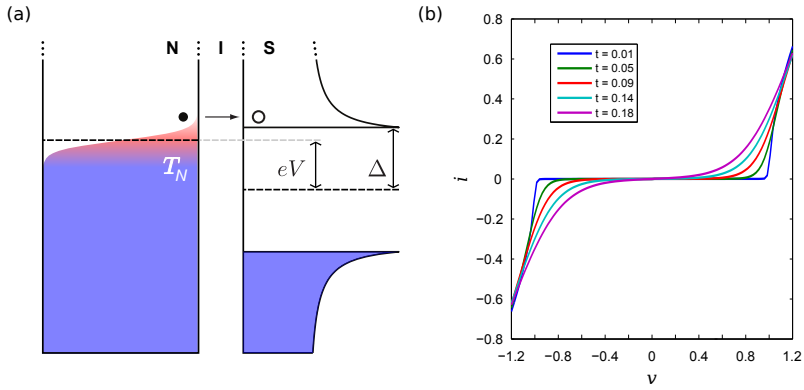

Figure 4.2. The NIS junction. (a) Energy-level diagram of a voltage-biased NIS junction. (b) Current-voltage characteristics of the NIS junction at different normal-metal temperatures. The relevant quantities have been normalized according to $v = eV/\Delta$, $i = \frac{eR_T}{\Delta} I$, and $t = k_B T/\Delta \approx 0.57 T/T_c$.

been measured using normal metal-insulator-superconductor junction as thermometers [136, 137]. However, in order to resolve single photons in real time, a fast and accurate thermometer is needed. The bandwidth should be much larger than $1/\tau$ and the sensitivity should exceed $\Delta T_e \sqrt{\tau}$. For a micrometer-sized Cu island of volume $\approx 1 \times 10^{-20}\,\mathrm{m}^3$ at $100\,\mathrm{mK}$, the expected temperature rise for a photon of energy $E_C/k_B = 1\,\mathrm{K}$ is about $1\,\mathrm{mK}$. The expected thermal relaxation time is of the order of $10\,\mu\mathrm{s}$, requiring a bandwidth in the MHz range and a sensitivity of a few $\mu\mathrm{K}/\sqrt{\mathrm{Hz}}$. Our first steps towards the realization of such a thermometer, reported in Publication XI, are the main focus of this Chapter.

4.2 The rf-NIS thermometer

The NIS junction

Tunnel junctions between a normal metal and a superconductor (NIS junctions) have been used for electron thermometry [138, 139] and refrigeration [140] since a long time; for a review, see Refs. [86, 87].

An energy-level diagram for the voltage-biased NIS junction is shown in Fig. 4.2. The density of states in the normal metal is constant around the Fermi energy, while that of the superconductor is given by the Bardeen-

Cooper-Schrieffer expression [141] [1]

$$N_S(E) = \left| \Re\mathrm{e}\left(E/\sqrt{E^2 - \Delta^2} \right) \right| \tag{4.2}$$

Electron states are populated according to the Fermi distributions $f_{N,S}(E) = \{1 + \exp[E/(k_B T_{N,S})]\}^{-1}$ at temperatures $T_{S,N}$, where the subscript N (S) stands for the normal metal (the superconductor). Fig. 4.2 already illustrates the basic principle of NIS thermometry: at temperatures $T_N \ll \Delta/k_B$ and bias voltages $V_b \lesssim \Delta/e$, the sharp density of states in the superconductor can be exploited to probe the (local) electron energy distribution in the normal metal. In the so-called quasiequilibrium regime [86], this distribution is in one-to-one correspondence with temperature. More generally, however, the NIS junction can be used to characterize out-of-equilibrium distributions; see, for instance, Ref. [144].

In describing the transport properties of the NIS junctions, we will limit ourselves to sequential electron tunneling, thus neglecting higher-order processes such as elastic cotunneling and Andreev reflection [145, 146]. While not relevant for the present work, such higher-order processes have been extensively studied elsewhere [147]. The current can be written as [86]

$$I_{\mathrm{NIS}} = \frac{1}{2eR_T} \int dE N_S(E) \left[f_N(E - eV_b) - f_N(E + eV_b) \right] , \tag{4.3}$$

where R_T is the tunneling resistance of the junction. Equation (4.3) highlights an important feature of the NIS junction as a thermometer: the current is insensitive to the occupation f_S in the superconductor, and hence to T_S. This insensitivity holds as long as the superconducting energy gap in (4.2) can be assumed to be constant, which is practically true up to $T/T_c \approx 0.4$, where T_c is the critical temperature of the superconductor.

The current-voltage characteristic of the NIS junction is shown in Fig. 4.2(b) for a few different temperatures. At low temperatures, the thermometer is only sensitive at voltages close to the gap, with the most sensitive points

[1] The finite-lifetime-broadened expression

$$N_S(E) = \left| \Re \frac{\mathrm{E}/\Delta + \mathrm{i}\gamma}{\sqrt{(E/\Delta + i\gamma)^2 - 1}} \right| \tag{4.1}$$

is often found in good agreement with the experiments, where $\gamma \ll 1$ is known as the Dynes parameter [142]. The broadening can have different origins, including defects in the junction as well as environment-assisted tunneling [143]. A finite Dynes parameter limits the operation range of the NIS thermometers to temperatures $T \gg \frac{\gamma\Delta}{k_B}$. Typical values obtained in our laboratory are $\gamma \approx 10 \times 10^{-4}$. By using additional on-chip filtering (ground plane), the record bound $\gamma < 1.6 \times 10^{-7}$ was obtained in Ref. [61].

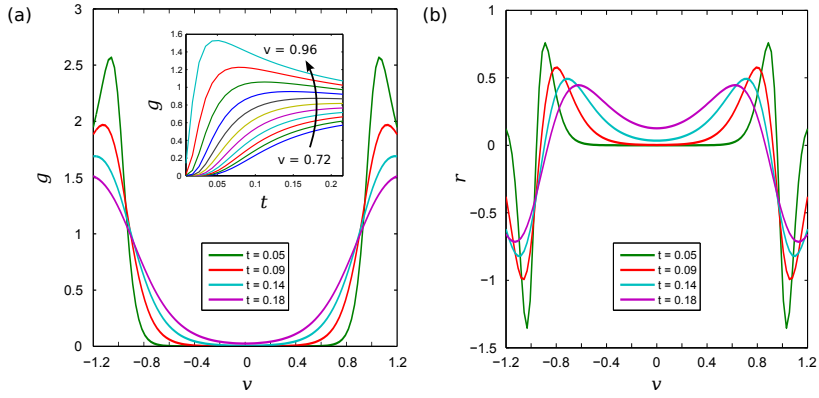

Figure 4.3. The NIS thermometer: differential readout. (a) Conductance-voltage characteristics of the NIS junction. The conductance is normalized as $g = R_T G$. Inset: conductance versus temperature for a set of voltages in the range of $0.72\Delta/e$ and $0.96\Delta/e$. (b) Responsivity $\mathcal{R} = \partial G/\partial T$ of conductance to temperature, normalized as $r = \frac{R_T \Delta}{k_B}\mathcal{R}$.

shifting towards zero bias as temperature is increased. In principle, temperature can be extracted from either a voltage-biased or a current-biased measurement. In the experiments, the current-biased configuration is typically preferred for a few practical reasons (for instance, in the SINIS configuration, the thermometer can be read out with a floating circuit). In any case, the temperature response is always monotonic and has the same sign at subgap voltages: a higher temperature corresponds to either a lower voltage (in the current bias mode), or a higher current (in the voltage-bias mode). A third possibility is to perform a differential readout, which probes the differential conductance $G_{\rm NIS} = \partial I_{\rm NIS}/\partial V_b$ at a fixed bias point. This possibility naturally arises in the radiofrequency measurement.

Upon differentiating (4.3), we obtain

$$G_{\rm NIS} = \frac{1}{R_T k_B T}\int dE N_S(E) f_N(E - eV_b)\left[1 - f_N(E - eV_b)\right] . \qquad (4.4)$$

Conductance-voltage characteristics are plotted in Fig. 4.3(a) for different temperatures. The differential conductance of the junction can far exceed its normal-state value $G_{\rm NIS} = 1/R_T$ at the onset of conduction, corresponding to the "knee" features of the I-Vs in Fig. 4.2(b). In contrast to the dc case, the conductance response is not, in general, monotonic. This can be seen from Fig. 4.3(a), Inset, where we plot $G_{\rm NIS}$ versus T_N for different values of V_b. At voltages close to the gap, some values of G are clearly associated to two different temperatures. An interesting figure for the optimization of the thermometer is the temperature responsivity of

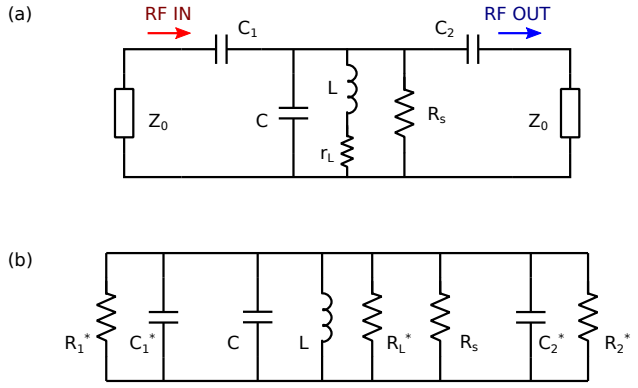

Figure 4.4. Resonator model (a) Lumped-element resonator with transmission readout. (b) Norton equivalent circuit used for estimating the resonant frequency and the quality factor.

the conductance, defined as $\mathcal{R}(V,T) = \frac{\partial G}{\partial T}$ and given by

$$\mathcal{R}(V_b,T) = -\frac{G_{\rm NIS}}{T} + \frac{1}{R_T k_B^2 T^3} \int dE N_S(E+eV_b) E f_N(E) \left[1 - f_N(E)\right] \left[1 - 2 f_N(E)\right] \ . \tag{4.5}$$

In Fig. 4.3(b), we plot $\mathcal{R}$ versus V_b at different temperatures. In the subgap region, the bias point that maximizes the responsivity moves towards zero bias as temperature is increased. Notice that the high responsivities obtained at voltages above the gap are of very limited usefulness, as they are accompanied by strong dissipation in both the normal-metal and the superconducting electrode.

The resonator

In order to enable a fast readout, we embed the NIS junction into a lumped-element microwave resonator [148]. Similar techniques are routinely used for the fast readout of high-impedance nanodevices, including single-electron transistors [149] and quantum point contacts [150, 151].

A lumped-element model for the resonator is illustrated in Fig. 4.4(a). The resonator consists of an inductor L of internal resistance r_L and a capacitor C. It is connected to input and output ports via the capacitors C_1 and C_2, respectively. The NIS junction is embedded in the resonator, introducing a parallel dissipative element of impedance R_s. At low input powers, R_s is given by the differential impedance of the junction at the voltage bias point set by the dc circuit (not shown). The transmission-line impedance of the readout circuit is $Z_0 = 50\,\Omega$.

In order to compute the resonator properties close to its resonant frequency ω_0, it is useful to turn the circuit of Fig. 4.4(a) into the equivalent circuit of Fig. 4.4(b). [2] We will also assume that $R_s \gg Z_0$ and that $L/(C + C_1 + C_2) \gg Z_0$. In the circuit of Fig. 4.4(b), internal losses are described by the parallel resistance $r_L^* = \frac{L^2\omega_0^2}{r_L}$. Losses due to the coupling to the input and output ports are accounted for by the resistances

$$R_i^* = \frac{1 + C_i^2 Z_0^2 \omega_0^2}{C_i^2 Z_0 \omega_0^2} \approx \frac{1}{C_i^2 Z_0 \omega_0^2} , \tag{4.6}$$

while the coupling capacitors contribute to the total capacitance $C_\Sigma = C + C_1^* + C_2^*$ as

$$C_i^* = \frac{C_i}{1 + C_i^2 Z_0^2 \omega_0^2} \approx C_i . \tag{4.7}$$

The resonant frequency of the circuit is given by

$$\omega_0 = \frac{1}{\sqrt{LC_\Sigma}} . \tag{4.8}$$

If $R_s \ll r_L^*$, then the internal quality factor is dominated by the NIS junction and reads

$$Q_{\text{int}} = \frac{R_s}{\omega_0 L} . \tag{4.9}$$

The external quality factor is determined by

$$R_{\text{ext}} = \frac{R_1^* R_2^*}{R_1^* + R_2^*} = \frac{1}{(C_1^2 + C_2^2) Z_0 \omega^2} \tag{4.10}$$

as

$$Q_{\text{ext}} = \frac{R_{\text{ext}}}{\omega_0 L} . \tag{4.11}$$

The scattering matrix can be calculated from the circuit in Fig. 4.4 with standard methods [154]. In Fig. 4.5(a), we plot the transmittance $|s_{21}|^2$ versus frequency for different NIS impedance R_s, namely, in the overcoupled ($R_s \gg R_{\text{ext}}$), critically coupled ($R_s = R_{\text{ext}}$) and slightly undercoupled ($R_s = \frac{1}{2} R_{\text{ext}}$) regimes. As the NIS junction acts as a dissipative element, it modifies the transmission at resonance as well as the quality factor, but it does not shift the resonant frequency. After a few simplifications, the transmittance at resonance can be written as

$$s_{21} = -\frac{2C_1 C_2 R_s Z_0}{LC_\Sigma + \left(C_1^2 + C_2^2\right) R_s Z_0} = -\frac{\alpha R_s / R_{\text{ext}}}{1 + R_s / R_{\text{ext}}} , \tag{4.12}$$

where $\alpha = \frac{2C_1 C_2}{C_1^2 + C_2^2}$ is related to the symmetry of the coupling capacitors. Of particular interest is the responsivity of the power transmittance $|s_{21}|^2$ to changes in R_s

$$\frac{\partial}{\partial R_s} |s_{21}|^2 = \frac{2\alpha^2 R_{\text{ext}} R_s}{(R + R_{\text{ext}})^3} \tag{4.13}$$

[2] A similar calculation was carried out in Ref. [152] for a different type of resonator. The resonator of Fig. 4.4(a) was considered in Ref. [153].

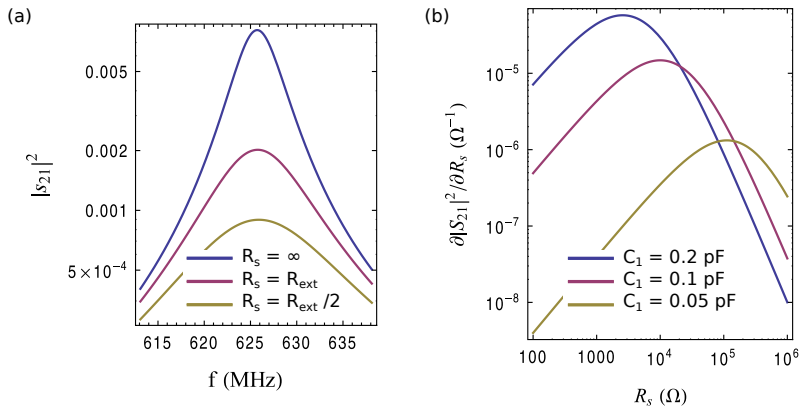

Figure 4.5. Calculated resonator response. (a) Transmittance $|s_{21}|^2$ versus frequency for different values of the junction impedance R_s. (b) Resonator responsivity at resonance, versus R_s, for different values of the coupling capacitors C_1 and C_2, with $C_1 = C_2$.

The responsivity is maximum when $R_s = \frac{1}{2}R_{\rm ext}$, where it takes the value $\frac{8\alpha^2}{27R_{\rm ext}}$. In Fig. 4.5(b), we plot the responsivity versus R for different values of the coupling capacitors, with $\alpha = 1$. While the optimal responsivity point can be tuned by changing the capacitors, the general trend is that the responsivity decreases as the R_s turns away from the line impedance Z_0.

4.3 Thermal model of the NIS calorimeter

In this Section, we introduce a thermal model for the experiment of Publication XI. Let us consider the circuit of Fig. 4.6(a), consisting of a normal-metal (Cu) island of line resistance r_I connected to superconducting (Al) leads by two clean contacts (left, right) and one tunnel barrier (top). Voltage biases V_b and V_H are applied to the top and left lead, respectively, while the right lead is grounded. This circuit realizes a microcalorimeter, comprising a thermometer (the NIS junction) and a Joule heater (the left NS contact, together with the island resistance).

We will assume that the so-called quasiequilibrium regime holds for the electron gas in the island [86]. This regime requires that the electron-electron relaxation time τ_{e-e} be much faster than the quasiparticle injection rate and implies that the electron gas is described by a Fermi-Dirac distribution with a well-defined temperature T_e. The latter, in general, can be different from the temperature T_b of the surrounding environment.

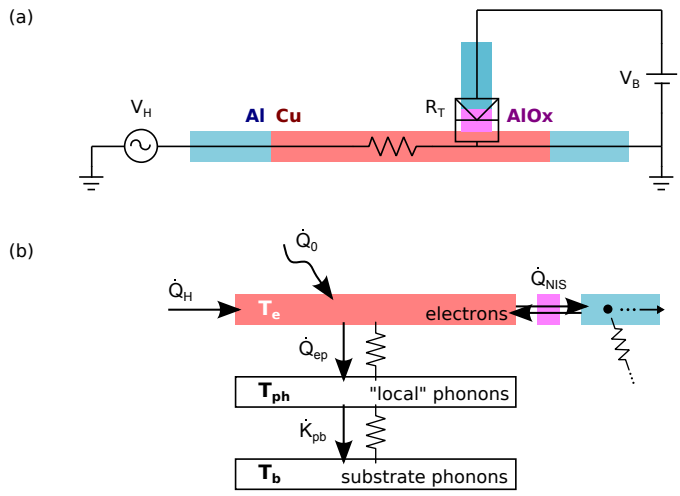

Figure 4.6. Thermal model of the NIS calorimeter. (a) Electrical circuit. (b) Corresponding heat flows; see the text.

Electron-electron relaxation is much faster in metals than in semiconductors [compare Chapter 3], due to the higher electron density. As a result, the quasiequilibrium regime is the most typical setting down to $100\,\mathrm{mK}$ and in the presence of low to moderate injection rates. Deviations from quasiequilibrium were reported in [155], where low-resistance ($100\,\Omega$ – $2\,\mathrm{k}\Omega$) NIS junctions were used as electronic coolers.

A sketch of the thermal model is shown in Fig. 4.6(b). The electron gas of the island is thermally connected to the local phonon bath at temperature T_{ph}. The local phonon bath, in turn, is thermally connected to the substrate phonons, which are assumed to be thermalized at the bath temperature T_b. The time-dependent electronic temperature T_e is governed by the heat equation:

$$\mathcal{C}(T_e)\frac{dT_e}{dt} = \dot{Q}_H(V_H) + \dot{Q}_{\mathrm{e-ph}}(T_e, T_{\mathrm{ph}}) + \dot{Q}_{\mathrm{NIS}}(V_b, T_e) + \dot{Q}_0\ , \tag{4.14}$$

where $\mathcal{C}(T_e)$ is the heat capacity of the electron gas and a brief description of each contribution on the right-hand side of (4.14) follows. The heating voltage V_H causes the Joule power

$$\dot{Q}_H(V_H) = \frac{V_H^2}{r_I} \tag{4.15}$$

to be dissipated in the island, where r_I is the end-to-end resistance of the island. The heat flow from electrons into phonons is typically given by the standard expression [156, 157]

$$\dot{Q}_{\mathrm{e-ph}}(T_e, T_{\mathrm{ph}}) = \Sigma\mathcal{V}(T_e^5 - T_{\mathrm{ph}}^5)\ , \tag{4.16}$$

where Σ is a material-dependent constant [3]. Electron tunneling through the NIS junction contributes a heat flow

$$\dot{Q}_{\rm NIS} = -\frac{1}{e^2 R_T}\int dE(E-eV_b)N_S(E)f_N(E-eV_b)\ , \qquad (4.17)$$

where R_T is the tunneling resistance of the junction and we have assumed that the temperature of the superconducting lead satisfies $T_S < 0.3\Delta/k_B$. Equation predicts cooling for $V_b \lesssim \Delta/e$ and heating when $V_b > \Delta/e$. In principle, then, the NIS thermometer does not cause significant overheating to the island – it tends to cool it, instead. However, we must remember that the total amount of power $I_{\rm NIS}V_b$ is dissipated at the junction, implying a heat flow $I_{\rm NIS}V_b - \dot{Q}_{\rm NIS}$ into the superconducting lead. This heat flow is carried by hot quasiparticles that tend to accumulate close to the junction. Excess quasiparticles can either recombine or diffuse away from the junction, but both these processes are very slow at low temperatures. As a result, the local effective temperature of the superconducting lead can rise as much as needed for these two equilibration channels to become effective. This degrades heat transport figures in NIS coolers as well as thermometers. However, the situation is much more severe for coolers as they are operated at much higher powers. Engineering the lead geometry and putting quasiparticle traps close to the junction have lead to a significantly improved performance [160, 161]. As for thermometers, increasing the tunneling resistance of the junction is sufficient for most applications. By the way, a poor performance of the NIS junction as a cooler may even be desirable for thermometry, as it makes the thermometer less invasive. Finally, a constant term $\dot{Q}_0 > 0$ is added to (4.14) in order to account for a spurious heating power which can arise, e.g., due to imperfect filtering of noise and blackbody radiation from higher-temperature stages.

It is worth spending a word on those heat flows which are not considered in (4.14). Thermal conductivity through the clean NS contacts can be neglected in the conditions of Publication XI, as (a) Andreev reflection blocks the heat flow within the gap, (b) the residual heat conduction due to quasiparticle excitations is effectively frozen out below $200\,\mathrm{mK}$, and (c) our superconducting lines are much longer than the coherence length, so that the inverse proximity effect is suppressed [162]. Finally, photonic heat conductance [136] is also negligible for our sample at these temperatures, due to the mismatch of the relevant impedances [137].

[3] For Cu, $\Sigma = 2\times10^9\,\mathrm{Wm^{-3}K^{-5}}$ [157]. Other power laws in T_e have also been reported [158, 159].

4.4 Experimental realization

In Publication XI, we demonstrate rf-NIS thermometry on a micrometer-sized Cu island below 100 mK. While based on an established technique, our work stands out from previous implementations [148, 163, 164] in many respects.

First of all, the volume of the island ($\mathcal{V} = 0.05\,\mu\mathrm{m}^3$) is smaller and the measured electronic temperatures are considerably lower than previously reported. As a result, the electron gas in the island has smaller heat capacity ($\mathcal{C} = \gamma\mathcal{V}T_e$) and much smaller heat conductance to its thermal bath ($G_{\mathrm{th}} = 5\Sigma\mathcal{V}T_e^4$, see the following). Pushing down these two numbers, while ensuring a reliable temperature readout, can turn the island into a fast and sensitive calorimeter of great practical value, with applications such as single-photon detection. With the current, admittedly not-optimized set-up, we estimate we can detect temperature spikes of 10-mK height in a single-shot measurement. This figure is about one order of magnitude higher than the temperature rise expected for a single-photon absorption event.

Further points of novelty are related to the biasing point and the estimate of temperature. In Refs. [148, 163], the devices were operated at zero bias. As the electronic temperature is lowered, however, the sensitivity of the NIS thermometer is (exponentially) suppressed at zero bias [see Section 4.2]. In Publication XI, we perform rf-NIS thermometry at different bias points. At low input powers, the rf readout allows us to faithfully sample the local differential conductance of the NIS junction. In turn, this makes it possible to directly convert the transmitted power into absolute temperature, using a minimal set of assumptions. Our temperature estimates are found in quantitative agreement with a theoretical model which takes the relevant heat flows into account. This confirms the validity of our technique.

Finally, we carry out a systematic characterization of thermal relaxation times at low temperatures. To our knowledge, these are the first such measurements in this temperature range. The measured relaxation times are compatible with previous measurements performed at higher temperatures [158, 163, 164], if one assumes the usual power law for the electron-phonon interaction. However, they are significantly longer than one would expect from the nominal heat capacity and heat conductance of the island. This suggests that the heat capacity of the Cu island may be

larger than the nominal value, due, for instance, to the presence of magnetic impurities in the Cu film [165, 166]. In fact, the thermal conductance of the island can be measured at steady state with dc techniques and is typically found in agreement with theory, possibly with a larger prefactor. On the other hand, measuring the heat capacity requires a dynamic measurement on a time scale faster than the thermal relaxation time. Such a measurement should be feasible with the present technique and is currently underway. We should also mention that the Kapitza contact resistance between different phonon baths, considered in a recent experimental work [167], as well as phonon transport in general, may also affect the relaxation times. Altogether, these considerations only highlight the key role time-resolved thermometry can play in deepening our understanding of thermal transport at the nanoscale.

Continuous-wave characterization

The sample measured in Publication XI consists of a 25 nm thick, 100 nm wide and 20 µm long Cu island connected to Al leads via two clean normal metal-superconductor contacts and a NIS junction with normal-state resistance $R_T = 22\,\mathrm{k}\Omega$. A schematic of our measurement set-up is shown in Fig. 4.7(a) and a close-up, false-color micrograph of the device is shown in Fig. 4.7(b). The NIS probe is embedded in a lumped-element LC resonator with resonant frequency $f_0 = 625\,\mathrm{MHz}$. A bias tee allows a dc voltage bias V_b to be applied to the NIS junction without interfering with the resonator readout. Of the two NS contacts, one is grounded at the sample stage, while the other is used to feed a heating current to the island. The total resistance of the island is $r_I = 360\,\Omega$, of which less than 10% lies between the NIS probe and the grounding NS contact.

We probe the resonator, coupled to input and output ports via the capacitors C_{C1} and C_{C2}, by measuring the transmittance $|s_{21}|^2 = P_{\mathrm{out}}/P_{\mathrm{in}}$. Figure 1(c) shows how the resonance peak responds to changes in V_b. The transmittance at resonance is well approximated by (4.12), with $R_{\mathrm{ext}} = 45.5\,\mathrm{k}\Omega$. For each curve in Fig. 4.7(c), we note the corresponding differential impedance R_s, emphasizing the high sensitivity of the readout at impedances of the order of R_{ext} (critical coupling, see Section 4.2). At critical coupling, the bandwidth is $10\,\mathrm{MHz}$ and the loaded quality factor is 62.5. In the following, we always probe the resonator at the resonant frequency f_0.

In Fig. 4.7(d), we plot $|s_{21}|^2$ as a function of V_b for a set of bath tem-

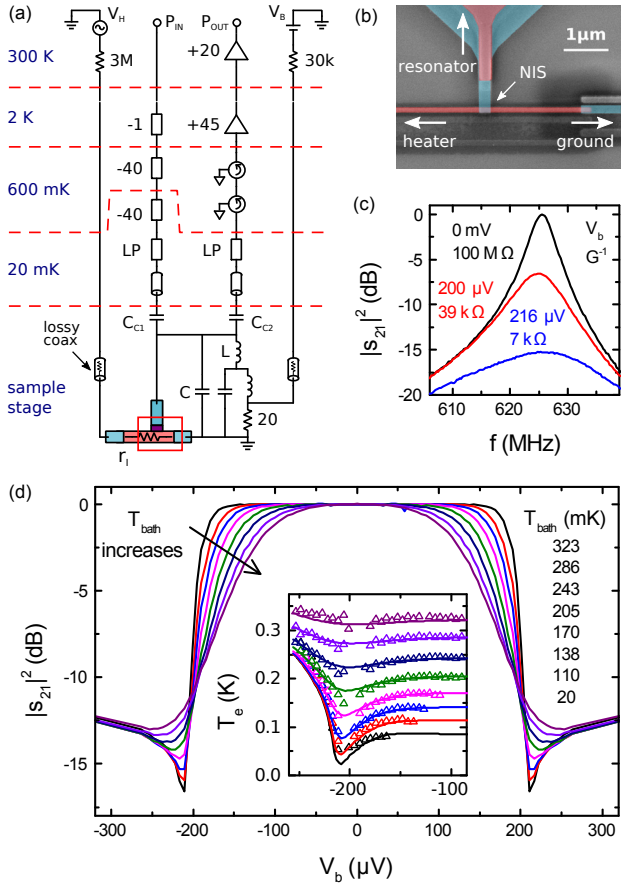

Figure 4.7. The rf-NIS thermometer. (a) Schematic of the measurement circuit. (b) False-color micrograph of a representative device (red: Cu, blue: Al), closing up on the NIS junction used as a thermometer. (c) Small-signal transmittance $|s_{21}|^2$ versus frequency for three selected values of the voltage bias V_b; the corresponding differential impedance G^{-1} of the NIS junction varies between $7\,\mathrm{k}\Omega$ and $100\,\mathrm{M}\Omega$. (d) Transmittance-voltage characteristics: $|s_{21}|^2$ versus V_b for a set of bath temperatures T_{bath} in the range of 20 to 323 mK. Inset: Electronic temperature T_e vs V_b for different values of T_{bath}. The experimental points (triangles) are obtained from the data of the main panel using Eqs. (4.12) and (4.4). The predictions of a thermal model taking into account electron-phonon and tunneling heat conductance [see Section 4.3] are shown for comparison (full lines).

peratures $T_{\rm bath}$ in the range of 20 to 325 mK. For each temperature, the transmittance at zero bias is taken as the $0\,{\rm dB}$ reference. The curves of Fig. 4.7 contain the same information as the conventional current-voltage characteristics of a NIS junction. In particular, they make it possible to infer the bias-dependent electronic temperature T_e in the Cu island. To extract T_e from $|s_{21}|^2$, we first convert $|s_{21}|^2$ into G using (4.12) and then G into T_e by numerically inverting (4.4). In Fig. 4.7(d), Inset, we plot the obtained T_e versus V_b, as extracted from the traces in the main panel (triangles). We have excluded points around $V_b \approx 0.98\Delta/e$, where the first-order responsivity (4.5) vanishes. At base temperature $T_{\rm bath} = 20\,{\rm mK}$, we find that $T_e \approx 85\,{\rm mK}$. This saturated T_e corresponds to a spurious injected power $\dot{Q}_0 \approx 400\,{\rm aW}$, which we ascribe to imperfect shielding of blackbody radiation as well as low-frequency noise in the dc lines and in the ground potential. The dependence of T_e on V_b, most pronounced for the lowest-temperature traces, is due to heat transport across the NIS junction, as described by (4.3). Conversely, at high temperatures, T_e closely follows $T_{\rm bath}$, as the electron-phonon heat conductance provides a strong thermal anchoring to the electrons in the Cu island. Our data are quantitatively accounted for by the thermal model of Section 4.3. The calculated T_e (full lines) agrees well with the measured ones, except in the vicinity of the optimal cooling point, where only a modest cooling is observed if compared to the theoretical prediction. This behavior can be ascribed to local overheating of the superconductor, as discussed in Section 4.3. Altogether, these results establish the validity of our rf-NIS thermometry technique.

Time-resolved measurements: thermal relaxation times

We demonstrate the real-time capability of our thermometer by measuring the thermal relaxation of the electron gas in the Cu island in response to a Joule heating pulse. The output signal is demodulated at the carrier frequency and recorded with a fast digitizer. The heating waveform is an amplitude-modulated sinusoid of frequency $f_H = 1\,{\rm MHz}$ and peak-to-peak amplitude $V_H^{\rm pp}$, see Fig. 4.8(a), which is fed to a large bias resistor R_H and then to the heating line. As f_H is much faster than the measured thermal relaxation rates (see the following), the island reacts to the time-averaged heating power $\dot{Q}_H = \frac{1}{2}(V_H^{\rm pp})^2 r_I / R_H^2$ when the heating is on. The time-domain response of the thermometer to the heating pulse is shown in Fig. 4.8(b) at base temperature, for a fixed V_b and different values of $V_H^{\rm pp}$. The left axis indicates the instantaneous power recorded by the digitizer.

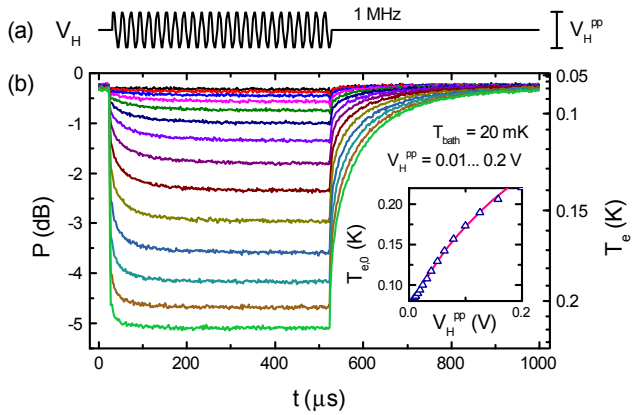

Figure 4.8. Time-resolved thermometry. (a) Amplitude-modulated sinusoid used to drive the heating pulse (the frequency is not to scale) and (b) real-time response of the thermometer, obtained by recording the transmitted power P versus time for different values of the heating-pulse amplitude $V_H^{\rm pp}$. The conversion from P into absolute electronic temperature T_e is displayed on the right axis. Inset: T_e at the end of the heating pulse ($t = 520\,\mu$s) versus $V_H^{\rm pp}$ (triangles). The prediction of the thermal model is shown for comparison (full line). All the traces are taken at base temperature and the voltage bias is $V_b = 0.17\,$mV.

This power is converted into temperature using a similar procedure as in Fig. 4.7(d), Inset, and the corresponding scale is noted on the right axis. The temperature reached by the island at the end of the heating pulse is plotted in Fig. 4.8(b), Inset as a function of $V_H^{\rm pp}$ (triangles), in good agreement with the prediction of the thermal model (full line). From Fig. 4.8, we see that the thermal response of the island is not instantaneous; instead, a finite-time relaxation is observed after the rising and falling edge of the pulse.

With constant heat input and when T_e is not far from its steady-state value $T_{e,0}$, the heat equation (4.14) can be studied in the linear-response limit. Written in terms of the temperature deviation $\delta T = T_e - T_{e,0}$, the linearized (4.14) reads

$$\mathcal{C}\frac{d\delta T}{dt} = -G_{\rm th}\delta T\ , \tag{4.18}$$

where $\mathcal{C}$ is the electronic heat capacity of the island, $G_{\rm th}$ is the total thermal conductance to its environment, and both $\mathcal{C}$ and $G_{\rm th}$ are evaluated at $T_{e,0}$. Equation (4.18) tells that T_e relaxes to $T_{e,0}$ exponentially with the relaxation time $\tau_0 = \mathcal{C}/G_{\rm th}$. Even after a large change in the heating power [beyond the linear-response regime described by (4.18)], the final approach to the new $T_{e,0}$ obeys this exponential law.

In Fig. 4.9(a-d), we present relaxation tails obtained from measurements

similar to those of Fig. 4.8. The tails are obtained from the raw data by subtracting the steady-state-temperature baseline from each trace. They have been normalized, horizontally offset for clarity, and plotted in a semilogarithmic scale in order to highlight the exponential decay. The full lines are fits of an exponential function to the tails.

The tails in panels (a,b) refer to relaxation after the rising (a) and falling edge (b) of heating pulses of different amplitude $V_H^{\rm pp}$. As $V_H^{\rm pp}$ is increased, relaxation after the rising edge gets faster as $T_{e,0}$ increases; on the other hand, no change is observed in the tails after the falling edge, as $T_{e,0}$ stays the same. In panel (c), we vary the bath temperature $T_{\rm bath}$ and see that the relaxation gets faster as $T_{\rm bath}$ is increased. In panel (d), we vary the bias voltage V_b. The observed time constant stays approximately the same, regardless of the fact that G changes by over two orders of magnitude across the given V_b range. Finally, in panels (e,f), we plot the values of τ as obtained from the fits. In panel (e), we show the dependence on V_b for two different values of $T_{\rm bath}$. The measured τ at base temperature is of the order of $100\,\mu$s and it increases by some 20% as V_b approaches Δ/e. This increase may well be due to a decrease in $G_{\rm th,ep}$ due to cooling of the island [compare Fig. 4.7(d), Inset]. In panel (f), we show the temperature dependence of τ, obtained in two different ways: we measured tails after the falling edge while varying $T_{\rm bath}$ (circles) and tails after the rising edge while varying $V_H^{\rm pp}$ (triangles). In the latter case, τ is plotted against $T_{e,0}$ at the end of the pulse, estimated as in Fig. 4.8(b). The agreement between the two series is remarkable. The saturation of τ at low $T_{\rm bath}$ is also consistent with the saturated T_e observed in Fig. 4.7(d), Inset. At higher temperatures, τ is predicted to scale as $T_{e,0}^{-3}$ provided $G_{\rm th} \approx G_{\rm th,ep}$ and both $\mathcal{C}$ and $G_{\rm th,ep}$ follow the theory predictions. The data presented here are not conclusive in this respect, due to the saturation of $T_{e,0}$ at low $T_{\rm bath}$ and to the narrow temperature range considered. Due to a transient that we observe after terminating the heat pulse, we refrain from presenting data points with $\tau \lesssim 20\,\mu$s. An improved set-up to avoid this transient is being made available in our laboratory.

Sensitivity and noise

We have performed systematic noise measurements of our thermometer in the frequency range of 1 Hz to 1 MHz, at different voltage biases, bath temperatures and input powers, and using different noise-equivalent bandwidths when digitizing the signal.

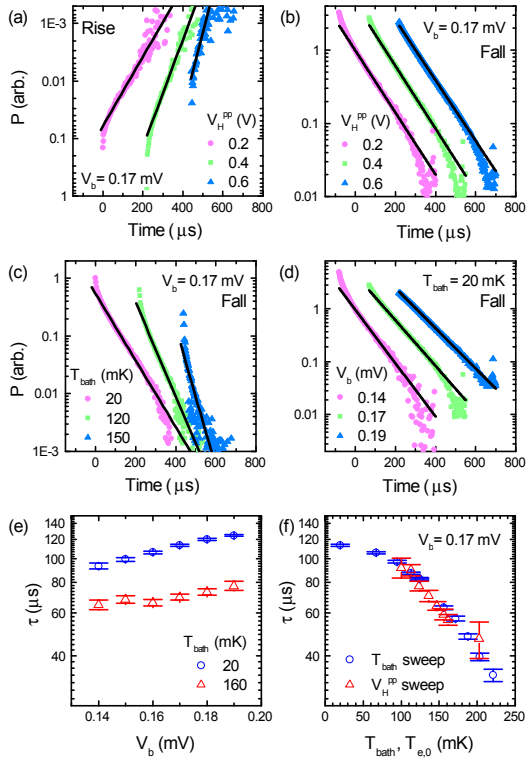

Figure 4.9. Time-resolved thermal relaxation. (a–d) Thermal relaxation traces (circles, squares, triangles). The traces are shifted by their baseline after relaxation, scaled and plotted on a logarithmic scale. They are also horizontally offset by $150\,\mu s$ for clarity. The full lines are exponential fits of the form $A\exp(-t/\tau)+B$ to the data. The data in panels (a,b) correspond to the rising (a) and falling edges (b) of selected traces in Fig. 4.8. Panels (c,d) present similar traces obtained for different values of the voltage bias V_b (c), and at different bath temperatures $T_{\rm bath}$ (d). (e) Thermal relaxation time τ versus V_b for two different values of $T_{\rm bath}$. (f) Temperature dependence of τ, obtained from traces as in panel (c) (circles, the x axis is $T_{\rm bath}$) and as in panel (a) (triangles, the x axis is the temperature $T_{e,0}$ at the end of the pulse). The error bars in (e,f) are obtained from the fits.

Our data indicate a noise temperature (NT) of about 8 K for our amplification chain, largely set by our HEMT amplifier, whose nominal NT, measured at 20 K and 550 MHz, is 6.5 K. The corner frequency for the $1/f$ noise is of the order of a few Hz.

Our experiments were performed at low input power, corresponding to a voltage modulation across the NIS junction of amplitude $\lesssim 1\,\mu\mathrm{V}$. This allows a faithful sampling of the transmittance-voltage characteristics reported in Fig. 4.7; furthermore, the responsivity of the thermometer approaches its theoretical value $\mathcal{R} = P_{\mathrm{in}}(\partial|s_{21}|^2/\partial G)(\partial G/\partial T_e)$. Under these conditions, we obtain a noise-equivalent temperature (NET) of $100\,\mu\mathrm{K}/\sqrt{\mathrm{Hz}}$ at 80 mK and $220\,\mu\mathrm{K}/\sqrt{\mathrm{Hz}}$ at 150 mK. This figure, together with the measured τ, makes it possible to detect a single energy-absorption event producing a 10 mK temperature spike. This figure can be improved by one to two orders of magnitude by proper optimization. In particular, the device can be operated at higher input powers, exploiting the fact that the NIS junction does not introduce dissipation at voltages below Δ/e; in fact, it can behave as a cooler, as discussed in Section 4.3 and confirmed by our data as well as by many previous experiments. The responsivity of the resonator can be improved by reducing the stray capacitance. Finally, the NT of the readout chain can be lowered by using an amplifier with a lower NT as the first stage; a Josephson parametric amplifier [168] is one such choice.

5. Dissipation in driven quantum systems

In this chapter we present three studies on the dynamics of periodically driven quantum systems in the presence of dissipation. These studies are presented in a separate chapter as they are based on a common theoretical formalism. However, their motivation is well grounded in the experiments of Chapters 2 and 4. In the introductory Section 5.1 we present the Born-Markov master equation for a periodically driven quantum system. In Section 5.2 we discuss a specific limit of this equation, considered in Publication VII, where the dynamic steady state is strongly influenced by the presence of the environment. This limit can be encountered when operating a Cooper-pair pump in the fully nonadiabatic limit [see also Section 2.5]. In Section 5.3 we show that vacuum fluctuations of a broadband environment (Lamb shift) can have an enhanced influence in a driven system as compared to the static case (Publication IX). Cooper-pair pumps, as well as Cooper-pair boxes, are candidate systems for observing this effect. Finally, in Section 5.4 we study the statistic of heat exchanges between a driven system and its environment (Publication X). The predictions of our model could be tested using a calorimetric readout of the type discussed in Chapter 4.

5.1 Floquet-Born-Markov master equation for periodically driven quantum systems

Quantum master equation in the Born-Markov approximation

We consider a driven quantum system, described by the time-dependent Hamiltonian $H(t)$. Its coupling to the environment is described by the total Hamiltonian

$$H_T(t) = H(t) + H_B + V \tag{5.1}$$

where H_B is the environment Hamiltonian and $V = S \otimes B$ is a bilinear coupling operator, S and B being operators acting in the Hilbert spaces of the system and the environment, respectively. It is useful to introduce the interaction picture with respect to $H_0(t) = H(t) + H_R$. Then a generic operator O is transformed according to $O \to \tilde{O} = U_0^\dagger(t;0) O U_0(t;0)$, where

$$U_0(t;0) = \mathrm{Texp}\left(-\frac{i}{\hbar}\int_0^t H_0(t')dt'\right) . \tag{5.2}$$

The evolution of the total density matrix ρ_T in the interaction picture is given by the Liouville equation

$$i\hbar\frac{d}{dt}\tilde{\rho}_T(t) = \left[\tilde{V}(t), \tilde{\rho}_T(t)\right] . \tag{5.3}$$

Starting from (5.3), the derivation of a master equation for the reduced system density matrix $\rho = \mathrm{Tr}_B[\rho_T]$ follows standard steps [169]. Under the hypotheses of (i) weak coupling, (ii) factorized system-environment initial condition, and (iii) fast autocorrelation time of the environment as compared to the relaxation time of the system, it is justified to use the Born-Markov approximation. We can write the result as:

$$\begin{aligned}\frac{\partial}{\partial t}\tilde{\rho}(t) = -\int_0^\infty d\tau \Big[& g(\tau)\tilde{S}(t)\tilde{S}(t-\tau)\tilde{\rho}(t) - g(\tau)\tilde{S}(t-\tau)\tilde{\rho}(t)\tilde{S}(t) \\ & - g(-\tau)\tilde{S}(t)\tilde{\rho}(t)\tilde{S}(t-\tau) + g(-\tau)\tilde{\rho}(t)\tilde{S}(t-\tau)\tilde{S}(t)\Big] ,\end{aligned} \tag{5.4}$$

where we have introduced the environment correlation function

$$g(\tau) = \mathop{\mathrm{Tr}}_B\left[\tilde{B}(t')\tilde{\rho}_B\tilde{B}(t'')\right] . \tag{5.5}$$

Equation (5.4) is the master equation in the Born-Markov approximation, written in the most general form for a time-dependent system Hamiltonian and a stationary environment. In the following, we will restrict ourselves to time-periodic Hamiltonians and make further simplifications. But let us first take a moment to discuss the correlation function of the environment.

Bosonic bath and correlation functions

A typical assumption [170] is that the environment is composed of free bosons, $H_B = \sum_\nu \hbar\omega_\nu \left(\frac{1}{2} + b_\nu^\dagger b_\nu\right)$ and the coupling operator is the sum of displacement operators $B = \sum_\nu \lambda_\nu (b_\nu + b_\nu^\dagger)$, where b_ν and $b_\nu^\dagger$ are creation and annihilation operators of a boson of energy $\hbar\omega_\nu$, λ_ν is the strength of the coupling and the sum runs over all the environmental modes. After

introducing the spectral density

$$J(\omega) = \sum_{\nu} \frac{\lambda_\nu^2}{2} \delta(\omega - \omega_\nu) \,, \tag{5.6}$$

the correlation function of the environment can be written as

$$\begin{aligned} g(\tau) &= \int_0^\infty d\omega J(\omega) \left[e^{i\omega\tau} f_B(\omega) + e^{-i\omega\tau} \left(f_B(\omega) + 1 \right) \right] \\ &= \int_0^\infty d\omega J(\omega) \left[\cos(\omega\tau) \coth(\beta\omega/2) - i \sin(\omega\tau) \right] \end{aligned} \tag{5.7}$$

where $f_B(\omega) = [\exp(\beta\omega) - 1]^{-1}$ is the Bose distribution function and $\beta = (k_B T)^{-1}$ the inverse temperature. Typical spectral densities have the form

$$J(\omega) = \eta^2 \frac{\omega^s}{\omega_c^{s-1}} \cdot \frac{\omega_c^2}{\omega^2 + \omega_c^2} \tag{5.8}$$

where $\eta^2 \ll 1$ is a dimensionless coupling strength, s is a characteristic exponent and we have introduced a Lorentzian cutoff with frequency ω_c. Environments with $s = 1$, $s < 1$, and $s > 1$ are referred to as ohmic, subohmic and superohmic, respectively, due to the fact that the spectral density of voltage fluctuations across a resistor is described by (5.8) with $s = 1$.

The environment correlation function g enters the master equation (5.4) in an integral form. After a spectral decomposition of the noise operator S, one is left to consider integrals of the form:

$$\mathcal{I}_\pm(z) = \int_0^\infty d\tau g(\pm\tau) e^{-iz\tau} \tag{5.9}$$

Remembering the identity $\int_0^\infty e^{i\omega t} dt = \pi\delta(\omega) + \mathcal{P}\left(\frac{i}{\omega}\right)$, where $\mathcal{P}$ denotes the Cauchy principal value, we can write

$$\mathcal{I}_\pm(z) = \pi s(\pm z) + i\mathcal{G}_\pm(z) \,, \tag{5.10}$$

where

$$s(z) = \theta(z) J(z) f_B(z) + \theta(-z) J(-z) \left[f_B(-z) + 1 \right] \,, \tag{5.11}$$

$$\mathcal{G}_\pm(z) = -\mathcal{P} \int_0^\infty d\omega J(\omega) \left[\frac{f_B(\omega)}{z \mp \omega} + \frac{f_B(\omega) + 1}{z \pm \omega} \right] \,. \tag{5.12}$$

The imaginary term in (5.10) is responsible for a renormalization of the system energies, due to the presence of the environment (Lamb shift). [1] When considering undriven and weakly systems, it is typically neglected. However, its influence in strongly driven system can be considerable, as we show in Publication IX.

[1] Notice the property $\mathcal{G}_\pm(-z) = -\mathcal{G}_\mp(z)$.

Floquet-Born-Markov master equation

In the following, we consider a periodically driven system, so that $H_S(t+\tau) = H_S(t)$, where τ is the drive period and $\Omega = 2\pi/\tau$ the corresponding angular frequency. The periodicity of the drive allows for a formal simplification of (5.4), using Floquet states [65].

According to Floquet theorem, the Schrödinger equation admits solutions (Floquet states) of the form $|\Psi_\alpha(t)\rangle = e^{-i\epsilon_\alpha t/\hbar}|\varphi_\alpha(t)\rangle$, where the Floquet mode $|\varphi_\alpha(t)\rangle$ satisfies $|\varphi_\alpha(t+\tau)\rangle = |\varphi_\alpha(t)\rangle$ and ϵ_α is its corresponding quasienergy. Quasienergies and their associated modes are defined up to the translation $\epsilon_\alpha \to \epsilon_\alpha + \hbar\Omega$, where $\Omega = 2\pi/\tau$. As such, all quasienergies can be mapped into the first Brillouin zone $[-\frac{1}{2}\hbar\Omega, \frac{1}{2}\hbar\Omega]$.

Using Floquet states, the evolution operator $U_0(t;0)$ in (5.2) can be written as

$$U_0(t;0) = \sum_\alpha |\Psi_\alpha(t)\rangle\langle\Psi_\alpha(0)| \otimes e^{-iH_B t} \tag{5.13}$$

and the coupling operators $\tilde{S}$ as

$$\tilde{S}(t) = \sum_{\alpha,\beta,k} S_{\alpha\beta,k} e^{i\Delta_{\alpha\beta,k}t} \, |\Psi_\alpha(0)\rangle\langle\Psi_\beta(0)| \tag{5.14}$$

with

$$S_{\alpha\beta,k} = \frac{1}{T}\int_0^T dt \, \langle\phi_\alpha|S|\phi_\beta\rangle \, e^{-ik\Omega t} \tag{5.15}$$

$$\Delta_{\alpha\beta,k} = \epsilon_\alpha - \epsilon_\beta + k\Omega \tag{5.16}$$

By substituting (5.15) into (5.4) and evaluating the integrals, we get

$$\begin{aligned}
\dot{\tilde{\rho}}_{\alpha\beta}(t) = &- \sum_{\gamma,\delta,k,k'} I_+(\Delta_{\gamma\delta,k'}) S_{\alpha\gamma,k} S_{\gamma\delta,k'} e^{i\Delta_{\alpha\gamma,k}t + i\Delta_{\gamma\delta,k'}t} \tilde{\rho}_{\delta\beta}(t) \\
&- I_+(\Delta_{\alpha\gamma,k}) S_{\alpha\gamma,k} S_{\delta\beta,k'} e^{i\Delta_{\alpha\gamma,k}t + i\Delta_{\delta\beta,k'}t} \tilde{\rho}_{\gamma\delta}(t) \\
&- I_-(\Delta_{\delta\beta,k'}) S_{\alpha\gamma,k} S_{\delta\beta,k'} e^{i\Delta_{\alpha\gamma,k}t + i\Delta_{\delta\beta,k'}t} \tilde{\rho}_{\gamma\delta}(t) \\
&+ I_-(\Delta_{\gamma\delta,k}) S_{\gamma\delta,k} S_{\delta\beta,k'} e^{i\Delta_{\gamma\delta,k}t + i\Delta_{\delta\beta,k'}t} \tilde{\rho}_{\alpha\gamma}(t)
\end{aligned} \tag{5.17}$$

Equation 5.17 is a literature result [65] that still applies to any periodically driven system. To proceed further, different approximations can be made, corresponding to different regimes.

Time scales and rotating-wave approximations

The master equation (5.17) consists of a sum of constant terms, each multiplied by an oscillating factor of the form $e^{i(\Delta_{\alpha,\beta,k} - \Delta_{\gamma,\delta,k'})t}$. If some of this factors oscillate fast with respect to the characteristic time scale of the

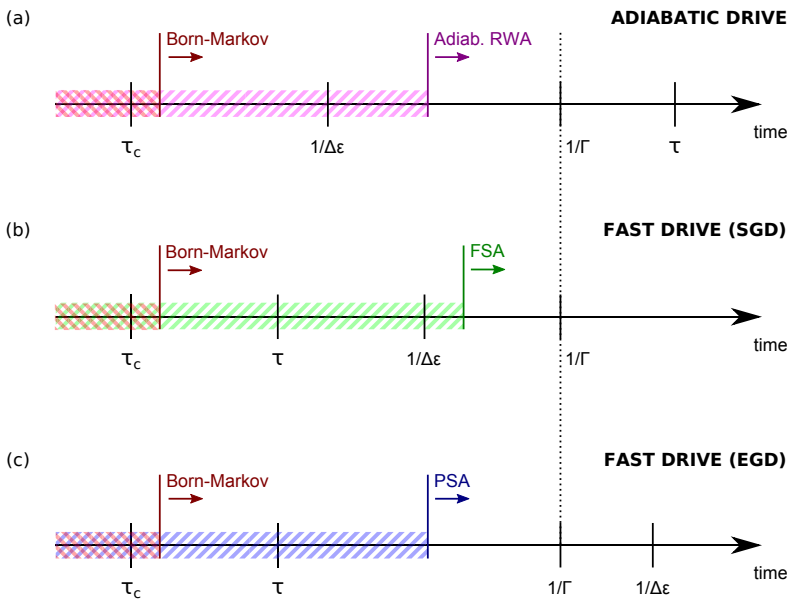

Figure 5.1. Time scales of the master equation and validity of different approximations. (a) Adiabatic limit, see Ref. [27]. (b) Fast drive, far from degeneracies in the quasienergy spectrum, see [171]. (c) Fast drive, quasi degenerate quasienergy spectrum, see Publication VII.

master equation, the dynamics is well described by an approximate master equation obtained by neglecting the corresponding terms. This procedure, which to some extent amounts to a time-coarse-graining, is generally known as secular (or rotating-wave) approximation.

Which class of terms can be neglected, depends on the collocation of the time scales of the problem. Three relevant cases are illustrated in Fig. 5.1.

Let us first consider an adiabatic drive, for which the Floquet states are well approximated by the adiabatic states introduced in Section 2.2. In that case, $\hbar\Omega \ll \bar{E}$, where $\bar{E}$ is some average energy gap between the adiabatic states. On the other hand, the assumption of weak coupling implies $h\gamma \ll \bar{E}$. It is thus legitimate to neglect the fast oscillations due to the dynamic phase $\approx \bar{E}t$, while it would be inappropriate to coarse-grain the dynamics over a drive period. A Born-Markov master equation written in terms of the adiabatic states, but not explicitly relying on Floquet analysis, was derived in Refs. [24, 25]. A derivation using Floquet theory was presented in Ref. [27]. The strategy adopted therein was to assign the fast-oscillating phases to the quasienergies while removing them from the Floquet modes, so that the quasienergy gap satisfies $\Delta\epsilon \gg h\gamma \gg \hbar\Omega$. As a result, terms oscillating as fast as $e^{i(\epsilon_\alpha - \epsilon_\beta)t}$, with $\alpha \neq \beta$, can be dropped,

while terms oscillating as $e^{ik\Omega t}$, with $k \neq 0$, must be retained. The situation is depicted in Fig. 5.1(a).

The opposite strategy is best suited for a fast drive, $\hbar\Omega \approx \bar{E}$. In particular, the quasienergies can be chosen to lie in the first Brillouin zone, so that $-\frac{1}{2}\hbar\Omega < \epsilon_\alpha \leq \frac{1}{2}\hbar\Omega$. Weak coupling now implies $\gamma \ll \Omega$, so that all terms oscillating as $e^{ik\Omega t}$, with $k \neq 0$, can be neglected. As for the terms of the form $e^{i(\epsilon_\alpha - \epsilon_\beta)t}$, $\alpha \neq \beta$, their relevance to the dynamics must be assessed case by case.

If $\gamma \ll \mathcal{E}$, as it typically happens for sufficiently weak coupling and/or far from degeneracies in the quasienergy spectrum, then all oscillating terms can be neglected; see Fig. 5.1(b). We refer to this approximation as full secular approximation (FSA). It was first derived in Ref. [171] and since then extensively used [65]. In the FSA, the master equation (5.17) becomes time-independent. Furthermore, the dynamics of populations and coherences is decoupled in the Floquet basis. After defining

$$\begin{aligned} a_{\alpha\beta,k} &= s(\Delta_{\alpha\beta,k})|S_{\alpha\beta,k}|^2 \,, \\ A_{\alpha\beta} &= \sum_k a_{\alpha\beta,k} \,, \end{aligned} \tag{5.18}$$

we have

$$\dot{\tilde{\rho}}_{\alpha\alpha} = \sum_\nu (A_{\alpha\nu}\tilde{\rho}_{\nu\nu} - A_{\nu\alpha}\tilde{\rho}_{\alpha\alpha}) \,, \tag{5.19}$$

$$\dot{\tilde{\rho}}_{\alpha\beta} = -\frac{1}{2}\sum_\nu (A_{\nu\alpha} + A_{\nu\beta})\tilde{\rho}_{\alpha\beta} \,, \text{ with } \alpha \neq \beta \,. \tag{5.20}$$

While the coherences undergo exponential decay as dictated by 5.20, the populations approach the steady-state value prescribed by 5.19. A key result of the FSA is that the steady-state density matrix is time-independent and diagonal in the Floquet basis. This establishes a strong analogy between Floquet states in a driven system and energy eigenstates in an undriven system.

In the vicinity of degeneracies in the quasienergy spectrum, the FSA breaks down, as first observed in [172, 173]. This is due to the emergence of a slow time scale, $1/\Delta\epsilon$, that can be comparable to or even slower than the decoherence time $1/\gamma$; see Fig. 5.1(c). In this case, one is allowed to neglect all terms with $k \neq k'$ but must keep those with $k = k'$ also when $\epsilon_\alpha \neq \epsilon_\beta$. This approximation, which we call partial secular approximation (PSA), is used in both Publication VII and Publication IX. As found in Publication VII, the residual time dependence due to terms oscillating like $e^{i(\epsilon_\alpha - \epsilon_\beta)t}$ cancels out when moving back from the interaction to the

Schrödinger picture. The resulting master equation can be written as

$$\dot{\rho}_{\alpha\beta} = -i(\epsilon_\alpha - \epsilon_\beta)\rho_{\alpha\beta} + \sum_{\gamma,\delta,k}[I_+(\Delta_{\gamma\delta,-k})S_{\alpha\gamma,k}S_{\gamma\delta,-k}\rho_{\delta\beta} - I_+(\Delta_{\alpha\gamma,k})S_{\alpha\gamma,k}S_{\delta\beta,-k}\rho_{\gamma\delta} - I_-(\Delta_{\delta\beta,-k})S_{\alpha\gamma,k}S_{\delta\beta,-k}\rho_{\gamma\delta} + I_-(\Delta_{\gamma\delta,k})S_{\gamma\delta,k}S_{\delta\beta,-k}\rho_{\alpha\gamma}] \, . \tag{5.21}$$

As for the FSA, (5.21) implies that the steady-state density matrix is time-independent in the Floquet basis. However, the dynamics of populations and coherences is coupled and the steady-state coherences do not vanish. Differently from the FSA, the Floquet basis is no longer the "pointer basis" for decoherence. The new pointer basis reflects a comparatively stronger interaction with the environment, whose presence "mixes" the Floquet states. The resulting regime is the subject of the next section, as well as of Publication VII.

5.2 Environment-governed dynamics

Let us consider a driven two-level system in the PSA. The equation for the coherences can be written as

$$\dot{\tilde{\rho}}_{12} = -\Gamma\tilde{\rho}_{12} + \Pi e^{-i\mathcal{E}t} \, , \tag{5.22}$$

where Γ is the coherence decay rate, Π is a rate that depends on the populations and $\mathcal{E} = \epsilon_1 - \epsilon_2$ is the quasienergy gap. [2] In the Schrödinger picture, the same equation reads

$$\dot{\rho}_{12} = i\mathcal{E}\rho_{12} - \Gamma\rho_{12} + \Pi \, , \tag{5.23}$$

whose steady-state solution is

$$\rho_{12}^{\mathrm{st}} = \frac{\Pi}{\Gamma - i\mathcal{E}} \, . \tag{5.24}$$

If $\mathcal{E} \gg \Gamma, \Pi$, then $\rho_{12} \to 0$ at steady state, in according to the result of the FSA. In general, however, this needs not to be true, even for a weakly coupled system. While the exact behavior of Γ and Π depends on the specific system considered, their scaling is proportional to $\eta^2 k_{\max}\Omega \approx \eta^2\Omega$, where $\eta^2 \ll 1$ is the dimensionless coupling strength and $k_{\max}$ is the harmonic number that gives the largest contribution to the rates. This analysis leads to the definition of the parameter

$$\xi = \frac{g^2\Omega}{\mathcal{E}} \, . \tag{5.25}$$

[2] Explicitly, $\Gamma = \frac{1}{2}\sum_{\alpha,\beta=1}^{2}\sum_k |S_{\alpha\beta,k}|^2 s(\Delta_{\alpha\beta,k})$ and $\Pi = \Pi_+ + \Pi_-(\rho_{22} - \rho_{11})$, where $\Pi_+ = \sum_k S_{11,k}S_{12,-k}[s(\Delta_{21,k}) + s(\Delta_{12,-k})]$ and $\Pi_- = \sum_k S_{11,k}S_{12,-k}[s(k\Omega) - s(-k\Omega) + s(\Delta_{21,k}) - s(\Delta_{12,-k})]$.

If $\xi \ll 1$, then the coherences undergo exponential decay, as predicted by the FSA. By contrast, if $\xi \gtrsim 1$, then the steady-state density matrix is, in general, not diagonal in the Floquet basis. This can happen as the quasienergy gap $\mathcal{E}$ can be made arbitrarily small without significantly affecting the rates Γ and Π. This feature is unique to driven systems. In fact, for an undriven system, a vanishing energy gap implies vanishing decoherence rates, at least for spectral densities of the form of (5.8).

The regime $\xi \gtrsim 1$ was explored in Publication VII. We found that the "pointer basis" – that is, the preferred basis where decoherence takes place – depends both on the coupling strength η and on the form of the operator S that couples the system to the environment. Finally, in the limit $\xi \gg 1$ (but still in the weak-coupling limit $\eta^2 \ll 1$), the pointer basis is, again, independent of η, as for the case $\xi \ll 1$. We labeled this regime as "environment-governed dynamics" ($\xi \gg 1$, EGD), as opposed to "system-governed dynamics" ($\xi \ll 1$, SGD).

In the following, we will illustrate the transition from SGD to EGD with two examples.

Example I – The Rabi Hamiltonian

As a first example, we consider the Rabi Hamiltonian

$$H(t) = \frac{E}{2}\sigma_z + g[\cos(\Omega t)\sigma_x + \sin(\Omega t)\sigma_y] \,, \tag{5.26}$$

which is analytically solvable. In particular, we can calculate Floquet states and quasienergies. The quasienergy spectrum is shown in Fig. 5.2. In particular, the quasienergy gap equals the Rabi frequency: $\mathcal{E} = \sqrt{\Delta^2 + 4g^2}$, where $\Delta = \epsilon - \omega$ is the detuning. The corresponding Floquet modes are:

$$|\phi_+(t)\rangle = \cos\theta|0\rangle - e^{-i\Omega t}\sin\theta|1\rangle \,, \tag{5.27}$$

$$|\phi_-(t)\rangle = \sin\theta|0\rangle + e^{-i\Omega t}\cos\theta|1\rangle \,, \tag{5.28}$$

where $\{|0\rangle, |1\rangle\}$ is the eigenbasis of the undriven systems and $\tan 2\theta = \frac{2g}{\Delta}$. Far from resonance, $\theta \approx 0$ and the Floquet states are the same as the undriven eigenstates. At resonance, $\theta = \frac{\pi}{4}$ and the Floquet modes are equal superpositions of $|0\rangle$ and $|1\rangle$.

We couple the system to a zero-temperature environment and consider the probability $P = \langle 1|\rho|1\rangle$ of finding the system in the excited state. For simplicity, let us first consider a resonant drive, $\Delta = 0$. If the coupling is infinitely weak, then we expect $P = 1/2$ as the system undergoes many Rabi oscillations before it interacts with the environment. By contrast, if

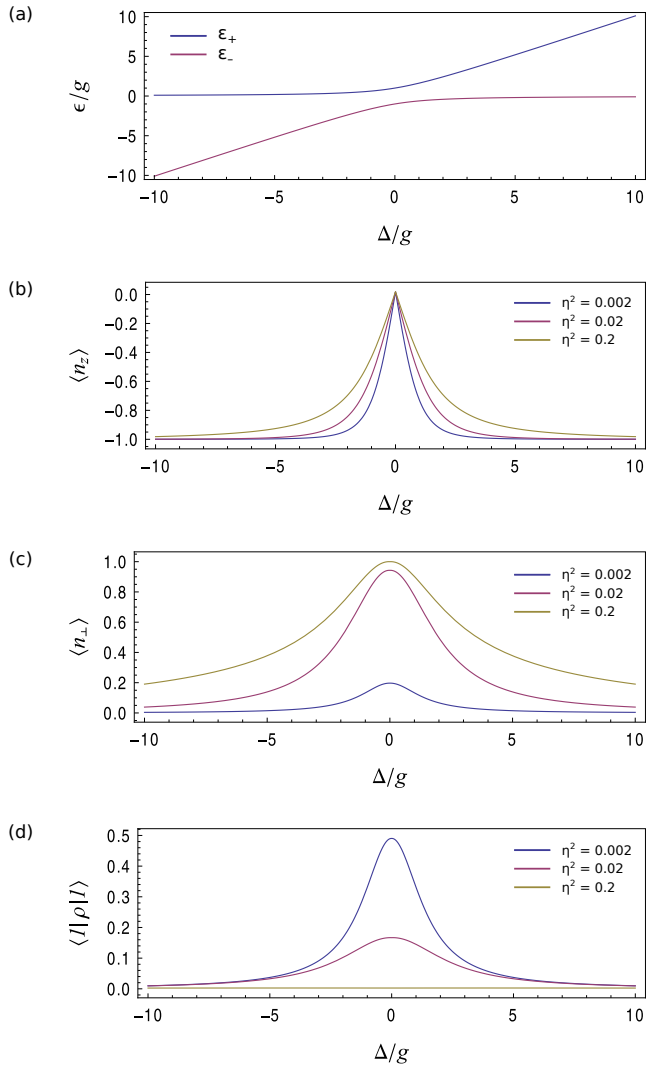

Figure 5.2. SGD to EGD transition in the Rabi model. (a) Quasienergy spectrum as a function of the normalized detuning Δ/g. (b,c) Parallel component $\langle n_z \rangle$ (b) and orthogonal component $\langle n_\perp \rangle$ (c) of the steady state with respect to the Floquet basis $\{|\phi_+\rangle, |\phi_-\rangle\}$. (d) Corresponding excited-state probability $\langle 1|\rho|1\rangle$. In (b-d), $E \gg g$, $S = \sigma_x$ and different values of the coupling parameter η are used.

the coupling is “very strong", it will tend to keep the system in the ground state, so that we expect $P \approx 0$. What does “very strong” mean? Intuitively, it means that the relaxation rate must be faster than the frequency of the Rabi oscillations. Now, the relaxation rate is proportional to $g^2\Omega$ for a transverse coupling operator ($S = \sigma_x$) and the Rabi frequency equals the quasienergy gap. Putting things together, our “strong coupling” condition directly translates into $\xi \gg 1$, that is, the EGD limit.

In Fig. 5.2(b,c) we plot the parallel component $n_z = \mathrm{Tr}[\sigma_z\rho]$ (b) and the orthogonal component $n_\perp = [\mathrm{Tr}^2(\sigma_x\rho) + \mathrm{Tr}^2(\sigma_y\rho)]^{1/2}$ (c) of the steady-state density matrix in the Floquet basis versus the detuning Δ and for different values of the coupling strength η. Upon increasing η, the pointer basis becomes essentially orthogonal to the Floquet basis in a neighborhood of the resonant frequency. In Fig. 5.2(d), we plot the corresponding population in the excited state of the fixed basis. In the EGD limit, the system is kept in the ground state, in agreement with the heuristic argument given above.

This simple example, which admits a clear physical interpretation, tells a nontrivial truth on the general validity of a certain master equation. Notice that if the steady-state basis were the Floquet basis (as predicted by the FSA), then one would have $P = \frac{1}{2}$ regardless of the coupling strength.

Example II – The Cooper-pair sluice

As a second example, we consider the Cooper-pair sluice, with the Hamiltonian and driving cycle given in Section 2.3. When the sluice is driven fast, the repeated sequence of Landau-Zener crossings gives rise to Landau-Zener-Stückelberg interference patterns, as we discussed in Section 2.5. The geometric phase accumulated during the sectors of adiabatic evolution is controlled by the superconducting phase bias φ, giving access to purely geometric interferometry. Due to the periodicity of the pumping cycle, the dynamics of the sluice and the resulting pumped charge lend themselves to a Floquet-based approach. A first, significant step in this direction was taken in Ref. [28]. In particular, it was there found that the total charge Q_α^{tr} transferred by the α-th Floquet state is given by

$$Q_\alpha^{\mathrm{tr}}/2e = \frac{\tau}{\hbar}\frac{\partial\epsilon_\alpha(\varphi)}{\partial\varphi} \,. \tag{5.29}$$

Equation (5.29) generalizes (2.18) and (2.19) to the nonadiabatic case. Furthermore, it establishes a direct link between the quasienergy spec-

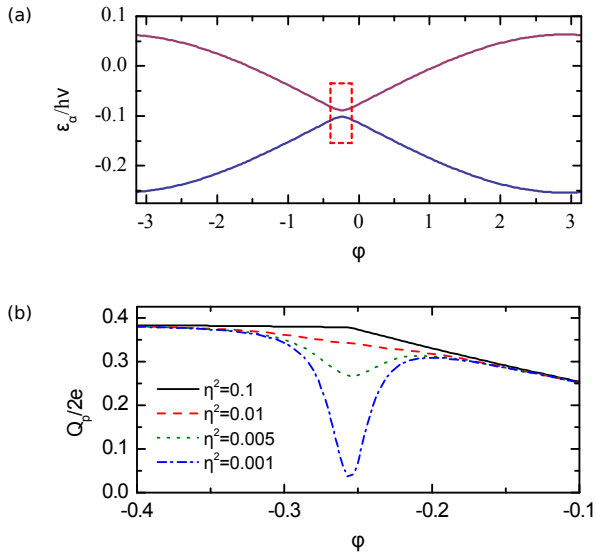

Figure 5.3. SGD to EGD transition in the Cooper-pair sluice: quasienergy spectrum and pumped charge. (a) Quasienergy spectrum of the fast-driven sluice, as a function of the superconducting phase bias φ. (b) Steady-state pumped charge versus φ in the vicinity of the quasienergy anticrossing, for different values of the system-environment coupling coefficient η.

trum and the pumped charge [3].

In Fig. 5.3(a), we plot the numerically exact quasienergy spectrum of the sluice versus φ for a representative choice of parameters. It was obtained by solving the equation $i\hbar\partial_t U(t) = H(t)U(t)$ over a period and diagonalizing $U(\tau)$. Keeping (5.29) in mind, it is natural to correlate constructive interference [see Fig. 2.9(b)] with the smooth plateaux around $\varphi = 2.88$, where the pumped charge vanishes for both Floquet states. Less intuitive is the interpretation of the weakly avoided quasienergy crossing at $\varphi = -0.26$, for at that point the adiabatic-impulse model [see Section 2.5] would predict destructive interference, corresponding to a maximum in the pumped charge. As it turns out, destructive interference is not robust against nonadiabatic corrections in the supposedly adiabatic sectors, resulting in the opening of a small gap in the quasienergy spectrum [174]. This small gap is also associated to a vanishing pumped charge for each

[3] Strictly speaking, the transferred charge is the sum of two terms, associated with the leakage supercurrent (or the dynamic phase) and the pumped current (or the geometric phase); compare Section 2.2. In the following and for simplicity, we assume that the supercurrent term does not contribute (this amounts to assuming ideal SQUIDs).

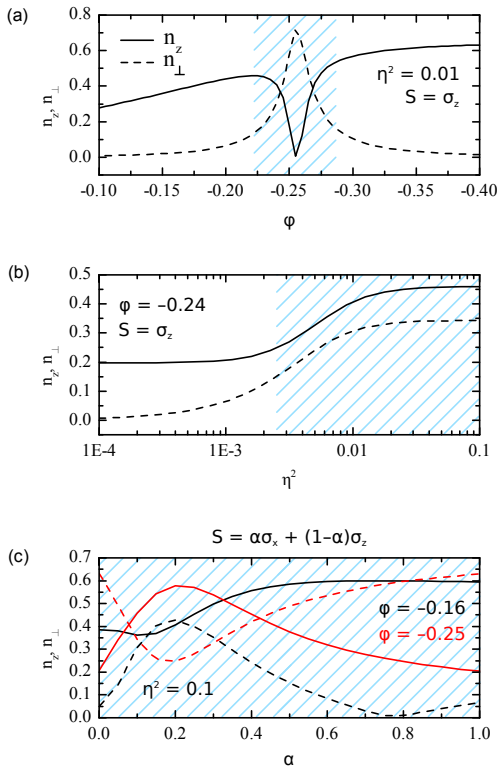

Figure 5.4. SGD-to-EGD transition in the Cooper-pair sluice: pointer basis. Steady-state projections $\langle n_z \rangle$ (full lines) and $\langle n_\perp \rangle$ (dashed lines) versus φ in a neighborhood of the weakly avoided energy crossing (a), versus η^2 (b), and versus α (c). EGD is attained is the highlighted regions.

Floquet state.

In Fig. 5.3(b), we plot the steady-state pumped charge $Q_p^{\rm st}$ versus φ in a neighborhood of the avoided quasienergy crossing. The sluice is coupled to a zero-temperature, ohmic environment by the coupling operator $S = \sigma_z$. For very weak coupling η, a dip is indeed observed in $Q_p^{\rm st}$. However, as η is increased, the dip recedes and eventually disappears: the presence of the environment has stabilized the dynamics against the nonadiabatic perturbation. This result must be regarded as direct evidence of EGD, as it implies that the steady-state coherences are not vanishing in the Floquet basis. A closer look at the steady-state density matrix confirms this picture. In Fig. 5.4, we plot the parallel and orthogonal components of the Bloch vector with respect to the Floquet basis. In panel (a), we show that for a moderate coupling to the environment ($\eta^2 = 0.01$), EGD is indeed attained close to the quasienergy anticrossing. In panel (b),

we show that for a fixed value of φ, the transition from SGD to EGD, signaled by a nonvanishing $n_\perp$, is determined by the coupling parameter η. Finally, we introduce a family of coupling operators $S = \alpha\sigma_x + (1-\alpha)\sigma_z$, parametrized by $\alpha \in [0,1]$. In panel (c), we show that in the EGD limit the pointer basis critically depends on the coupling operator, a characteristic feature of EGD.

5.3 Lamb shift of a driven quantum system

When evaluating the integrals of the correlation function appearing in the master equation, the principal-value integrals (5.12) are often neglected. In an undriven system, they lead to a small ($\lesssim 1\%$) renormalization of the unperturbed energy levels, induced by the system-environment coupling [169]. For this reason, they are referred to as "Lamb shift", in close analogy with the shift observed in atomic spectra due to the interaction between bound electrons and the microwave field [175, 176].

Let us consider the Floquet-Born-Markov master equation in the PSA, Eq. (5.21). This can be regarded as a Bloch-Redfield-type master equation, with quasienergies playing the role of energies and "exotic" rates which do not obey detailed balance. In this spirit, let us write (5.21) as

$$\dot{\rho}_{\alpha\beta} = -i(\epsilon_\alpha - \epsilon_\beta)\rho_{\alpha\beta} + \sum_{\gamma,\delta} \left[\mathcal{R}_{\alpha\beta\gamma\delta} + i\tilde{\mathcal{R}}_{\alpha\beta\gamma\delta}\right] \rho_{\gamma\delta} \,, \tag{5.30}$$

where $\mathcal{R}$ is the Redfield tensor and $\tilde{\mathcal{R}}$ the correction due to the principal-value integrals (5.12). In the undriven case [169], the correction amounts to a renormalization of the bare energies: $\tilde{\mathcal{R}}_{\alpha\beta\gamma\delta} = \delta_{\gamma\alpha}\delta_{\delta\beta}(\tilde{\epsilon}_\alpha - \tilde{\epsilon}_\beta)$. In the driven case, $\tilde{\mathcal{R}}$ includes other terms, too. However, there is a good reason to focus on the terms of the form $\tilde{\mathcal{R}}_{\alpha\beta\alpha\beta}$, with $\alpha \neq \beta$. This class of terms provides a renormalization of quasienergies, which, albeit small, can be extremely significant close to degeneracies in the Floquet spectrum.

In Publication IX, we explicitly calculate the environment-induced renormalization of the quasienergies, that can be regarded as the Lamb shift of a strongly driven quantum system. We also show that, in relative terms, the renormalization can be much larger than what is typically observed in an undriven system. As an analytically tractable example, we again consider the semiclassical Rabi model. Finally, we discuss its implementation in superconducting circuits, in particular, the Cooper-pair box and the Cooper-pair sluice.

The correction $\tilde{\mathcal{E}}_{\alpha\beta}$ to the quasienergy gap $\mathcal{E}_{\alpha\beta} = \epsilon_\alpha - \epsilon_\beta$ is given by

$$\tilde{\mathcal{E}}_{\alpha\beta} = \frac{1}{\pi\hbar} \sum_{\mu,k} \left[\mathcal{G}_+(\Delta_{\mu\alpha,k}) |S_{\mu\alpha,k}|^2 + \mathcal{G}_-(\Delta_{\beta\mu,k}) |S_{\beta\mu,k}|^2 \right] \tag{5.31}$$

For an Ohmic spectral density of the form (5.8) with $s = 1$ and at zero temperature, the integrals (5.12) can be reduced to the exponential integral $\mathrm{Ei}(x) = -\int_x^\infty \frac{e^{-t}}{t} dt$. For a two-level system, the correction reads

$$\tilde{\mathcal{E}}_{12} = \frac{\eta^2}{\pi} \sum_k \omega_c \, g(\Delta_{21,k}) |S_{21,k}|^2 \tag{5.32}$$

where $g(x) = x \left[\mathrm{Ei}(x) \, \mathrm{e}^{-x} + \mathrm{Ei}(-x) \, \mathrm{e}^{x} \right]$. If ω_c is much larger than all characteristic energy scales of the driven system, then we can approximate $g(x) \approx 2x \ln(|x|)$ and

$$\tilde{\mathcal{E}}_{12} = \frac{\eta^2}{\pi} \sum_k \left[\Delta_{21,k} |S_{21,k}|^2 \ln \frac{|\Delta_{21,k}|}{\omega_c} \right] . \tag{5.33}$$

Equation (5.33) can be readily applied to the Rabi model in the case of transverse coupling ($S = \sigma_x$) and longitudinal coupling ($S = \sigma_z$). The behavior of the quasienergy gap in each case is analyzed in Fig. 5.5 for representative parameter values. The left panels refer to $S = \sigma_x$ and the right panels to $S = \sigma_z$. In panels (a,b), we compare the renormalized quasienergy gap $\mathcal{E}_{12} + \tilde{\mathcal{E}}_{12}$ (solid lines) to the bare quasienergy gap $\mathcal{E}_{12}$ (dashed lines). In particular, for transverse coupling, we find a pronounced asymmetry with respect to negative and positive detuning. In panels (c,d), we plot the ratio $\tilde{\mathcal{E}}_{12}/\mathcal{E}_{12}$. In both cases, the ratio is much larger than the few-percent value observed, e.g., in [177]. Even if we derived this result for an ohmic environment, similarly high ratios can be found for a quasi-single-mode reservoir; see Publication IX, Supplemental Material. Finally, in panel (e,f), we plot $\mathcal{E}_{12} + \tilde{\mathcal{E}}_{12}$ and $\mathcal{E}_{12}$ versus the driving amplitude g for a slightly blue-detuned drive ($\Delta/E = 0.005$). Interestingly, the dependence of the renormalized gap on g is nonmonotonic for the case $S = \sigma_x$, a clear-cut prediction to be tested against an experiment.

Strongly driven superconducting circuits, in particular Cooper-pair boxes, are natural candidates for studying these effects. Due to their large dipole moment, Cooper-pair boxes are coupled to their environment over a broad range of frequencies. Feasible experimental conditions for observing the quasienergy renormalization are discussed in more detail in Publication IX. As a matter of fact, many recent experiments on Cooper-pair boxes [178, 179, 180, 181] can be interpreted in terms of probe spectroscopy of quasienergy states [182]. We believe these set-ups would provide a convenient testbed for our approach.

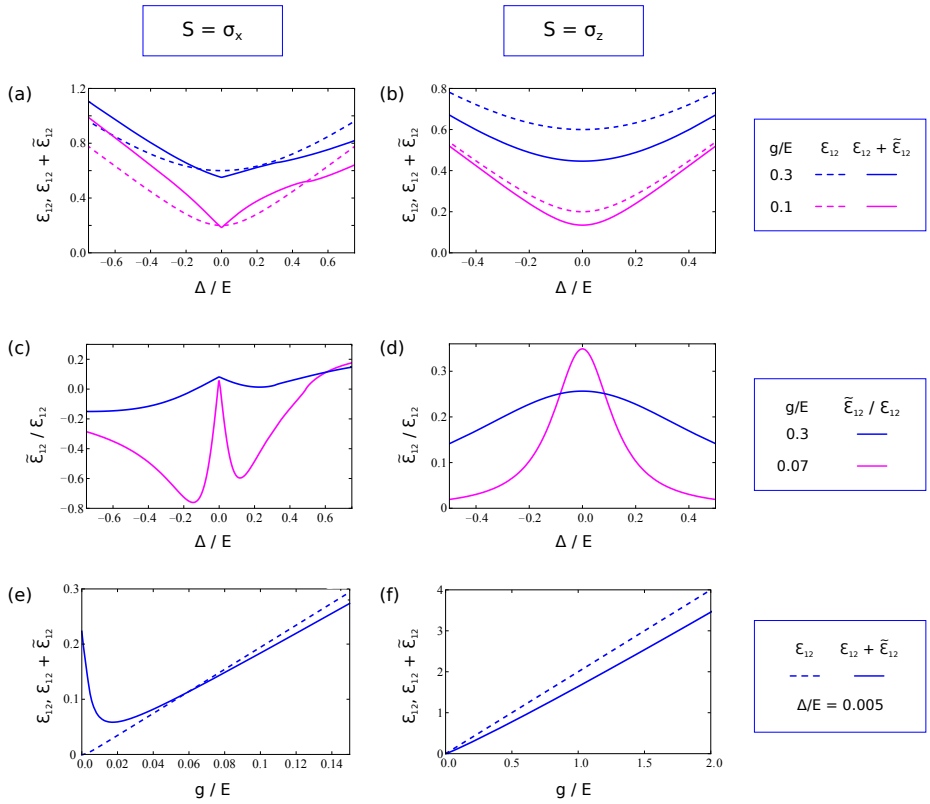

Figure 5.5. Lamb shift of a driven quantum system. Quasienergy renormalization (Lamb shift) in the Rabi model with transverse coupling ($S = \sigma_x$, left) and longitudinal coupling ($S = \sigma_z$, right). The environment is an Ohmic bath with cutoff frequency $\omega_c = 60E$ and coupling coefficient $\eta^2 = 0.1$. (a,b) Renormalized quasienergy gap $\mathcal{E}_{12} + \tilde{\mathcal{E}}_{12}$ (solid lines) and bare quasienergy gap $\mathcal{E}_{12}$ (dashed lines) versus normalized detuning Δ/E, for two different driving amplitudes. (c,d) Corresponding relative strength $\tilde{\mathcal{E}}_{12}/\mathcal{E}_{12}$ of the Lamb-shift correction. (e,f) Renormalized (solid) and bare (dashed) quasienergy gap versus the normalized driving amplitude g/Δ for a slightly blue-detuned drive ($\Delta/E = 0.005$).

5.4 Heat-exchange statistics in driven quantum systems

In the previous sections, we analyzed the influence of the environment on the dynamics of a periodically driven system. This scenario can also be considered from a thermodynamical perspective: the system is acted upon by an external force that does work on it while exchanging energy with a heat bath. In Publication X, we take the "side" of the environment as we study the statistics of energy exchanges between a periodically driven quantum system and a heat bath. By combining a generalized master equation formalism [128] with Floquet theory [65], we formally derive the characteristic generating function of the distribution, from which all the cumulants of the energy distribution can be derived. Furthermore, in the long time limit, we explicitly write down the full probability distribution in a general form. By highlighting the contribution of each individual energy exchange, the full distribution provides us with a deeper insight into the thermalization process. We illustrate these concepts by applying them to the semiclassical Rabi problem and find that different coupling operators S result in very different energy-exchange processes. Our formalism can be straightforwardly generalized to consider multi-level systems and multiple heat baths; as such, it could be used to study the performance of quantum heat engines [23].

Generalized master equation and energy-exchange distribution

We consider the same setting as in Section 5.1, defined by the Hamiltonian (5.1). Our quantity of interest is the probability density distribution $P(Q,t)$ for the environment to exchange the amount of energy Q between times 0 and t. This is given by

$$P(Q,t) = \sum_{e_1,e_2} \delta(e_2 - e_1 - Q) p[e_2;e_1] p[e_1] \,, \tag{5.34}$$

where $p[e_2;e_1]$ is the conditional probability that a measurement of H_B gives e_2 at time t when it gave e_1 at time t_0 and $p[e_1]$ is the probability to measure e_1 at time t_0. Introducing the projector P_{e_j} on the j-th state of the reservoir of energy e_j and using the property $P_{e_j}^2 = P_{e_j}$, we have

$$\begin{aligned} p[e_2,e_1]p[e_1] &= \mathrm{Tr}[P_{e_2}U(t)P_{e_1}\rho_T(0)P_{e_1}U^\dagger(t)P_{e_2}] \\ &= \mathrm{Tr}[U^\dagger(t)P_{e_2}U(t)P_{e_1}\rho_T(0)P_{e_1}]. \end{aligned} \tag{5.35}$$

where $/rho_T$ is the total (system+environment) density matrix and $U(t)$ is the evolution operator generated by $H_T(t)$. It is convenient to introduce

the characteristic generating function

$$G(\lambda,t) \equiv \int_{-\infty}^{\infty} dQ P(Q,t) e^{iQ\lambda} = \sum_{e_1,e_2} p[e_2;e_1]p[e_1]e^{i\lambda(e_2-e_1)} \ , \tag{5.36}$$

so that the moments of Q are given by

$$\langle Q^n(t)\rangle = (-i)^n \left.\frac{d^n G(\lambda,t)}{d\lambda^n}\right|_{\lambda=0} \ . \tag{5.37}$$

If we assume the initial total density matrix to be factorized as $\rho_T(0) = \rho(0)\otimes\rho_B(0)$ (as we did in Section 5.1), then all projectors P_{e_j} commute with $\rho_T(0)$, so that the initial measurement of H_B does not change the subsequent dynamics. After noticing that $\sum_{e_j} P_{e_j} e^{\pm i\lambda e_j} = e^{\pm i\lambda H_R}$, we write (5.36) as

$$G(\lambda,t) = \mathrm{Tr}[U^\dagger(t) e^{i\lambda H_R} U(t) e^{-i\lambda H_R} \rho_T(0)] \tag{5.38}$$

and finally as

$$G(\lambda,t) = \mathrm{Tr}[\rho_T^\lambda(t)] \ , \tag{5.39}$$

where

$$\rho_T^\lambda(t) = U_{\lambda/2}(t)\rho_T(0)U^\dagger_{-\lambda/2}(t) \tag{5.40}$$

and

$$U_\lambda(t) = e^{i\lambda H_R} U(t) e^{-i\lambda H_R} \tag{5.41}$$

satisfies the equation of motion

$$i dU_\lambda(t)/dt = H_\lambda(t) U_\lambda(t) \ , \tag{5.42}$$

with $H_\lambda(t) = e^{i\lambda H_R} H_T(t) e^{-i\lambda H_R}$.

Starting from (5.40), we derive a generalized master equation for $\rho^\lambda = \mathrm{Tr}_B[\rho_T^\lambda]$. Mutatis mutandis, the derivation follows that presented in Section 5.1. Notice that U_λ is not a unitary operator, so that (5.3) must be replaced by

$$i\hbar\frac{d}{dt}\tilde{\rho}_T^\lambda(t) = -i\left[\tilde{V}_\lambda(t)\tilde{\rho}_T^\lambda(t) - \tilde{\rho}_T^\lambda(t)\tilde{V}_\lambda(t)\right] \ . \tag{5.43}$$

The general result in the Born-Markov approximation, to be compared to (5.4), is

$$\begin{aligned}\frac{\partial}{\partial t}\tilde{\rho}^\lambda(t) = -\int_0^\infty d\tau \Big[& g(\tau)\tilde{S}(t)\tilde{S}(t-\tau)\tilde{\rho}^\lambda(t) - g(-\lambda+\tau)\tilde{S}(t-\tau)\tilde{\rho}^\lambda(t)\tilde{S}(t) \\ & -g(-\lambda-\tau)\tilde{S}(t)\tilde{\rho}^\lambda(t)\tilde{S}(t-\tau) + g(-\tau)\tilde{\rho}^\lambda(t)\tilde{S}(t-\tau)\tilde{S}(t)\Big]\end{aligned} \tag{5.44}$$

As expected, (5.4) is recovered from (5.44) in the limit $\lambda \to 0$.

Application of the Floquet theory is also straightforward. We will present the result for a two level system and in the FSA. In the FSA, the populations $\rho^{\lambda}_{\alpha\alpha} = \langle\Psi_\alpha|\rho^{\lambda}|\Psi_\alpha\rangle$ are decoupled from the coherences and satisfy a vector equation of the form

$$\dot{\vec{\rho}}^{\lambda} = \mathcal{A}\vec{\rho}^{\lambda} \,, \tag{5.45}$$

where $\vec{\rho}^{\lambda} = \{\rho^{\lambda}_{11}, \rho^{\lambda}_{22}\}$. After recalling the definitions (5.18) and defining

$$A^{\lambda}_{\alpha\beta} = \sum_k e^{-i\lambda\Delta_{\alpha\beta,k}} a_{\alpha\beta,k} \,, \tag{5.46}$$

we can write the matrix $\mathcal{A}$ as

$$\mathcal{A} = \begin{pmatrix} A^{\lambda}_{11} - A_{11} - A_{21} & A^{\lambda}_{12} \\ A^{\lambda}_{21} & A^{\lambda}_{22} - A_{22} - A_{12} \end{pmatrix} \,. \tag{5.47}$$

Equations (5.45) and (5.47) are the starting point of the analysis of Publication X.

General results

Even before solving (5.45), the knowledge of $\dot{\rho}^{\lambda}$ can be used to evaluate the mean heat power $\langle\dot{Q}\rangle = d\langle Q\rangle/dt$ transferred to the reservoir at any time:

$$\langle\dot{Q}\rangle = -\sum_{\alpha,\beta,k} \Delta_{\alpha\beta,k}\, a_{\alpha\beta,k}\, \rho_{\beta\beta} \,. \tag{5.48}$$

In particular, at dynamic steady state, one has

$$\langle\dot{Q}\rangle = -\frac{1}{2}\sum_k (k\Omega)\,(a_{11,k} + a_{22,k}) - \frac{1}{A_{12}+A_{21}}\sum_{h,k} (k\Omega + h\Omega)\, a_{12,k} a_{21,h} \,. \tag{5.49}$$

Equation (5.49) can be used to classify open driven quantum systems into two categories: those that exchange heat at steady-state, and those that do not. In general and in contrast to the undriven case, a driven system will keep exchanging energy with the environment unless its dressed (Floquet) states are decoupled (for instance, by symmetry) from the noise. This result was also obtained in Refs. [183, 184] by using a standard master equation approach and associating the relaxation processes to the dissipated heat.

By solving (5.45), we get a formal expression for the characteristic generating function:

$$G(\lambda, t) = c^{\lambda}_{-} e^{\xi_-(\lambda)t} + c^{\lambda}_{+} e^{\xi_+(\lambda)t} \,, \tag{5.50}$$

where $\xi_\pm(\lambda)$ are the eigenvalues of $\mathcal{A}$ and $c^{\lambda}_{\pm}$ the projection of the initial density matrix $\rho(0)$ onto the corresponding eigenvectors $v^{\lambda}_{\pm}$, normalized so

that $\mathrm{Tr}\, v_{\pm}^{\lambda} = 1$. Many properties of the heat distribution can be obtained from (5.50); for a detailed analysis, see Publication X. In particular, the first few moments of the distribution can be straightforwardly calculated. Furthermore, the explicit knowledge of $G(\lambda, t)$ allows us to retrieve the full $P(Q, t)$ at any given time. This requires inverting the Fourier transform, a task which in general must be performed numerically. However, some analytical insight can be gained in the long-time limit. We first notice that $\Re\mathrm{e}\, \xi_{-}(\lambda)$ is always negative, while $\Re\mathrm{e}\, \xi_{+}(\lambda)$ is negative everywhere except at $\lambda_n = n\tau$, $n \in \mathcal{Z}$, where it vanishes. In the long-time limit, $G(\lambda, t)$ thus localizes at a countable number of values. By expanding $\xi_{+}(\lambda)$ up to the second order in $\lambda - \lambda_n$ (Gaussian approximation), we can invert the Fourier transform analytically and find that

$$P(Q,t) = w(Q,t)\Omega \sum_k \Big[p_{\downarrow}\delta(Q + \epsilon_1 - \epsilon_2 + k\Omega) + p_{\uparrow}\delta(Q + \epsilon_2 - \epsilon_1 + k\Omega) + (1 - p_{\uparrow} - p_{\downarrow})\delta(Q + k\Omega) \Big] , \tag{5.51}$$

where $p_{\uparrow} = A_{21}/(A_{21} + A_{12})\rho_{11}(0)$, $p_{\downarrow} = A_{12}/(A_{21} + A_{12})\rho_{22}(0)$ and

$$w(Q,t) = \frac{1}{\sqrt{2\pi}} \frac{1}{\sqrt{2bt\Omega}} \exp\left[-\frac{(Q - at\Omega)^2}{4bt\Omega^2} \right] , \tag{5.52}$$

with real coefficients $a = -i\xi_{+}^{(1)}(0) \geq 0$ and $b = -1/2\xi_{+}^{(2)}(0) \geq 0$. Eqs. (5.51) and (5.52) suggest an insightful interpretation of the energy-exchange process. The delta functions account for the fact that the exchanges take place only in multiples of $\Delta_{\alpha\beta,k}$. This results from energy being available in photons of energy Ω, the drive frequency, and $\epsilon_2 - \epsilon_1$, the dressed energy gap of the driven system. Furthermore, they tell that the system is either found in the same Floquet state or has undergone a transition upwards (downwards), with probability $1 - p_{\uparrow} - p_{\downarrow}$ and $p_{\uparrow}$ ($p_{\downarrow}$), respectively. On the other hand, the total probability that a certain amount of energy has been exchanged is dictated by the weight function $w(Q, t)$. An appealing feature of (5.51) is that it clearly shows how the heat-exchange distribution "builds up" on individual exchanges of well-defined energy. One should keep in mind, however, that it was derived under the assumption that $G(\lambda, t)$ is localized at the nodes $\lambda = n\tau$. This assumption holds true only in the limit where many energy quanta have been exchanged. For very long times, $t \gg 1/b$, one can neglect the discretization due to the Dirac combs in (5.51) and find that $P(Q, t) \approx w(Q, t)$.

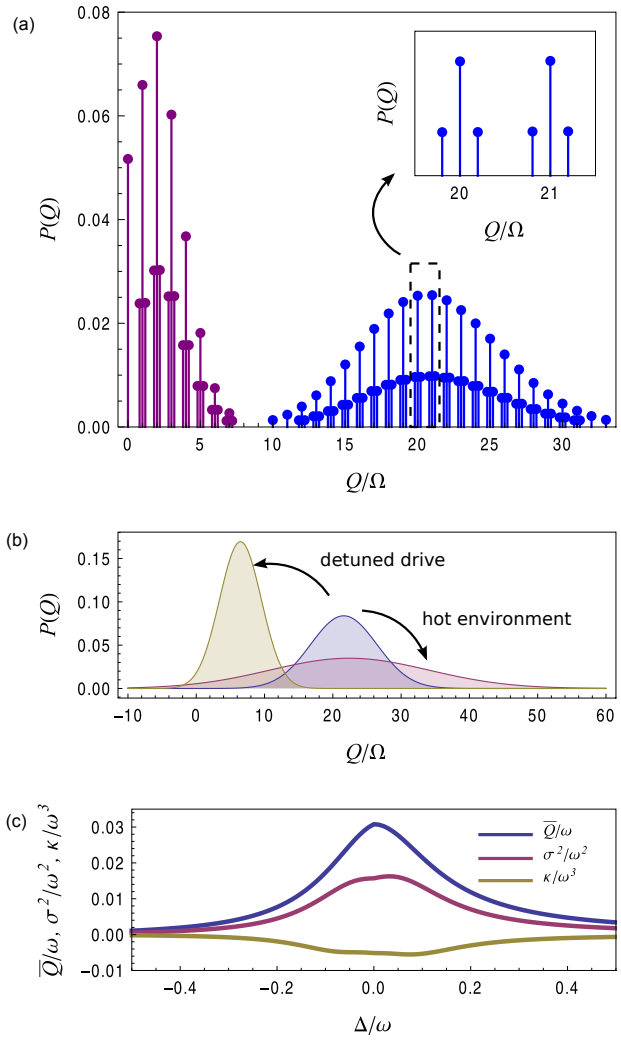

Figure 5.6. Rabi model: dissipated energy for transverse coupling. (a) PDD at $t/\tau = 80$ (purple) and $t/\tau = 700$ (blue). Inset: triplets at frequencies $k\Omega$, and $k\Omega \pm \mathcal{E}$. (b) Effect of temperature and detuning on $w(Q,t)$.a Temperature is changed from $k_BT = 0.1\omega$ to $k_BT = 3\omega$. The detuning is changed from $\Delta = 0.02\omega$ to $\Delta = 0.3\omega$. (c) Mean value $\bar{Q}$ (blue), variance σ^2 (purple) and skewness κ (yellow) of the PDD as a function of the detuning Δ. For all panels, the initial state is the DSS, $t/\tau = 700$, $g = 0.1\omega$, $\Delta = 0.02\omega$, $\varphi = 0$, $k_BT = 0.1\omega$ and $\eta = 0.01$.

Example – the Rabi model

Let us consider, once more, the Rabi model with the coupling operators $S = \sigma_x$ and $S = \sigma_z$. When $S = \sigma_x$, (5.48) tells that the heat current is, in general, nonvanishing. In physical terms, the system is continuously "pumped" by the drive and emits photons to the environment, resulting in a net heat flow to the environment. The full probability distribution is shown in Fig. 5.6(a) at two different times, starting from the dynamic steady state. It was obtained from the analytical solution (5.50) by numerically inverting the Fourier transform. The structure of the PDD is the same as in (5.51): a series of Dirac combs modulated by an envelope which moves in time. As best seen in the Inset, the spectrum of possible energies is composed by symmetric triplets centered at integer multiples of Ω and spaced by an amount Ω_R. This can be regarded as a calorimetric characterization of the well-known Mollow triplet observed in quantum-optics experiments [185, 186, 187]. Notice that the envelope function of the PDD is manifestly non-Gaussian at early times.

In Fig. 5.6 (b,c), we show how the long-time-limit distribution is affected by changes in the drive frequency and the temperature of the environment. In panel (b), we plot the Gaussian envelope function $w(Q,t)$ for three representative cases. In passing from low to high temperature, the mean value of the distribution is barely affected, while the variance strongly increases. The fact that temperature has little influence on the average dissipated heat is related to the fact that – differently from an undriven system – the transition rates $A_{\alpha\beta}$ do not satisfy the detailed balance. In contrast, the variance of the distribution depends on the temperature, due to the fact that a higher-temperature environment leads to stronger noise effects. In passing from a resonant to a red-detuned drive, the PDD shows reduced average and variance because of the reduction of the energy injected in the system that can then be dissipated. This is confirmed by the behavior of the central moments as a function of the detuning Δ, shown in panel (c).

Finally, let us consider the noise operator $S = \sigma_z$. In this case, (5.49) tells that the mean heat power vanishes at dynamic steady state. This is due to the symmetry of the problem, which forbids transitions with energy exchange $n\Omega$, thereby causing the drive and the environment to be effectively decoupled. This is confirmed by the full solution of the master equation, which is formally equivalent to that of an undriven system. As

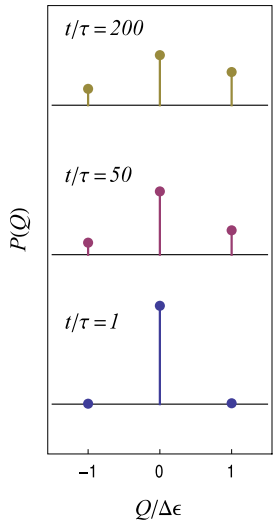

Figure 5.7. Rabi model: dissipated energy for longitudinal coupling. PDD at different times for longitudinal coupling ($S = \sigma_z$).

a result, the amount of dissipated heat is much smaller (a single transition is allowed) and depends critically on the initial state. In this sense, the distribution can be regarded as a calorimetric fingerprint of decoherence, which carries information on the initial state. A sample distribution is shown in Fig. 5.7, at different times and with $|0\rangle$ as the initial state. More details can be found in Publication X, where we also show that the distribution can be sensitive to the phase of the drive and that its mean value can be negative, meaning that the system is more likely to absorb energy and the environment is more likely to release it.

Outlook

Before turning to experimental implementations, we list some possible extensions of this work. First of all, the FSA could be replaced by a PSA, at the only expense of more complicated analytical expressions. This would make it possible to address the EGD regime described in Section 5.2 from the point of view of energy exchanges. Furthermore, several techniques developed in the context of the full-counting statistics may be adapted to the present formalism, also thanks to the fact that the Floquet picture turns a time-dependent problem into a time-independent one (at least, in the limits described in Section 5.1). Finally, it would be interesting to extend this formalism to nonmarkovian environments, perhaps in the

spirit of Refs. [188, 189].

Our predictions could be tested in a variety of physical systems, for example, superconducting quantum bits embedded in a resistive environment [130, 15] and/or integrated in a circuit-quantum-electrodynamics architecture [190]. In any case, the availability of a fast microcalorimeter of the type discussed in Chapter 4 is indispensable. For example, let us take the proposal of Ref. [15], discussed in Section 4.1. Voltage fluctuations across the resistor induce fluctuations in the potential on the island (charge noise), so that the coupling operator is $S = \sigma_z$. The corresponding spectral density can be evaluated by taking into account the circuit of Fig. 4.1. The result is an ohmic spectral density with Lorentzian cutoff, as described by (5.8) with $s = 1$. The coupling strength is $\eta^2 = R_{\rm eff}/R_Q$ and the cutoff frequency is $\omega_c = 1/(R_{\rm eff}C_{\rm eff})$, where we have introduced the quantities $R_{\rm eff} = (C_g/C_\Sigma)R$, $C_{\rm eff} = C_J C_\Sigma/C_g$, and $R_K = \hbar/e^2$. Realistic experimental parameters are $R = 200\,\Omega$, $C_g = 500\,\mathrm{aW}$, $C_J = 1\,\mathrm{fF}$, $E_C = e^2/(2C_\Sigma) = k_B \cdot 1\,\mathrm{K}$. Then the maximum energy of the emitted photons is $4E_C = h \cdot 80\,\mathrm{GHz}$, well below the cutoff frequency $\omega_c/(2\pi) = 1.6\,\mathrm{THz}$. The coupling parameter is $\eta^2 = 5 \times 10^{-4}$, well in the weak coupling regime. The characteristic relaxation rate due to the presence of the resistor is of the order of $1/(\eta^2 E_C) = 100\,\mathrm{ns}$. This time must be compared with the intrinsic relaxation time of the Cooper-pair box (typically, a few hundred ns), to determine which fraction of the emitted photons are collected by the resistor. Ideally, one would like this fraction to approach unity, implying that decoherence in the Cooper-pair box is essentially due to the presence of the resistor.

The possibility to control the Cooper-pair box on much faster time scales (tens of ns) than the thermal relaxation time of the resistor (tens of $\mu\mathrm{s}$) [191] suggests that energy distributions such as the one shown in Fig. 5.6 could be measured by driving the system over many periods within the thermal relaxation time, thereby allowing the energy of many photons to "pile up" in the resistor. However, resolving the energy peaks of Fig. 5.6 still requires good single-shot fidelity for photons of energy $\hbar\Omega$, which, in turn, calls for a substantial improvement from Publication XI.

6. Experimental techniques

In this chapter we give a brief summary of the most important experimental techniques used in this work.

6.1 Device fabrication

The samples measured in this thesis were fabricated using standard micro and nanofabrication processes, including optical and electron-beam lithography, thermal and electron-beam metal evaporation, thermal annealing, wet etching, in-situ oxidation, and liftoff. The devices described in Chapter 3 were fabricated in the cleanroom of the NEST laboratories, Pisa. Those described in Chapters 2 and 4 were fabricated in the Micronova Nanofabrication Center, Espoo, a research facility shared by VTT and Aalto University.

Quantum dots and quantum point contacts in 2DEGs

We start from a two-inch wafer of Si-doped GaAs/AlGaAs heterostructure, grown by molecular-beam epitaxy (MBE) in the TASC National Laboratory, Trieste. The 2DEG is defined $100\,\mathrm{nm}$ below the surface. The carrier density and mobility, measured in an etched Hall bar with the Van der Pauw method and by Shubnikov-de Haas oscillations, typically exceeded $1 \times 10^{11}\,\mathrm{cm}^{-2}$ and $1 \times 10^{6}\,\mathrm{cm}^{2}\mathrm{V}^{-1}\mathrm{s}^{-1}$, respectively.

We first cleave the wafer into $2\,\mathrm{mm} \times 2\,\mathrm{mm}$ chips, each chip accommodating four samples. As the first step, we define the "mesa", which delimits the 2DEG regions to be contacted. We draw the mesa pattern, together with alignment markers, using either optical lithography or e-beam lithography. In the latter case, it is convenient to use a negative resist to reduce exposure time. After exposure and development, we soak the chip in a $\mathrm{H_2O_2} : \mathrm{H_3PO_4} : \mathrm{H_2O}$ solution for $60\,\mathrm{s}$, followed by a stop in

deionized (DI) water. The solution etches the exposed area at an average speed of $100\,\mathrm{nm/min}$.

As the next step, we produce Ohmic contacts to the 2DEG. We define the contact area by optical-beam lithography. We then deposit $10\,\mathrm{nm}$ Ni, $200\,\mathrm{nm}$ AuGe, $10\,\mathrm{nm}$ Ni and $100\,\mathrm{nm}$ Au, by thermal evaporation. We then perform thermal annealing at $460\,^{\circ}\mathrm{C}$ for $90\,\mathrm{s}$ in a vacuum chamber with constant N_2 flow.

As the final fabrication step, we pattern the gate electrodes that are used for lateral confinement of the 2DEG; in particular, these electrodes are used to define QDs and QPCs. This step comprises e-beam lithography followed by thermal evaporation and liftoff. We use standard poly(methyl methacrylate) (PMMA) as the e-beam resist, spun and baked so as to obtain a thickness of 80 to $100\,\mathrm{nm}$. At $30\,\mathrm{kV}$ extraction voltage, a typical dose required for patterning a $100\,\mathrm{nm}$ wide feature is around $250\,\mu\mathrm{Ccm}^{-2}$. As for the deposited material, we achieve good result using either $30\,\mathrm{nm}$ Al or $5\,\mathrm{nm}$ Ti followed by $25\,\mathrm{nm}$ Au. A quick plasma ashing process ("descum") can be performed after development and prior to metal deposition to clean the surface from resist remnants and other organic contaminants.

After preparation, the samples are accommodated in a dual-in-line package and wedge-bonded to the contact pins using Al wire.

Superconducting and hybrid tunnel junctions

We realize tunnel junctions using the standard shadow evaporation (or "Dolan bridge") technique and in-situ oxidation of Al in between subsequent evaporation steps. The key steps are summarized in Fig. 6.1. We start our process from a commercial four-inch silicon wafer. We use P-type doped wafers with 5 to $10\,\Omega\mathrm{cm}$ sheet resistance. The wafers are single-side polished and $300\,\mathrm{nm}$ thermal oxide has been grown on the surface.

Most of the tunnel-junction devices measured in this thesis can be fabricated with a single lithographic step. In order for the shadow evaporation technique to succeed, it is important to achieve a good undercut; that is, the profile of the developed resist should look like in Fig. 6.1(c). For this reason, we employ a multi-layer spin-coating technique. We first spin-coat the highly sensitive copolymer poly(methylmetacrylate-methacrylic acid) [P(MMA-MAA)]. The spinning/baking process can also be repeated two or three times to achieve the desired thickness, which can vary from a few hundred nm to a couple $\mu\mathrm{m}$. As the last layer, we deposit a $100\,\mathrm{nm}$ thick layer of PMMA. In typical conditions and with extraction voltages up to

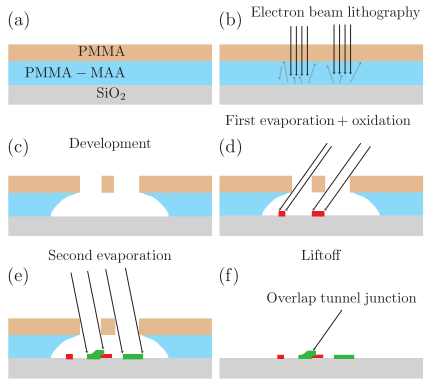

Figure 6.1. The shadow evaporation technique. After [192].

30 kV, the multi-layer technique alone guarantees a good result for deposition angles up to 10°. This cannot be taken as a general rule, however, as the results strongly depend on the geometry of the pattern. Furthermore, the exposure of the copolymer is strongly reduced at higher extraction voltages (100 kV), due to reduced electron backscattering. For high extraction voltages, we obtain good results by adding an exposure step for the area surrounding the small features to be patterned, using 10 to 20% of the standard dose. We also obtain acceptable results by using a selective remover for the copolymer (methyl-glycol diluted in methanol).

The evaporation and oxidation steps are performed in an e-beam evaporator where the following materials are in use: Ag, Al, Au, AuPd, Cu, and Ti. An Ar plasma gun is available in the evaporator chamber. We use it for in-situ ashing before depositing the material. This additional step improves reproducibility and significantly eases the liftoff. A typical pressure in the evaporator during material deposition is 1×10^{-7} mbar. We use oxidation pressures ranging from 0.2 up to 20 mbar, with an oxidation times of a few minutes. In general, higher oxidation pressures are required if the Ar plasma is used. Using 1 mbar oxidation pressure for 2 minutes, we obtain for our Al/AlOx/Cu junctions a resistance per unit area around 500 Ωμm^2. The liftoff is typically done by leaving the sample in lukewarm (30 °C) acetone for 1 h.

After preparation, the samples are wedge-bonded to a sample stage using Al wire.

6.2 Measurement set-up

All measurements performed in this thesis are low-temperature electronic measurements. The samples were cooled down in He-3 cryostats (Oxford), down to $250\,\mathrm{mK}$; in plastic dilution refrigerators that we build and maintain in-house, down to $50\,\mathrm{mK}$; and in commercial dilution refrigerators (Bluefors, Oxford), with $20\,\mathrm{mK}$ measured and $8\,\mathrm{mK}$ nominal base temperature. We will not discuss cryogenic techniques here; for a review, see [165]. Instead, we will briefly describe the electrical set-ups for each type of experiment.

Quantum dot thermometry

In quantum-dot thermometry experiments, the measurements are performed at low frequency. Battery-powered digital-to-analog converters (DACs) are used as clean voltage sources for the gates. Two-probe transport measurements are performed by applying a source-drain voltage between one probe and the common ground and reading out the current with a transconductance amplifier (or "current-to-voltage converter"). Differential conductance measurements are performed by phase-sensitive detection using a lock-in amplifier (Stanford Research SR830), using an excitation frequency of a few Hz and excitation amplitude in the linear response regime. In the set-up of Publication VIII, the measurement wiring consisted of constantan twisted pairs all the way down to the ^{3}He pot. The lines were filtered by π filters at room temperature and RC filters at the ^{3}He pot. In the final measurement in the dilution fridge, copper-powder filters were also used at the mixing chamber. A similar measurement set-up for transport experiments in quantum dots and quantum point contacts is described in more detail in several PhD theses from Delft University; see, for instance, [193].

Cooper-pair pumping

The measurements of Publication IV required three custom-shaped pulses to be sent to the sample at frequencies in the range of 10 to $100\,\mathrm{MHz}$. One "gate pulse" was sent to the island gate and two "flux pulses" to one end of the on-chip coils used to control the two SQUIDs (see Fig. 2.2). The other end of the on-chip coils was grounded at the sample stage. The pulses were generated using arbitrary waveform generators (AWGs) with 1Gs/s

(Tektronix AFG3252) and 12Gs/s sampling rate (Tektronix AWG7122). Bias tees were used so as to decouple the dc and the rf components of the pulses. In this way, it was possible to isolate the noisy generators by using in-and-out dc blocks while using battery-powered sources for providing the dc voltages. Transport measurements across the pump were performed in the standard, two-probe setting.

The wiring was done differently for the dc and rf lines. For the dc lines, we used manganin twisted pairs down to the 2 K stage, followed by at least 2m lossy coaxial line (Thermocoax) and $100\,\Omega$ surface-mount resistors. The lossy coaxial line provides a strong attenuation at frequencies above $1\,\mathrm{GHz}$. It also provides around $0.5\,\mathrm{nF}$ distributed capacitance and $200\,\Omega$ resistance, thereby realizing an RC filter with cutoff frequency of a few MHz. The rf lines were attenuated at different temperature stages and filtered with a commercial multi-stage LC filter at the mixing chamber. The voltages applied to the gate were of the order of a few mV and the currents flowing in the coils of the order of $200\,\mu\mathrm{A}$.

Fast thermometry

The measurements of Publication XI also required a combination of dc and rf signals to be sent to the sample. In addition, they required a fast readout line to probe the resonator. Our current set-up for fast thermometry measurements is depicted in Fig. 6.2. A resonant tone is sent via the input line and the transmittance is probed at the output line. The bias point of the NIS junction can be tuned by applying a dc voltage over the bias line. Finally, custom-shaped heating pulses can be sent through the heating line. The rf input/output signals are handled by suitable PCI extensions for instrumentation (PXI) modules from Aeroflex, including a local oscillator, a signal generator and a wideband rf digitizer. The dc voltage bias is applied by a battery-powered DAC. Finally, the heating pulse is generated by an AWG. All the rf instrumentation is isolated from the ground of the fridge by using in-and-out dc blocks (not shown).

As the four lines serve different purposes, different choices have been made for each of them. The dc line consists of a 2m long Thermocoax wire going directly from room temperature down to the mixing chamber. Heat sinking is achieved by clamping the wire at different temperature stages using copper clamps. At the mixing chamber, the wire is connected via a MCX-type connector to another $25\,\mathrm{cm}$ long Thermocoax wire, whose inner and outer conductor are directly soldered to the sample stage and to

the printed circuit board of the sample stage, respectively. The sample stage is an indium-sealed, rf-tight copper box. As for the rf lines, different types of coaxial cables are used at different temperature. The choice of the material is a tradeoff between low thermal conductance and low attenuation, which is particularly important for the output line. We have installed Be-Cu coaxial wires down to 2 K and superconducting Nb wires from 2 K down to the mixing chamber. When connecting parts of the circuit at the same temperature, we use standard Cu cables. Our noise-reduction strategy for the heating and input lines relies mostly on heavy attenuation and partly on a commercial high-rejection LC filter mounted at the mixing chamber. [1] By contrast, in the output line we use two circulators in series to isolate the output port of the resonator from the higher-temperature stages. Each circulator provides around $20\,\mathrm{dB}$ isolation. We have also installed a low-temperature amplifier (Quinstar) at the $2\,\mathrm{K}$ plate. It has a gain of at least $40\,\mathrm{dB}$ between 550 and $650\,\mathrm{MHz}$ and a nominal noise temperature of $6.5\,\mathrm{K}$.

[1] Copper-powder or Eccosorb filters would be a valuable addition to our set-up.

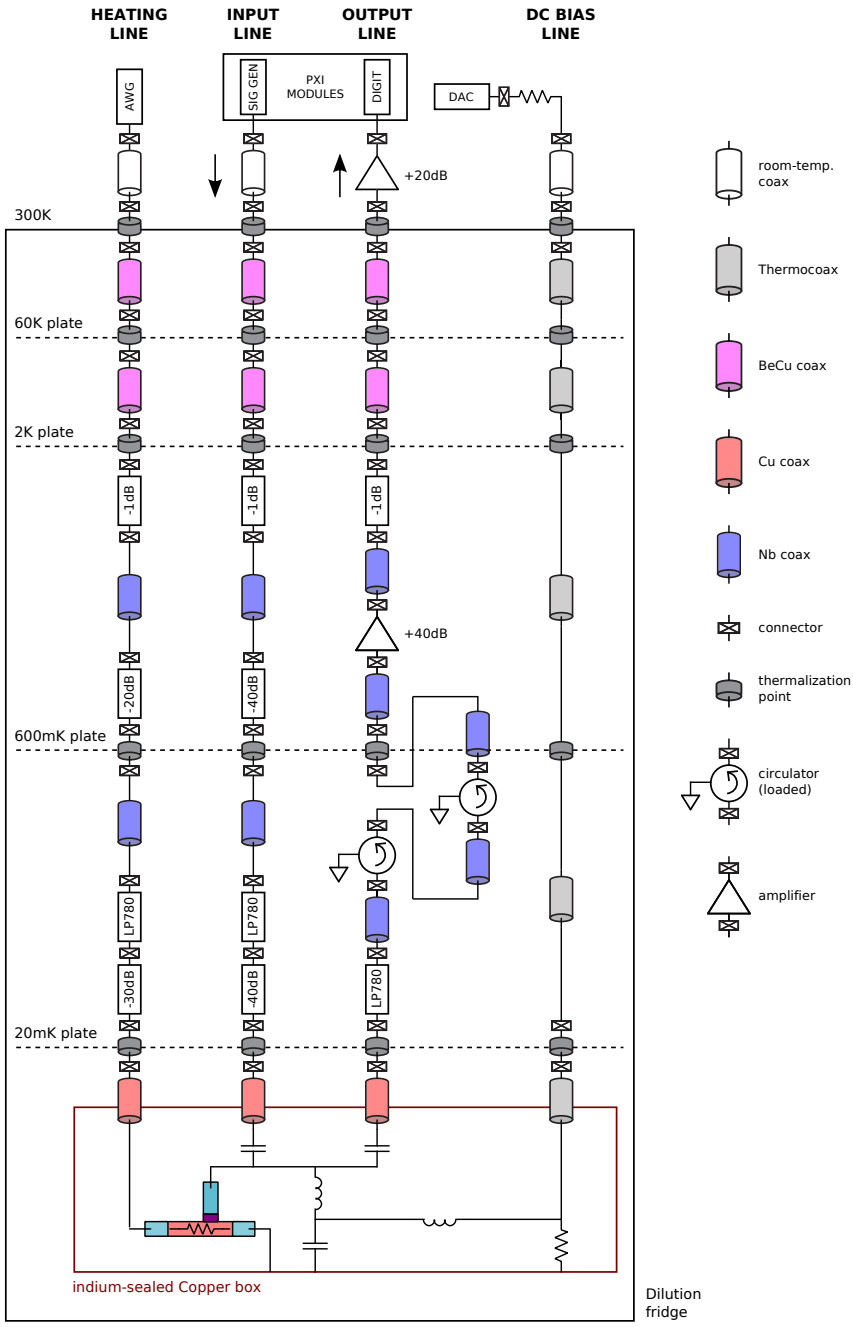

Figure 6.2. Experimental set-up for fast thermometry measurements. See the text for details.

Bibliography

[1] L. J. Geerligs et al., Zeitschrift für Phys. B **85**, 349 (1991).

[2] J. J. Toppari, J. M. Kivioja, J. P. Pekola, and M. T. Savolainen, J. Low Temp. Phys. **136**, 57 (2004).

[3] R. Leone, L. P. Lévy, and P. Lafarge, Phys. Rev. Lett. **100**, 117001 (2008).

[4] A. O. Niskanen, J. P. Pekola, and H. Seppä, Phys. Rev. Lett. **91**, 177003 (2003).

[5] A. O. Niskanen, J. M. Kivioja, H. Seppä, and J. P. Pekola, Phys. Rev. B **71**, 12513 (2005).

[6] M. Möttönen, J. P. Pekola, J. J. Vartiainen, V. Brosco, and F. W. J. Hekking, Phys. Rev. B **73**, 214523 (2006).

[7] M. Möttönen, J. J. Vartiainen, and J. P. Pekola, Phys. Rev. Lett. **100**, 177201 (2008).

[8] F. Hoehne et al., Phys. Rev. B **85**, 140504 (2012).

[9] J. P. Pekola et al., Rev. Mod. Phys. **85**, 1421 (2013).

[10] J. P. Pekola et al., Nat. Phys. **4**, 120 (2008).

[11] M. D. Blumenthal et al., Nat. Phys. **3**, 343 (2007).

[12] S. P. Giblin et al., Nat. Commun. **3**, 930 (2012).

[13] L. Fricke et al., Phys. Rev. Lett. **112**, 226803 (2014).

[14] A. Rossi et al., Nano Lett. **14**, 3405 (2014).

[15] J. P. Pekola, P. Solinas, a. Shnirman, and D. V. Averin, New J. Phys. **15**, 115006 (2013).

[16] Y. Makhlin, G. Schön, and A. Shnirman, Rev. Mod. Phys. **73**, 357 (2001).

[17] M. Aunola and J. J. Toppari, Phys. Rev. B **68**, 020502(R) (2003).

[18] P. J. Leek et al., Science **318**, 1889 (2007).

[19] S. N. Shevchenko, S. Ashhab, and F. Nori, Phys. Rep. **492**, 1 (2010).

[20] X. Tan et al., Phys. Rev. Lett. **112**, 027001 (2014).

[21] J. Zhang, J. Zhang, X. Zhang, and K. Kim, Phys. Rev. A **89**, 013608 (2014).

[22] M. H. Devoret and R. J. Schoelkopf, Science **339**, 1169 (2013).

[23] R. Kosloff and A. Levy, Annu. Rev. Phys. Chem. **65**, 365 (2014).

[24] J. P. Pekola, V. Brosco, M. Möttönen, P. Solinas, and A. Shnirman, Phys. Rev. Lett. **105**, 030401 (2010).

[25] P. Solinas, M. Möttönen, J. Salmilehto, and J. P. Pekola, Phys. Rev. B **82**, 134517 (2010).

[26] J. Salmilehto and M. Möttönen, Phys. Rev. B **84**, 174507 (2011).

[27] I. Kamleitner and A. Shnirman, Phys. Rev. B **84**, 235140 (2011).

[28] A. Russomanno, S. Pugnetti, V. Brosco, and R. Fazio, Phys. Rev. B **83**, 214508 (2011).

[29] Y. Nakamura, Y. A. Pashkin, and J. S. Tsai, Nature **398**, 786 (1999).

[30] O. Astafiev, Y. Pashkin, Y. Nakamura, T. Yamamoto, and J. Tsai, Phys. Rev. Lett. **93**, 267007 (2004).

[31] D. Vion et al., Science **296**, 886 (2002).

[32] G. Ithier et al., Phys. Rev. B **72**, 134519 (2005).

[33] J. Koch et al., Phys. Rev. A **76**, 042319 (2007).

[34] V. E. Manucharyan, J. Koch, L. I. Glazman, and M. H. Devoret, Science **326**, 113 (2009).

[35] R. Barends et al., Phys. Rev. Lett. **111**, 080502 (2013).

[36] P. W. Brouwer, Phys. Rev. B **58**, 10135 (1998).

[37] M. Switkes, Science **283**, 1905 (1999).

[38] P. W. Brouwer, Phys. Rev. B **63**, 121303 (2001).

[39] S. Russo, J. Tobiska, T. M. Klapwijk, and A. Morpurgo, Phys. Rev. Lett. **99**, 086601 (2007).

[40] F. Giazotto et al., Nat. Phys. **7**, 857 (2011).

[41] J. P. Pekola, J. J. Toppari, M. Aunola, M. T. Savolainen, and D. V. Averin, Phys. Rev. B **60**, R9931 (1999).

[42] M. Aunola, J. J. Toppari, and J. P. Pekola, Phys. Rev. B **62**, 1296 (2000).

[43] A. Messiah, *Quantum Mechanics*, North-Holland, Amsterdam, 1st edition, 1961.

[44] J. Samuel and R. Bhandari, Phys. Rev. Lett. **60**, 2339 (1988).

[45] G. García de Polavieja and E. Sjöqvist, Am. J. Phys. **66**, 431 (1998).

[46] J. Salmilehto and M. Möttönen, Phys. Rev. B **86**, 184512 (2012).

[47] I. M. Pop et al., Nat. Phys. **6**, 589 (2010).

[48] S. Gasparinetti et al., unpublished.

[49] J. M. Martinis and R. L. Kautz, Phys. Rev. Lett. **63**, 1507 (1989).

[50] R. L. Kautz and J. M. Martinis, Phys. Rev. B **42**, 9903 (1990).

[51] J. M. Kivioja et al., Phys. Rev. Lett. **94**, 247002 (2005).

[52] V. Krasnov et al., Phys. Rev. Lett. **95**, 157002 (2005).

[53] A. Kemppinen, *Tunnel junction devices for quantum metrology*, PhD thesis, Helsinki Unversity of Technology, 2009.

[54] Retrieved from `http://www.boat-ed.com/`. (c) Kalkomey 1998-2014. .

[55] J. M. Martinis, M. Ansmann, and J. Aumentado, Phys. Rev. Lett. **103**, 097002 (2009).

[56] G. Catelani et al., Phys. Rev. Lett. **106**, 077002 (2011).

[57] P. Joyez, P. Lafarge, A. Filipe, D. Esteve, and M. H. Devoret, Phys. Rev. Lett. **72**, 2458 (1994).

[58] J. Aumentado, M. W. Keller, J. M. Martinis, and M. H. Devoret, Phys. Rev. Lett. **92**, 066802 (2004).

[59] A. J. Ferguson, N. A. Court, F. E. Hudson, and R. G. Clark, Phys. Rev. Lett. **97**, 106603 (2006).

[60] R. Barends et al., Appl. Phys. Lett. **99**, 113507 (2011).

[61] O.-P. Saira, A. Kemppinen, V. F. Maisi, and J. P. Pekola, Phys. Rev. B **85**, 012504 (2012).

[62] T. A. Fulton, P. L. Gammel, D. J. Bishop, L. N. Dunkleberger, and G. J. Dolan, Phys. Rev. Lett. **63**, 1307 (1989).

[63] B. Damski and W. H. Zurek, Phys. Rev. A **73**, 063405 (2006).

[64] Y. Kayanuma, Phys. Rev. A **55**, R2495 (1997).

[65] M. Grifoni and P. Hänggi, Phys. Rep. **304**, 229 (1998).

[66] F. Grossmann, T. Dittrich, P. Jung, and P. Hänggi, Phys. Rev. Lett. **67**, 516 (1991).

[67] K. Eckert et al., Phys. Rev. A **70**, 023606 (2004).

[68] A. D. Greentree, J. H. Cole, A. R. Hamilton, and L. C. L. Hollenberg, Phys. Rev. B **70**, 235317 (2004).

[69] J. Siewert, T. Brandes, and G. Falci, Opt. Commun. **264**, 435 (2006).

[70] I. Kamleitner, J. Cresser, and J. Twamley, Phys. Rev. A **77**, 032331 (2008).

[71] J. Huneke, G. Platero, and S. Kohler, Phys. Rev. Lett. **110**, 036802 (2013).

[72] L. Pfeiffer and K. W. West, Physica E **20**, 57 (2003).

[73] W. Pan et al., Phys. Rev. Lett. **83**, 3530 (1999).

[74] K. v. Klitzing, G. Dorda, and M. Pepper, Phys. Rev. Lett. **45**, 494 (1980).

[75] D. C. Tsui, H. L. Stormer, and A. C. Gossard, Phys. Rev. Lett. **48**, 1559 (1982).

[76] P. Simon and D. Loss, Phys. Rev. Lett. **98**, 156401 (2007).

[77] C. Scheller et al., Phys. Rev. Lett. **112**, 066801 (2014).

[78] P. Nozieres and A. Blandin, J. Phys. Paris **41**, 193 (1980).

[79] A. Zawadowski, Phys. Rev. Lett. **45**, 211 (1980).

[80] R. M. Potok, I. G. Rau, H. Shtrikman, Y. Oreg, and D. Goldhaber-Gordon, Nature **446**, 167 (2007).

[81] R. Willett et al., Phys. Rev. Lett. **59**, 1776 (1987).

[82] C. Nayak, A. Stern, M. R. Freeman, and S. Das Sarma, Rev. Mod. Phys. **80**, 1083 (2008).

[83] A. C. Clark, K. K. Schwarzwälder, T. Bandi, D. Maradan, and D. M. Zumbühl, Rev. Sci. Instrum. **81**, 103904 (2010).

[84] L. Casparis et al., Rev. Sci. Instrum. **83**, 083903 (2012).

[85] D. Maradan et al., J. Low Temp. Phys. **175**, 784 (2014).

[86] F. Giazotto, T. T. Heikkilä, A. Luukanen, A. M. Savin, and J. P. Pekola, Rev. Mod. Phys. **78**, 217 (2006).

[87] J. T. Muhonen, M. Meschke, and J. P. Pekola, Rep. Prog. Phys. **75**, 046501 (2012).

[88] H. L. Edwards, Q. Niu, and A. L. de Lozanne, Appl. Phys. Lett. **63**, 1815 (1993).

[89] H. L. Edwards, Q. Niu, G. A. Georgakis, and A. L. de Lozanne, Phys. Rev. B **52**, 5714 (1995).

[90] J. R. Prance et al., Phys. Rev. Lett. **102**, 146602 (2009).

[91] C. W. J. Beenakker, Phys. Rev. B **44**, 1646 (1991).

[92] H. van Houten, C. W. J. Beenakker, and A. A. M. Staring, Coulomb-Blockade Oscillations in Semiconductor Nanostructures, in *NATO ASI Ser. B294*, edited by H. Grabert and M. H. Devoret, Plenum Press, New York, 1992.

[93] L. P. Kouwenhoven et al., Electron transport in quantum dots, in *Mesoscopic Electron Transport*, edited by L. L. Sohn, L. P. Kouwenhoven, and G. Schön, pages 16–23, Kluwer, 1997.

[94] I. Karakurt, V. Goldman, J. Liu, and A. Zaslavsky, Phys. Rev. Lett. **87**, 146801 (2001).

[95] I. P. Radu et al., Science **320**, 899 (2008).

[96] J. R. Prance, *Cooling an electron gas using quantum dot based electronic refrigeration*, PhD thesis, University of Cambridge, 2009.

[97] A. Mavalankar et al., Appl. Phys. Lett. **103**, 133116 (2013).

[98] V. S. Khrapai, S. Ludwig, J. P. Kotthaus, H. P. Tranitz, and W. Wegscheider, Phys. Rev. Lett. **99**, 96803 (2007).

[99] D. Harbusch, D. Taubert, H. P. Tranitz, W. Wegscheider, and S. Ludwig, Phys. Rev. Lett. **104**, 196801 (2010).

[100] N. J. Appleyard, J. T. Nicholls, M. Y. Simmons, W. R. Tribe, and M. Pepper, Phys. Rev. Lett. **81**, 3491 (1998).

[101] F. Deon et al., Appl. Phys. Lett. **96**, 142107 (2010).

[102] S. De Franceschi et al., Appl. Phys. Lett. **83**, 344 (2003).

[103] E. A. Hoffmann et al., Nano Lett. **9**, 779 (2009).

[104] Y. Zhang et al., Phys. Rev. B **79**, 241304 (2009).

[105] L. W. Molenkamp, H. Van Houten, C. W. J. Beenakker, R. Eppenga, and C. T. Foxon, Phys. Rev. Lett. **65**, 1052 (1990).

[106] L. W. Molenkamp et al., Phys. Rev. Lett. **68**, 3765 (1992).

[107] A. A. M. Staring et al., Europhys. Lett. **22**, 57 (1993).

[108] U. Sivan and Y. Imry, Phys. Rev. B **33**, 551 (1986).

[109] H. Van Houten, L. W. Molenkamp, C. W. J. Beenakker, and C. T. Foxon, Semicond. Sci. Technol. **7**, B215 (1992).

[110] P. J. Price, J. Appl. Phys. **53**, 6863 (1982).

[111] M. Field et al., Phys. Rev. Lett. **70**, 1311 (1993).

[112] J. M. Elzerman et al., Nature **430**, 431 (2004).

[113] L. DiCarlo et al., Phys. Rev. Lett. **92**, 226801 (2004).

[114] Y. Blanter and M. Büttiker, Phys. Rep. **336**, 1 (2000).

[115] E. Onac et al., Phys. Rev. Lett. **96**, 176601 (2006).

[116] S. Gustavsson et al., Phys. Rev. Lett. **99**, 206804 (2007).

[117] S. Gustavsson et al., Phys. Rev. B **78**, 035324 (2008).

[118] M. Pedersen, S. A. Van Langen, and M. Büttiker, Phys. Rev. B **57**, 1838 (1998).

[119] C. E. Young and A. A. Clerk, Phys. Rev. Lett. **104**, 186803 (2010).

[120] V. S. Khrapai, S. Ludwig, J. P. Kotthaus, H. P. Tranitz, and W. Wegscheider, Phys. Rev. Lett. **97**, 176803 (2006).

[121] G. Granger et al., Nat. Phys. **8**, 522 (2012).

[122] U. Seifert, Rep. Prog. Phys. **75**, 126001 (2012).

[123] C. Jarzynski, Phys. Rev. Lett. **78**, 2690 (1997).

[124] G. E. Crooks, Phys. Rev. E **60**, 2721 (1999).

[125] O.-P. Saira et al., Phys. Rev. Lett. **109**, 180601 (2012).

[126] J. Koski, T. Sagawa, O.-P. Saira, and Y. Yoon, Nat. Phys. **9**, 644 (2013).

[127] J. V. Koski, V. F. Maisi, T. Sagawa, and J. P. Pekola, Phys. Rev. Lett. **113**, 030601 (2014).

[128] M. Esposito, U. Harbola, and S. Mukamel, Rev. Mod. Phys. **81**, 1665 (2009).

[129] M. Campisi, P. Hänggi, and P. Talkner, Rev. Mod. Phys. **83**, 771 (2011).

[130] P. Solinas, D. V. Averin, and J. P. Pekola, Phys. Rev. B **87**, 060508 (2013).

[131] P. Talkner, E. Lutz, and P. Hänggi, Phys. Rev. E **75**, 050102 (2007).

[132] R. Dorner et al., Phys. Rev. Lett. **110**, 230601 (2013).

[133] L. Mazzola, G. De Chiara, and M. Paternostro, Phys. Rev. Lett. **110**, 230602 (2013).

[134] F. W. J. Hekking and J. P. Pekola, Phys. Rev. Lett. **111**, 093602 (2013).

[135] M. Silaev, T. T. Heikkilä, and P. Virtanen, arXiv:1312.3476v2.

[136] M. Meschke, W. Guichard, and J. P. Pekola, Nature **444**, 187 (2006).

[137] A. V. Timofeev, M. Helle, M. Meschke, M. Möttönen, and J. P. Pekola, Phys. Rev. Lett. **102**, 200801 (2009).

[138] J. M. Rowell and D. C. Tsui, Phys. Rev. B **14**, 2456 (1976).

[139] M. Nahum and J. M. Martinis, Appl. Phys. Lett. **63**, 3075 (1993).

[140] M. Nahum, T. M. Eiles, and J. M. Martinis, Appl. Phys. Lett. **65**, 3123 (1994).

[141] J. Bardeen, L. N. Cooper, and J. R. Schrieffer, Phys. Rev. **108**, 1175 (1957).

[142] R. C. Dynes, V. Narayanamurti, and J. P. Garno, Phys. Rev. Lett. **41**, 1509 (1978).

[143] J. P. Pekola et al., Phys. Rev. Lett. **105**, 026803 (2010).

[144] H. Pothier, S. Guéron, N. O. Birge, and D. Esteve, Zeitschrift für Phys. B **103**, 313 (1997).

[145] D. V. Averin and K. K. Likharev, Single-electronics, in *Mesoscopic Phenomena in Solids*, edited by B. Altshuler, P. A. Lee, and R. Webb, page 173, North-Holland, Amsterdam, 1991.

[146] G. L. Ingold and Y. V. Nazarov, Charge tunneling rates in ultrasmall junctions, in *Single Charge Tunneling*, edited by H. Grabert and M. H. Devoret, volume 294, chapter 2, pages 21–107, Plenum Press, New York, 1992.

[147] V. F. Maisi, *Andreev tunneling and quasiparticle excitations in mesoscopic normal metal – superconductor structures*, PhD thesis, Aalto University, 2014.

[148] D. R. Schmidt, C. S. Yung, and A. N. Cleland, Appl. Phys. Lett. **83**, 1002 (2003).

[149] R. J. Schoelkopf, P. Wahlgren, A. A. Kozhevnikov, and D. E. Prober, Science **280**, 1238 (1998).

[150] H. Qin and D. A. Williams, Appl. Phys. Lett. **88**, 203506 (2006).

[151] D. J. Reilly, C. M. Marcus, M. P. Hanson, and A. C. Gossard, Appl. Phys. Lett. **91**, 162101 (2007).

[152] M. Goppl et al., J. Appl. Phys. **104**, 113904 (2008).

[153] K. L. Viisanen, *Measuring temperature relaxation on a small proximized normal metal island with an RF-NIS thermometer*, Master thesis, Aalto University, 2014.

[154] D. Pozar, *Microwave Engineering*, Wiley, 2nd edition, 1998.

[155] J. P. Pekola et al., Phys. Rev. Lett. **92**, 056804 (2004).

[156] F. C. Wellstood, C. Urbina, and J. Clarke, Phys. Rev. B **49**, 5942 (1994).

[157] M. L. Roukes, M. R. Freeman, R. S. Germain, R. C. Richardson, and M. B. Ketchen, Phys. Rev. Lett. **55**, 422 (1985).

[158] L. J. Taskinen, J. M. Kivioja, J. T. Karvonen, and I. J. Maasilta, phys. stat. sol. (c) **1**, 2856 (2004).

[159] J. Karvonen, L. Taskinen, and I. Maasilta, Phys. Rev. B **72**, 012302 (2005).

[160] H. Q. Nguyen et al., New J. Phys. **15**, 085013 (2013).

[161] H. Q. Nguyen, M. Meschke, J. P. Pekola, and H. Courtois, arXiv:1402.5872v1.

[162] J. T. Peltonen et al., Phys. Rev. Lett. **105**, 097004 (2010).

[163] D. R. Schmidt, C. S. Yung, and A. N. Cleland, Phys. Rev. B **69**, 140301 (2004).

[164] D. R. Schmidt et al., Appl. Phys. Lett. **86**, 053505 (2005).

[165] F. Pobell, *Matter and methods at low temperatures*, Springer, 3rd edition, 2007.

[166] A. Anthore, F. Pierre, H. Pothier, and D. Esteve, Phys. Rev. Lett. **90**, 076806 (2003).

[167] L. M. A. Pascal, A. Fay, C. B. Winkelmann, and H. Courtois, Phys. Rev. B **88**, 100502 (2013).

[168] M. A. Castellanos-Beltran and K. W. Lehnert, Appl. Phys. Lett. **91**, 083509 (2007).

[169] H.-P. Breuer and F. Petruccione, *The Theory of Open Quantum Systems*, Oxford University Press, 2007.

[170] A. Caldeira and A. Leggett, Phys. Rev. Lett. **46**, 211 (1981).

[171] R. Blümel et al., Phys. Rev. A **44**, 4521 (1991).

[172] T. Dittrich, B. Oelschlägel, and P. Hänggi, Europhys. Lett. **22**, 5 (1993).

[173] B. Oelschlägel, T. Dittrich, and P. Hänggi, Acta Phys. Pol. B **24**, 845 (1993).

[174] S. Gasparinetti and P. Solinas, unpublished.

[175] W. Lamb and R. Retherford, Phys. Rev. **72**, 241 (1947).

[176] H. Bethe, Phys. Rev. **72**, 339 (1947).

[177] A. Fragner et al., Science **322**, 1357 (2008).

[178] C. M. Wilson et al., Phys. Rev. Lett. **98**, 257003 (2007).

[179] C. M. Wilson et al., Phys. Rev. B **81**, 024520 (2010).

[180] J. Tuorila et al., Phys. Rev. Lett. **105**, 257003 (2010).

[181] J. Tuorila et al., Supercond. Sci. Technol. **26**, 124001 (2013).

[182] M. Silveri, J. Tuorila, M. Kemppainen, and E. Thuneberg, Phys. Rev. B **87**, 134505 (2013).

[183] K. Szczygielski, D. Gelbwaser-Klimovsky, and R. Alicki, Phys. Rev. E **87**, 012120 (2013).

[184] M. Langemeyer and M. Holthaus, Phys. Rev. E **89**, 012101 (2014).

[185] B. Mollow, Phys. Rev. **188**, 1969 (1969).

[186] C. Cohen-Tannoudji, J. Dupont-Roc, and G. Grynberg, *Atom-Photon Interactions: Basic Processes and Applications*, Wiley, New York, 1998.

[187] S. Haroche and J. M. Raimond, *Exploring the Quantum: Atoms, Cavities, and Photons*, Oxford University Press, 2006.

[188] A. Braggio, J. König, and R. Fazio, Phys. Rev. Lett. **96**, 026805 (2006).

[189] J. Piilo, S. Maniscalco, K. Härkönen, and K.-A. Suominen, Phys. Rev. Lett. **100**, 180402 (2008).

[190] A. Wallraff et al., Nature **431**, 162 (2004).

[191] F. Persson, C. M. Wilson, M. Sandberg, and P. Delsing, Phys. Rev. B **82**, 134533 (2010).

[192] J. T. Peltonen, *Fluctuations, relaxation and proximity effect in superconducting circuits*, PhD thesis, Aalto University, 2011.

[193] R. Hanson, *Electron spins in semiconductor quantum dots*, PhD thesis, Delft Unversity of Technology, 2005.

Aalto-DD 165/2014

ISBN 978-952-60-5919-8 (printed)
ISBN 978-952-60-5920-4 (pdf)
ISSN-L 1799-4934
ISSN 1799-4934 (printed)
ISSN 1799-4942 (pdf)

Aalto University
School of Science
O.V. Lounasmaa Laboratory
www.aalto.fi

BUSINESS +
ECONOMY

ART +
DESIGN +
ARCHITECTURE

SCIENCE +
TECHNOLOGY

CROSSOVER

DOCTORAL
DISSERTATIONS